UNIVERSITY OF TROMSØ UIT

Faculty of Science and Technology
Department of Geology

Strength and rheological evolution of the lower continental crust: an experimental study of the deformation behaviour of feldspar and quartz at high pressure and temperature

Marianne Negrini

A dissertation for the degree of
Philosophiae Doctor

May 2013

Strength and rheological evolution of the lower continental crust: an experimental study of the deformation behavior of feldspar and quartz at high pressure and temperature

Marianne Negrini

May 2013

Acknowledgements

I am grateful to many people for help and support during my PhD.

First I want to thank my supervisor Prof. Holger Stünitz for making this thesis possible and for his patient help.

Many thanks also to the entire "Hard Rock Geology Group" (Erling Ravna, Steffen Bergh, Kare Kullerud, Luca Menegon, Pritam Nasipuri). Without their help, suggestions, advices, discussions and good cheer everything would have been immensely more difficult.

I am grateful to Matej Pec and Anja Thust for introducing me in the Lab work and helping me in many occasions.

Many thanks to Alfons Berger, Luiz Morales, Marco Herweg, Eric Reusser for letting me use the microscopes (EMPA, SEM, EBSD), helping me in the analytical procedures, discuss the data and supporting me.

I want to express my gratitude to the technical stuff of the geological department (Steiner, Frode, Trine) for the technical support and to the administrative team (Annbjørg, Stig Arne, Kai) for kindly helping with practical and administrative difficulties.

Thanks to my friends in Norway that made my stay in Tromsø a wonderful experience. Special thanks to Nicole, Julia, Noortje, Philipp, Polina, Kasha, Andreia, Diane and the "lazy climbing team" (Eythor and Kjetill). It was great to share our PhD's together, and being distracted from them during skiing, kayaking, hiking, climbing, dining and nice trips in northern Norway. Thanks also to my friends in Switzerland, Italy, Austria and from wherever, which support and encouragement has been indispensable.

My parents and my sisters could never be properly thanked for all they have done for me while studying…GRAZIE!

Last but not least, I would like to thanks Steve for all his help, support and patience.

Abstract

Models representing the strength of the lithosphere (i.e. strength-depth profiles) are mainly based on the rheological properties of the minerals quartz and feldspar that, to a large extent, are determined in laboratory-based rock deformation studies. The study of the deformation behavior of quartz and feldspar is of fundamental importance for the understanding and modeling of plate tectonics and orogenic processes in general. However, the rheology of the crust is intensely debated because field observations sometimes do not support models based on geophysical data. Experiments may resolve some of the discrepancies.

The aim of this study is to reproduce in the laboratory, by means of high pressure and high temperature deformation experiments, the microstructures and reactions observed in quartz and feldspar in nature in order to quantify and explore deformation processes in the lower continental crust. The deformation experiments were performed on natural single crystals and powders of quartz and feldspar with a Griggs-type solid medium deformation apparatus. High confining pressures (Pc= 0.75-1.5 GPa) and temperatures (700 °C-1000 °C) were chosen in order to simulate lower crustal conditions. As in many laboratory deformation experiments, the use of very high temperatures was necessary to promote deformation of quartz and feldspar at the strain rates that can be achieved using the Griggs apparatus (10^{-6} to 10^{-7} in this work). Two main crustal processes were studied: (1) The effect of deformation on the TitaniQ (titanium in quartz) geothermobarometer and; (2) the deformation behavior and rheology of melt bearing feldspar single crystals and gouges.

(1) The geothermobarometer TitaniQ is based on Si-Ti substitution in quartz, which is both pressure and temperature dependent. Because the microstructural evolution of quartz under varying pressure and temperature conditions is relatively well characterized, the correlation between quartz microstructures and Ti content represents a promising method to directly estimate the pressure and temperature conditions of deformation. However, the effect that different mechanisms of recrystallization have on Ti incorporation is not fully understood, and thus it is unknown whether the TitaniQ geothermobarometer can be applied to deformed rocks of the lower crust. Our high pressure and temperature deformation experiment on quartz single crystals (Chapter 3) demonstrate that in a fluid-present and Ti-saturated environment, the Si—Ti substitution in quartz is not likely to occur during deformation, regardless of the recrystallization mechanism involved in the deformation process. In our experiments, neither quartz grains that deformed by subgrain rotation recrystallization

nor those showing grain boundary migration features incorporate equilibrium contents of Ti. These results suggest that the application of the TitaniQ geothermobarometer to deformed rocks under prograde metamorphic conditions is not as straightforward as previously thought.

(2) Previous experimental studies suggest that fluid-bearing feldspar deforms by viscous processes at temperatures > 700 °C. However, field observations indicate that under lower crustal conditions feldspar can deform by brittle processes, even at high temperature. Microstructural observations and mechanical data from high-temperature and high-pressure deformation experiments on K-feldspar single crystals (Chapter 4) demonstrate that deformation is initially accommodated by brittle fractures, which cause grain size reduction and formation of gouges. Dilatation along the fractures leads to a local decrease of the confining pressure and promotes melting in cracked regions. However, the presence of melt in the system does not significantly influence the strength of the rock as melt is present only in small fractions and, during deformation, it remains isolated without forming an interconnected network. Preliminary microstructural observations of the fine grained fault gouges formed along brittle fractures suggests the activity of dissolution precipitation creep as the dominant deformation mechanism.

In order to better quantify and study the processes occurring in the gouges, shear experiments were performed on layers of fine grained aggregates of feldspar (Chapter 5). Microstructural observations supported by mechanical data indicate that the composition of the starting material has only a minor influence on the deformation behavior of water bearing feldspar gouges. Furthermore, no systematic differences were observed in melt bearing and melt free aggregates. The presence of regions of gouge showing pervasive compositional changes, the nucleation and growth of new euhedral grains with a different chemical composition, grains with lobate and indented grain boundaries, and overgrowth structures all suggest that in wet feldspar gouges at high pressure and temperature deformation is mainly accommodated by dissolution precipitation processes.

Table of contents

CHAPTER 5

List of figures

List of tables

CHAPTER 1

Introduction

1.1 General aspects of the lower continental crust

The lower continental crust is considered to be the portion of the crust that extends from approximately 10 km depth down to the Moho (Taylor and McLennan 1985). However, the depth extent and thickness of the lower crust vary considerably in different tectonic settings: in active rifts and in fore-arcs the lower crust is generally thinner (from 8-27 km) whereas in Mesozoic– Cenozoic orogenic belts it is generally thicker and can reach a depth of ~50 km (Rudnick and Fountain 1995).

Due to its inaccessible location and the relatively restricted number of outcrop exposures, direct observations of lower crustal material are limited. Information regarding the composition, structure, chemical and physical state of the lower crust is largely based on geophysical investigations (e.g., seismic and heat flow studies; Brown et al. 2003; Christensen and Mooney 1995; Holbrook et al. 1992; Kennett and van der Hilst 1998; Rudnick and Fountain 1995; Smithson 1978), mineralogical and geochemical data obtained from exposed crustal cross-sections and xenoliths (Bohlen and Mezger 1989; Condie 1999; Fountain et al. 1990; Hart et al. 1990; Kay and Kay 1981; Kern et al. 1999; Ketcham 1996; Miller and Christensen 1994; O'Reilly and Griffin 1996; Rudnick 1992; Schmitz and Bowring 2003; Vissers et al. 1997; Yu et al. 2003; Zhai et al. 2001; Zhang et al. 1998) and from interpretation of laboratory experiments performed on lithologies representative of the lower crust (Bürgmann and Dresen 2008; Kohlstedt et al. 1995; Rybacki and Dresen 2000).

The continental lower crust has a complex composition and structure (e.g., Kay and Kay 1981; Taylor and McLennan 1985). The chemical composition of the constituent rocks varies from felsic (granite; e.g., Brown et al. 2003; Christensen and Mooney 1995; Gao et al. 1998; Stöckhert and Renner 1998) to mafic (gabbro; Christensen and Mooney 1995; Weaver and Tarney 1984; Weaver and Tarney 1981; Weaver and Tarney 1980), with a general trend of increasing mafic components with depth leading to the development of a vertical stratification (Allmendinger et al. 1987; Fountain and Salisbury 1981; Matthews and Cheadle 1986). In addition to the vertical

stratification, large spatial heterogeneities in lower crustal composition are common, reflecting the often complicated geological evolution in a wide variety of tectonic settings (e.g., Dawson et al. 1986; Heacock 1971; Lambert and Heier 1968; Shankland and Ander 1983). Due to its complex nature and marked compositional and structural heterogeneity, the deformation behavior of the lower crust is only partly understood, and represents a topic of intensive ongoing research.

1.2 The strength of the lower crust

Knowledge of the strength and rheological properties of the continental lower crust is essential for modeling major geodynamic processes and for an understanding of the role that the lower crust plays in continental tectonics. One of the ways to estimate the strength of the lower crust is to extrapolate mechanical data obtained in laboratory rock deformation experiments to natural deformation conditions (e.g., Bürgmann and Dresen 2008; Kohlstedt et al. 1995; Rybacki and Dresen 2000).

Deformation experiments on feldspar at high pressure (1.0 -1.5 GPa) and high temperature (600 °C – 900 °C) have shown that one of the dominant deformation processes is recrystallization-accommodated dislocation creep (Borg and Hear 1970; Hadizadeh and Tullis 1992; Kronenberg and Shelton 1980; Marshall and Mclaren 1977; Tullis and Yund 1987, 1985, 1980, 1977). The activity of grain boundary migration, dislocation creep and dislocation glide in different types of feldspar (albite, anorthite, labradorite) has been reported in deformation experiments by several authors (e.g., Rybacki and Dresen 2000, Stünitz and Tullis 2001). Laboratory-derived dislocation creep flow laws for plagioclase deformed under water-present conditions predict a weak lower crust with a flow strength of less than 30 MPa at temperatures above 700 °C (Bürgmann and Dresen 2008; Gleason et al. 1993; Hirth et al. 2001; Luan and Paterson 1990; Paterson and Luan 1990 and references therein). Consequently, a rheological model of a weak and ductile granitic to dioritic lower crust overlying a mechanically stronger olivine-rich upper mantle is commonly utilized (e.g., Handy and Brun 2004). This rheological model, termed the “jelly sandwich” model (e.g., Burov and Diament 1995; Chen and Molnar 1983; Cloetingh and Burov 1996; Hirth and Kohlstedt 2003; Ranalli 1995; Ranalli and Murphy 1987; Watts and Burov 2003) (Fig. 1.1a), is in good agreement with microstructural studies of exhumed fault rocks in active and ancient plate margins (Handy and Brun 2004).

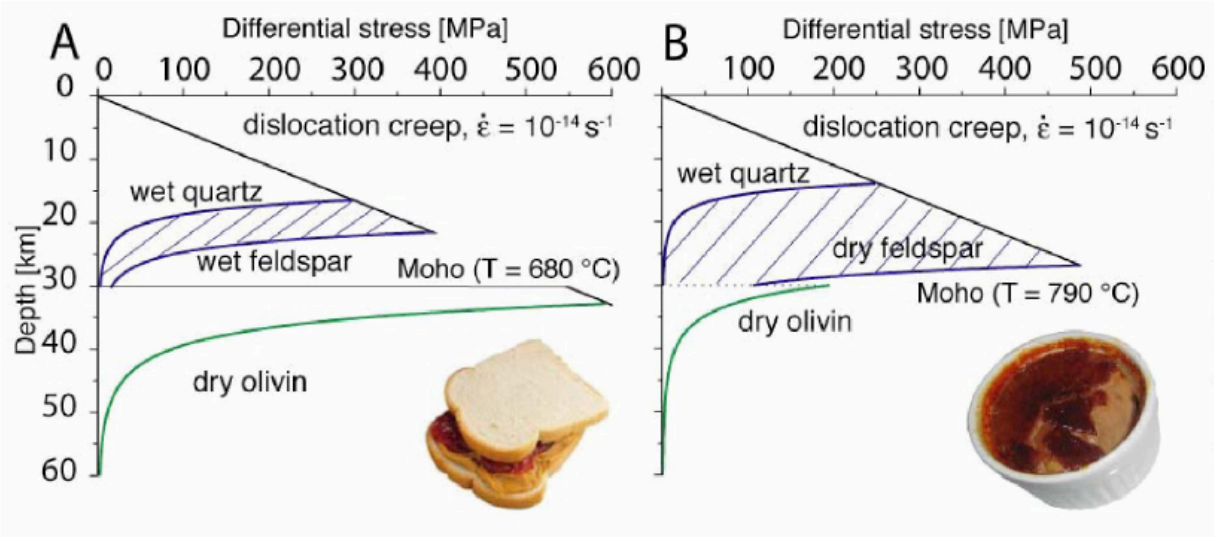

Fig. 1.1 Schematic representations of two models for the strength of the lithosphere**. (a)** The "jelly sandwich" model. **(b)** The "crème brûlée" model (from Burgman and Dresen 2008).

However, more recent interpretations of seismic data, geodynamic modeling, as well as the observation of brittle fractures and frictional melts (pseudotachylytes) in exhumed lower crustal exposures, indicates that the lower crust may support higher stresses than those predicted from the experimental data (Afonso and Ranalli 2004; Jackson 2002; Jackson et al. 2004; Kohlstedt et al. 1995; Lund et al. 2004; Mackwell et al. 1998; Maggi et al. 2000; Priestley et al. 2008; Rybacki and Dresen 2004; Rybacki and Dresen 2000). These observations suggest that the lower crust may be strong and brittle, and overly a weaker upper mantle. The "crème brûlée" rheological model has been developed for this scenario (Fig. 1.1b; Burov and Watts 2006; Jackson 2002; Maggi et al. 2000).

Although intensive experimental and field-based work has been performed on lower crustal materials, one of the outstanding questions is how brittle (e.g., fracturing) and viscous (e.g., dislocation and/or diffusion creep) deformation mechanisms interact in the lower crust, and what consequences this has for crustal rheology (e.g., Handy and Brun 2004; Jackson 2002; Jackson et al. 2004).

1.3 Strength variations

One reason for the complex deformation behavior of the feldspars - which constitutes one of the major mineralogical constituents of the lower crust - is the presence or absence of fluid in the system. For example, Rybacki and Dresen (2004) observed that dry plagioclase aggregates creep at strain rates lower than 10^{-14} sec^{-1} at a flow stress of 100 MPa and 700 °C, whereas wet plagioclase aggregates creep at strain rates up to 2 orders of magnitude faster even at lower temperatures (600 °C).

Recent measurements of the H_2O-contents of lower crustal plagioclase (Xia et al. 2006) indicate that natural water contents can be about 5-10 times lower than those used in the experiments of Rybacki and Dresen (2000). This raises the possibility that the lower crust may be stronger and "less ductile" than suggested by deformation experiments performed on "wet" plagioclase. Dry plagioclase rich rocks may deform in a semi-brittle way, whereby local fracturing occurs as a consequence of stress concentrations. Fracturing in turn may have a pronounced effect on rock permeability, facilitating fluid infiltration (Austrheim 1987; Brodie and Rutter 1985; Mancktelow and Pennacchioni 2004) and leading to a local "wet" rheology associated with the onset of viscous deformation.

Strength variations in the lower crust may also be caused by the presence of melt in the system. The P-T conditions of the lower crust are often high enough for partial melting to occur, which can influence considerably the rheology of the rock. Partial melting of the lower crust has been widely invoked to play an important role in the formation of orogens and mountain belts (e.g., Beaumont et al. 2001; Clark and Royden 2000; Davidson et al. 1994; King et al. 2010a; Royden et al. 2008).

Dramatic rock weakening caused by the presence of melt has been observed in deformation experiments (Arzi 1978; Mecklenburgh and Rutter 2003; Rutter and Neumann 1995; Scott and Kohlstedt 2006), and also inferred from field relationships (e.g., Beaumont et al. 2001; Davidson et al. 1994; Lexa et al. 2011; Schulmann et al. 2008; Slagstad 2005). Melt-induced weakening is controlled by a number of factors including (1) the amount, distribution, and interconnectivity of melt in the system, all of which are influenced by the deformation process itself (e.g., Arzi 1978; Molen and Paterson 1979; Rosenberg and Handy 2005; Wickham 1987; Cooper et al. 1989; Hirth and Kohlstedt 1995a; Hirth and Kohlstedt 1995b; Jin et al. 1994; Kohlstedt 1992; Pharr and Ashby 1983; Rosenberg and Handy 2005) (2) melt induced switches in deformation mechanisms, generally from dislocation creep to diffusion creep (Dell'Angelo et al. 1987; Dell'Angelo and Tullis 1988,

Schmid et al. 1977, Karato et al. 1986) and granular flow (= grain boundary sliding, Rosenberg and Handy 2001, Paterson 1999). Rocks undergoing partial melting often deform by several deformation mechanisms that operate simultaneously, meaning that representing such rocks with single rheological flow laws is very difficult (Handy et al. 2001; Rosenberg and Berger 2001).

1.4 Reconstruction of the pressure and temperature (P-T) conditions during deformation

In order to determinate the physical conditions (water content, partial melt, strength), deformation history (deformation mechanism, recrystallization) and rheological behavior of the lower crust, knowledge concerning the metamorphic path (i.e., pressure-temperature-time, P-T-t, path) experienced by a particular rock or rock suite is of fundamental importance. The pressure and temperature evolution of rocks can be determined by thermodynamic modeling based on the properties of minerals (P-T-X pseudosections) and/or by the chemistry of coexisting mineral phases (conventional thermobarometry). However, these methods have limitations when trying to correlate the metamorphic path of a rock with its deformation history. The geothermobarometer titanium-in-quartz (TitaniQ) introduced by Thomas et al. (2010) and Wark and Watson (2006) may allow a direct correlation of P-T conditions with the deformation history (Kohn and Northrup 2009), as it requires the analysis (both chemical and microstructural) of only a single phase, namely quartz. Because quartz is (1) ubiquitous in rocks of the continental crust, (2) stable under a wide range of metamorphic conditions, and (3) extensively studied in terms of its deformation behavior and microstructural characteristics, the TitaniQ geothermobarometer provides a promising tool for accurate estimations of the metamorphic-deformation path of lower crustal material. However, in certain field-based studies involving the TitaniQ geothermobarometer, discrepancies have been reported between the temperature and pressure conditions calculated with TitaniQ and those calculated with other more “conventional” geothermobarometers (e.g., Grujic et al. 2011; Wilson et al. 2012). An outstanding question is whether these discrepancies arise because of our poor understanding of how deformation and recrystallization affect incorporation of Ti into the quartz crystal lattice.

1.5 Aims and key issues of the thesis

The aim of this thesis is to use tightly-controlled high pressure and high temperature deformation experiments to provide a better understanding of the deformation mechanisms and deformation history of the lower continental crust. As described above, several questions remain regarding the interaction of brittle and viscous deformation mechanisms in the lower crust, and the reconstruction of P-T-deformation paths using the novel TitaniQ geothermobarometer. In this thesis we address to the following issues:

- The effect of deformation and recrystallization of quartz on the TitaniQ geothermobarometer
- The high pressure and high temperature deformation behavior of dry and water-bearing K-feldspar single crystals
- The relationships between brittle cracking, dilation and melt formation in K-feldspar single crystals
- The interactions between partial melting, melt distribution and deformation behavior in K-feldspar single crystals and gouges

1.6 Thesis outline and style

Chapters 3-5 of this thesis have been written as independent manuscripts that will be submitted separately to international earth science journals. As such, each chapter contains a separate abstract and introduction as well as separate sections dealing with the experimental and analytical methodologies, observations, discussion of the data and conclusions. Inevitably there is some overlap and repetition between the chapters, particularly in the sections dealing with the experimental methods. The content of each chapter is briefly described individually below:

Chapter 2:
Experimental techniques

This chapter introduces the laboratory techniques for the preparation and execution of the experiments used for this thesis. The Griggs-type solid medium deformation apparatus is briefly described. Furthermore an overview of the samples and the sample-assembly is given. The experimental procedures as well as the data acquisition and evaluation methods are described.

Chapter 3:

The effect of deformation on the TitaniQ geothermobarometer: an experimental study

This chapter is currently under review in the Journal "Contributions to Mineralogy and Petrology".

This chapter explores the relationship between deformation and the P-T dependent Ti-Si (Titanium-Silicon) substitution in quartz single crystals. Different types of deformation mechanisms (e.g., subgrain rotation recrystallization, grain boundary migration recrystallization) were activated during the experiments by changing the experimental conditions, crystal orientation and water content in order to study the effect that the different mechanisms may have on the incorporation and/or equilibration of Ti in the quartz crystal lattice. Detailed correlation between the experimental microstructures and Ti contents of the recrystallized grains (using scanning electron microscope observations and electron microprobe chemical analyses) highlighted some potential problems concerning the applicability of the TitaniQ geothermobarometer to deformed metamorphic rocks.

Chapter 4:

Partial melting and compositional changes in perthitic K-feldspar during experimental deformation at high pressure and temperature

This chapter presents the results of high pressure and high temperature deformation experiments performed on perthitic K-feldspar single crystals. The observed microstructures are discussed in the context of the mechanical data registered during the deformation procedure and thermodynamic and kinetics models of melting in the system Ab-Or-H_2O. Microstructural and chemical observations reveal localized melt formation along brittle shear fractures, the generation of gouge and newly-crystallized grains, and complex chemical changes of the starting materials. Discussion focuses on the coupling between deformation, cracking and partial melting, as well as the possible role of dissolution-precipitation as a deformation process.

Chapter 5**:**

Deformation mechanisms and chemical compositional changes in melt bearing feldspar gouges: an experimental study

The aim of this chapter is to examine in detail the deformation mechanisms and mechanical development occurring in fine-grained melt bearing gouges like those formed along the shear

fractures described in chapter 4. The deformation processes occurring in the gouges were simulated by shearing layers of fine grained feldspar gouge of different chemical composition. Microstructural observations show widespread evidence that dissolution-precipitation creep is the dominant deformation mechanism in the gouges, including the growth of new chemically-distinct grains and indented grain boundaries.

CHAPTER 2

Experimental procedures

2.1 Introduction

In this chapter the experimental techniques used in this thesis are described. First, a brief introduction and a general description of the deformation apparatus is given. Secondly, the experimental samples as well as the sample assembly are presented. The third part of the chapter is dedicated to the experimental procedures, as well as a brief description of the data acquisition, processing and evaluation techniques. Details of individual experiments can be found in Chapters 3, 4 and 5.

2.2 Deformation apparatus

All experiments were performed with one of two Griggs-type solid medium deformation apparatus (or "Griggs Rig") at the University of Tromsø, Norway. The "Rigs", which were designed by D.T. Griggs in the late 1960s (Griggs 1967), are an adaptation (by adding an inner moving piston) of the solid confining medium piston-cylinder apparatus of Boyd and England (1960). Additional improvements and modifications were made by Griggs and Blacic (Green et al. 1970) and Tullis and Tullis (1986). The apparatus are designed to reach confining pressures of up to 2.0 GPa and temperatures of up to 1200 °C and therefore represent ideal machines for the study of plastic deformation in quartz and feldspar. An overview of the apparatus (Rig 2) is given in figure 2.1a.

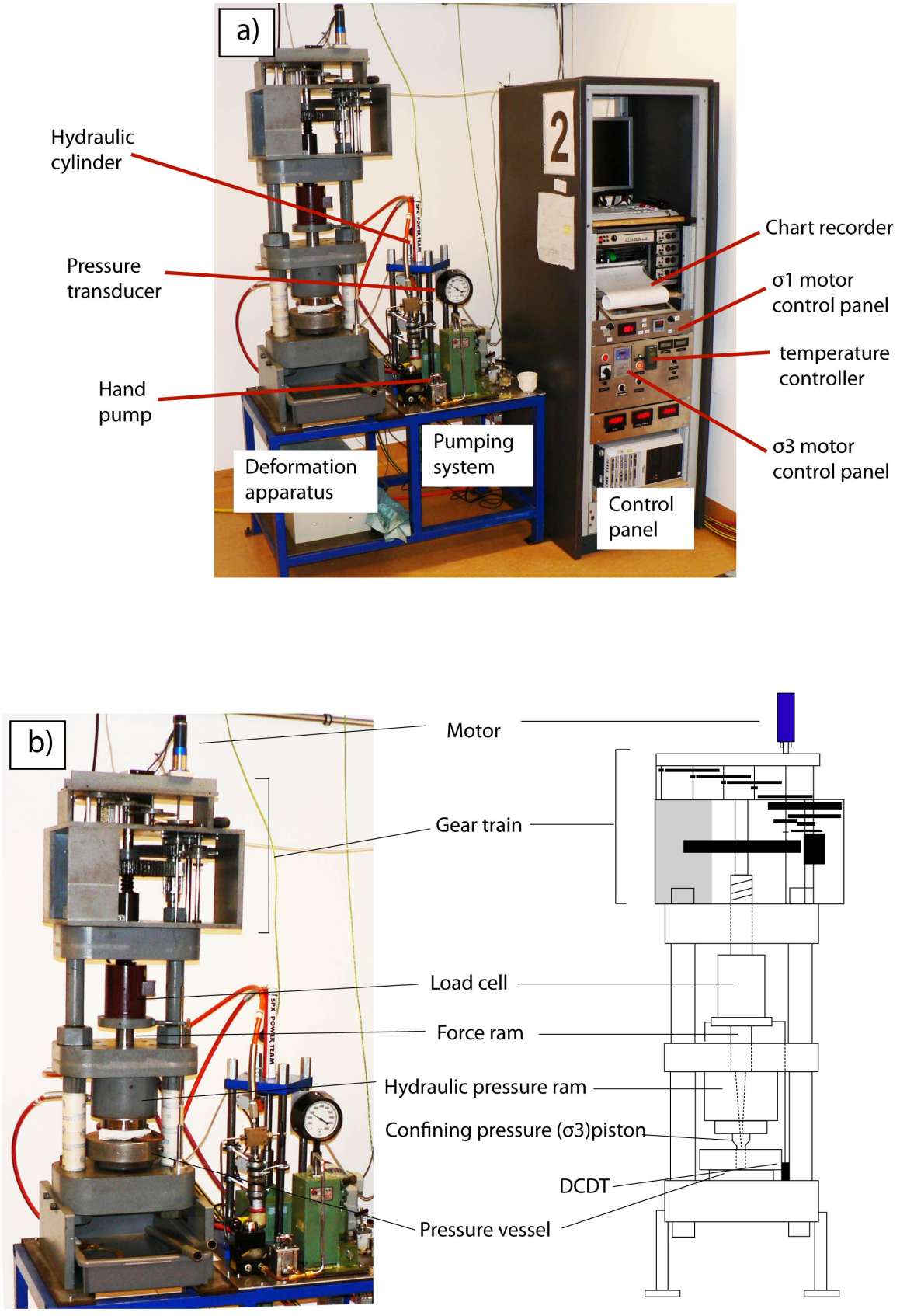

Fig. 2.1 Griggs-type solid medium deformation apparatus. **(a)** Overview of the "RIG 2". **(b)** Detail of the deformation apparatus modified after Holyoke and Kronenberg (2010)

The two "Griggs" at the University of Tromsø have very similar design and functionality. The only differences are a digital linear transformation measurement system (DLT) mounted in Rig 2, slightly thinner tie bars in Rig 1 in order to permit the use of an internally cooled pressure vessel, some minor differences in the mechanical settings (e.g., different design of the pumping system, different hydraulic cylinder) and slightly different apparatus compliance (which is corrected during the data evaluation). The corrected data from both apparatus show good reproducibility indicating that both apparatus are well calibrated.

The high confining pressures (Pc) are produced by pumping oil into an oil chamber. The pumping process can either be performed manually with a hand-pump or controlled automatically with a motorized hydraulic cylinder (Fig. 2.1a). By pumping oil in to the oil chamber the hydraulic ram moves down and presses the confining pressure (σ_3) piston into the pressure vessel (Fig. 2.1b). The confining pressure piston presses on the salt liners (solid confining medium) around the samples transmitting the confining pressure to the sample. The confining pressure is determined and controlled with an external pressure transducer that measures the oil pressure in the oil chamber (Fig. 2.1a), taking into account the relative areas of ram and piston.

The high temperatures are generated by resistance heating using a straight tubular graphite furnace placed around the sample (Fig. 2.5). The temperature inside the pressure vessel is measured using an S-type thermocouple placed next to the sample (Fig. 2.5) and is monitored using a Eurotherm PID- temperature controller (Fig. 2.1a). Due to the high heat conductivity of the piston pressing on the sample, a thermal gradient is produced. A double thermocouple experiment, in which one thermocouple was placed in the center and the other at the lower end of the sample, revealed a temperature difference of ~10 % across a vertical distance of ~6 mm. As the temperature gradient is constant at all temperatures the exact temperature in any part of the deformed sample can be calculated and determined. Because high temperatures lead to dilation of the metal pieces of the deformation apparatus, which would result in variations of confining pressure, the pressure vessel as well as the hydraulic confining pressure ram are cooled with an externally connected water system.

The non-hydrostatic stress on the sample is produced by pressing an inner σ_1 piston (which runs through the center of the σ_3 piston) into the sample assembly. The force actuator is driven by a servo controlled motor connected to the gear-train of wheels (Fig. 2.1b). The velocity of the σ_1 piston (displacement rate) can be adjusted by choosing different gear combinations in the gear train, and it

is controlled automatically and kept constant by the servo controlled motor (Fig. 2.1a). The force on the inner piston is measured using an external load cell located above the hydraulic ram, and the axial displacement of the pistons is measured with a displacement transducer (DCDT, Fig 2.1b).

2.3 Starting materials

In this work two different types of deformation experiment were conducted: (a) axial compression experiments performed on intact crystals and (b) shear experiments performed on rock powders. A schematic representation of both types of sample assembly used for this thesis is presented in figure 2.2.

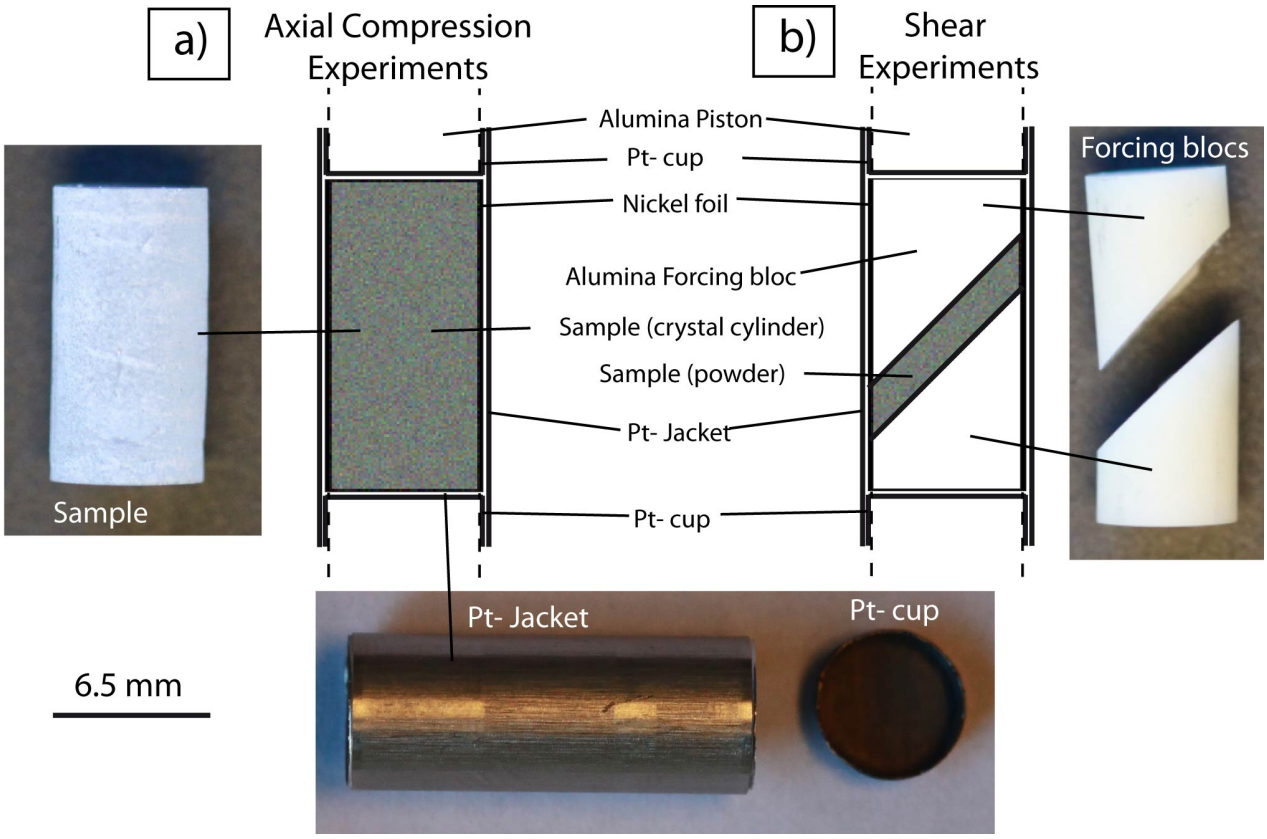

Fig. 2.2 Scale diagram of the two sample geometries used in the experiments. **(a)** Geometry used for axial compression experiments. **(b)** Geometry used for shear experiments on powders.

The samples used for axial compression experiments (Fig. 2.2a) consist of a cylinder cored from natural single crystals with a diamond coring tool and water as lubricant. The cylinders used for

the experiments have a diameter of ~6.3 mm and a length of 12-13 mm. The ends of the cylinders are ground flat and parallel. For this work three different natural single crystals were used: a pink K-feldspar (Fig. 2.3a, chapters 4, 5), a white K-feldspar (Fig. 2.3b, chapter 4) and quartz (Fig. 2.3c, chapter 3). Further specifications about the starting materials can be found in the respective chapters.

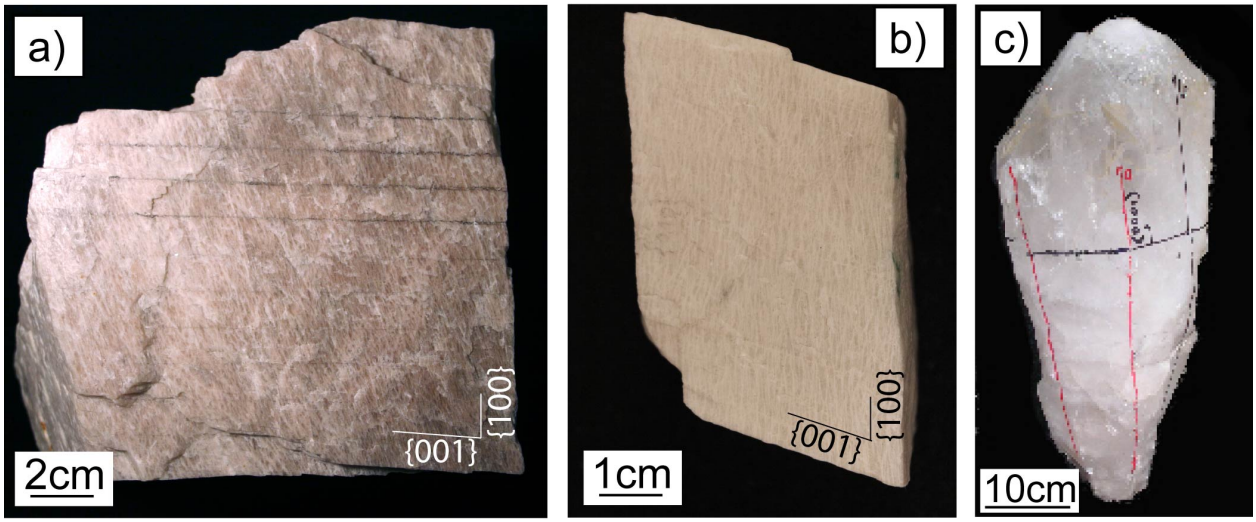

Fig. 2.3 Starting material used for axial compression experiments. **(a)** Pink K-feldspar. **(b)** White K-feldspar. **(c)** Quartz, from Thust (2012)

Shear experiments (Fig. 2.2b; chapter 5) were performed on powders of pink K-feldspar (Fig. 2.3a), gem-quality labradorite (Fig. 2.4a), and albitite (Fig. 2.4b).

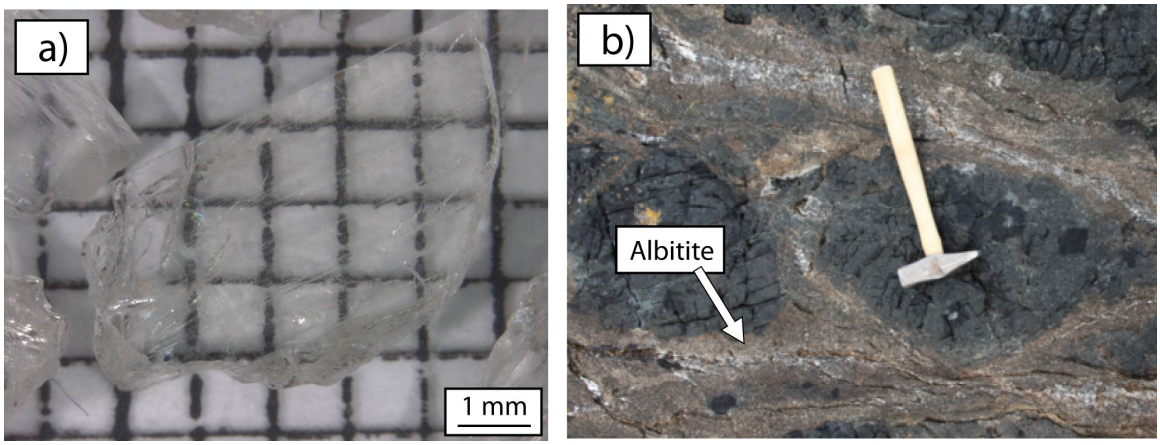

Fig. 2.4 Starting material used for shear experiments on powders. **(a)** Gem-quality Sonora labradorite. **(b)** Albitite from Priyatkina et al. (2011)

The powder is obtained by crushing the starting material first with a hammer and then by milling in an agate or porcelain mortar for about 15 min. The powder is then added to distilled water and passed through a series of sieves and paper filters in order to obtain different grain size fractions. For the experiments described in this thesis the grain size fractions 11-20 μm and 20-100 μm were used. After filtering, the different fractions are dried in an oven at 110 °C for at least 24 h. For the experiments, 0.1 g of dry powder is placed in-between two precut forcing blocks of alumina (Al_2O_3; Fig. 2.2b). The forcing blocks were prepared by sawing a 14 mm long alumina piston at an angle of 45°, whose ends were previously ground flat and plane parallel.

In both single crystal and powder experiments the samples are wrapped in a thin layer of Nickel foil and weld-sealed in a can-shaped Platinum (Pt) jacket (Fig. 2.2). In the case of "wet" experiments the desired amount of distilled water is added to the sample prior to weld-sealing. The distilled water is added to the lower part of the samples using a micro-pipette in order to prevent evaporation during the welding process. In some experiments performed with quartz single crystals (chapter 3), TiO_2 powder was added carefully around the cylindrical samples with the help of a small spatula. The weld sealing process is performed with a Lambert precision welding apparatus using a low current in order to avoid heating of the sample and to minimize water loss during the process.

2.4 Sample assembly

The sample assembly, which during the experimental procedure is placed into the cooled pressure vessel, is represented in Figure 2.5. The jacketed sample (Fig. 2.2) is placed in between two alumina (Al_2O_3) pistons, which transmit the applied force to the sample. Alumina was chosen for its high strength and low thermal conductivity. The sample and pistons are then wrapped in 3 inner NaCl pieces. The inner diameter of the 3 sleeves is slightly different: the two NaCl pieces surrounding the pistons have a diameter of ~6.5 mm, whereas the piece surrounding the jacketed samples has a inner diameter of ~7 mm. The different diameters are chosen in order to perfectly confine the sample and pistons and avoid formation of cracks during the initial stage of the pressurization process. The sample and three inner salt liners are then placed inside a cylindrical graphite furnace consisting of an inner and outer pyrophyllite tube and a central graphite tube. The furnace (containing the sample, alumina pistons and inner salt pieces) is then wrapped in an outer salt cell consisting of two NaCl pieces. The S-type Pt-Pt (10%) Rh thermocouple is placed in contact

with the sample by drilling a small vertical hole through the wall of the lower outer salt piece, as well as a horizontal hole through the furnace and in to the middle inner salt piece. The position of the thermocouple (which ideally is in the center of the sample) is regulated by changing the length of the lower alumina piston with respect to the upper margin of the lower salt piece.

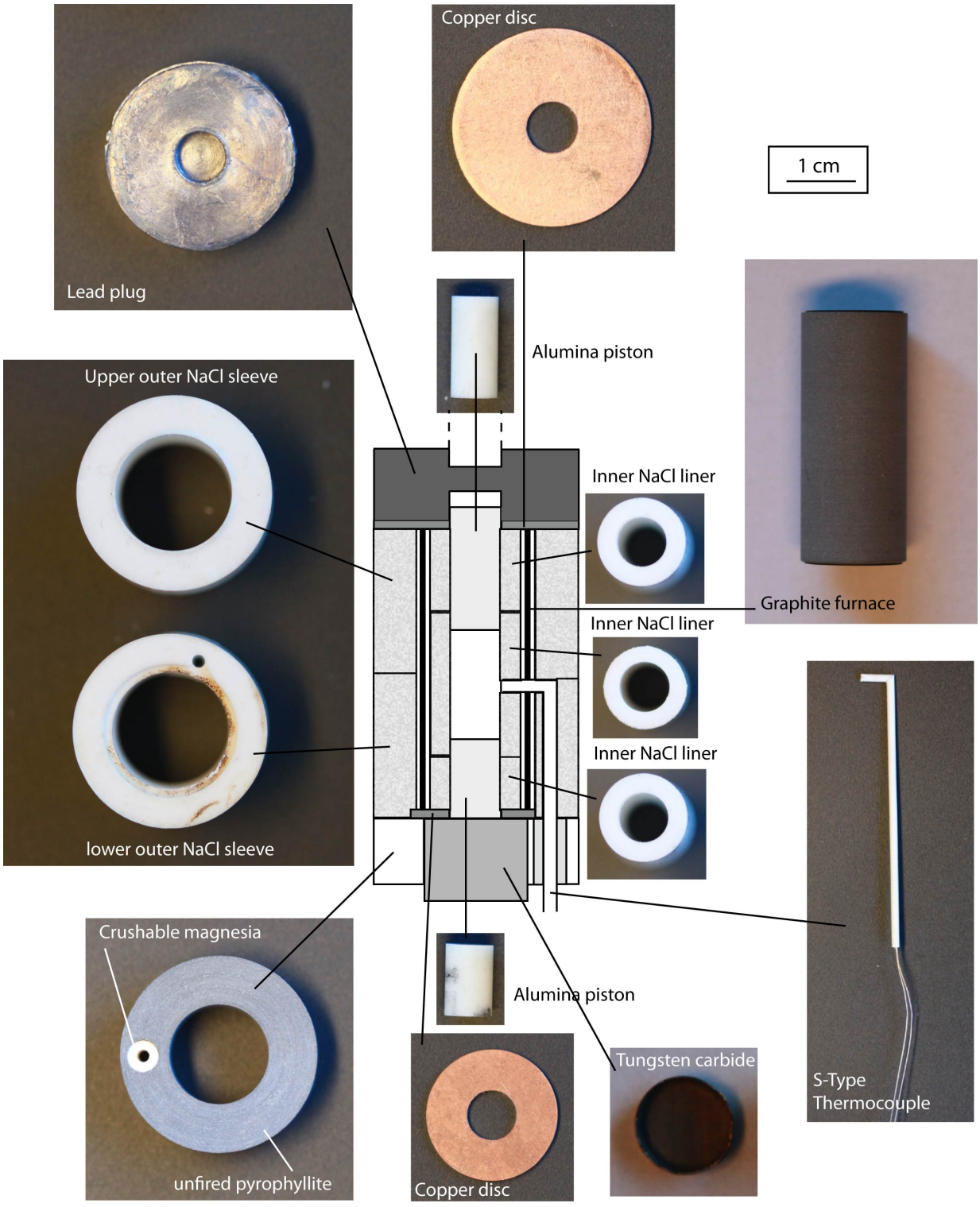

Fig. 2.5 Scale diagram of the sample assembly

On the top and bottom of the graphite furnace two copper disks (small disk on the bottom, larger disk on top) are inserted in order to allow transmission of the current between the furnace and the pressure vessel. Inside the pressure vessel, the entire sample assembly sits on top of a tungsten carbide base plug that is inserted in the center of an unfired phyrophyllite base ring. A 17-mm thick upper lead (Pb) plug with a central hole isolates the sample assembly from the external atmosphere. For the experiments described in this thesis two pressure vessels with slightly different designs were used. One pressure vessel has an internal cooling system, whereas in the other the cooling water circulates in an upper aluminum plate screwed to the top of the pressure vessel. The different pressure vessel designs do not influence the deformation behavior of the samples.

2.5 Experimental deformation procedure

The pressure vessel containing the sample and sample assembly is placed in the "rig" below the hydraulic ram (Fig. 2.1a). The water-cooling tubes as well as the electricity cable for heating are then connected to the pressure vessel, and the system is cooled down to the water temperature (generally 9-10 °C).

At the beginning of each experiment the confining pressure is carefully raised manually up to 0.1 GPa in approximately 1 h time. Then the furnace is switched on and the sample is heated up to 200 °C in 8 min. The pressure is then raised very slowly using a motor-driven pumping system in order to prevent damage to the sample, the furnace and the thermocouple. Generally the pressure is raised in steps of about 0.1 GPa and the temperature in steps of 100 °C with a gradient of 25 °C/min. During the pumping process the σ_1 piston is advanced from time to time to avoid stripping off the σ_1 packing ring. The loading process is normally accomplished in 6-8 hours.

Upon reaching the desired hydrostatic pressures and temperatures, the apparatus is left to equilibrate for 1-2 hours so that the oil pressure and axial load settle down and stabilize. In experiments performed on powder, hot pressing of the sample is necessary in order to decrease the porosity of the starting material. For this purpose the powder experiments are held at the pre-determined hydrostatic conditions for a period of up to 76 hours prior to deformation.

After stabilization and/or hotpressing, deformation is started by advancing the σ_1 piston at a pre-set constant displacement rate (strain rate) with the motor. After reaching the desired strain the deformation process is terminated by stopping the advancement of the piston and by the

simultaneous and fast decrease of temperature to 200 °C, which occurs in approximately 2 min. Pressure and load are then slowly decreased to atmospheric condition in order to minimize the formation of unlading cracks in the sample. Finally the sample assembly is pressed out of the pressure vessel and carefully disaggregated with a scalpel to take out the sample. The deformed sample is subsequently cut in half along its length using a diamond saw and thin sections are prepared.

2.6 Data acquisition and processing

During the experiments the force, confining pressure, axial displacement and external temperature are recorded as amplified volt signals in an analogue chart recorder (Fig. 2.1a). The analogue chart data (Fig. 2.6a) are used during the experimental procedure to directly define the run in curve, hit point, differential stress and strain. Simultaneously the data are also registered digitally by the computer program LabVIEW with one data point recorded every 0.5-1.0 sec (Fig. 2.6b). The deformation temperature registered at the thermocouple tip, the furnace power unit (output value of the heating system) as well as the vertical movement of the load-cell with respect to the frame of the deformation apparatus are registered manually during the pumping and subsequent deformation process.

At the beginning of the deformation process the σ_1 piston advances through the upper lead (Pb) plug. Initailly the curve registers a rapid increase because of the high friction in the apparatus and between the pistons. When the piston starts to push into the Pb plug the load curve has a gentle slope as it registers the constant–rate movement of the σ_1 piston through the Pb plug. This part of the chart is called the “run-in curve” (Fig. 2.6b).

At a certain point the ductile Pb plug is squeezed out and the σ_1 piston starts to touch the upper alumina piston, which is in direct contact with the sample. At this point, called the “hit point”, the load rises until the sample begins to yield (Fig. 2.6b). In our experiments the “hit point” is not sharp, because the lead plug strain-hardens exponentially as it becomes very thin when it is squeezed out between the pistons (Fig. 2.2). To determine a discrete hit point it is assumed that the “run in“ phase can be linearly extrapolated (Fig. 2.6b). The hit point is then determined as the intersection between the linearly extrapolated “run in phase” and the best fit to the initial linear part of the loading curve (Fig. 2.6b). During the deformation process the confining pressure show slight variations due to changes in the room temperature and extension of the apparatus during loading.

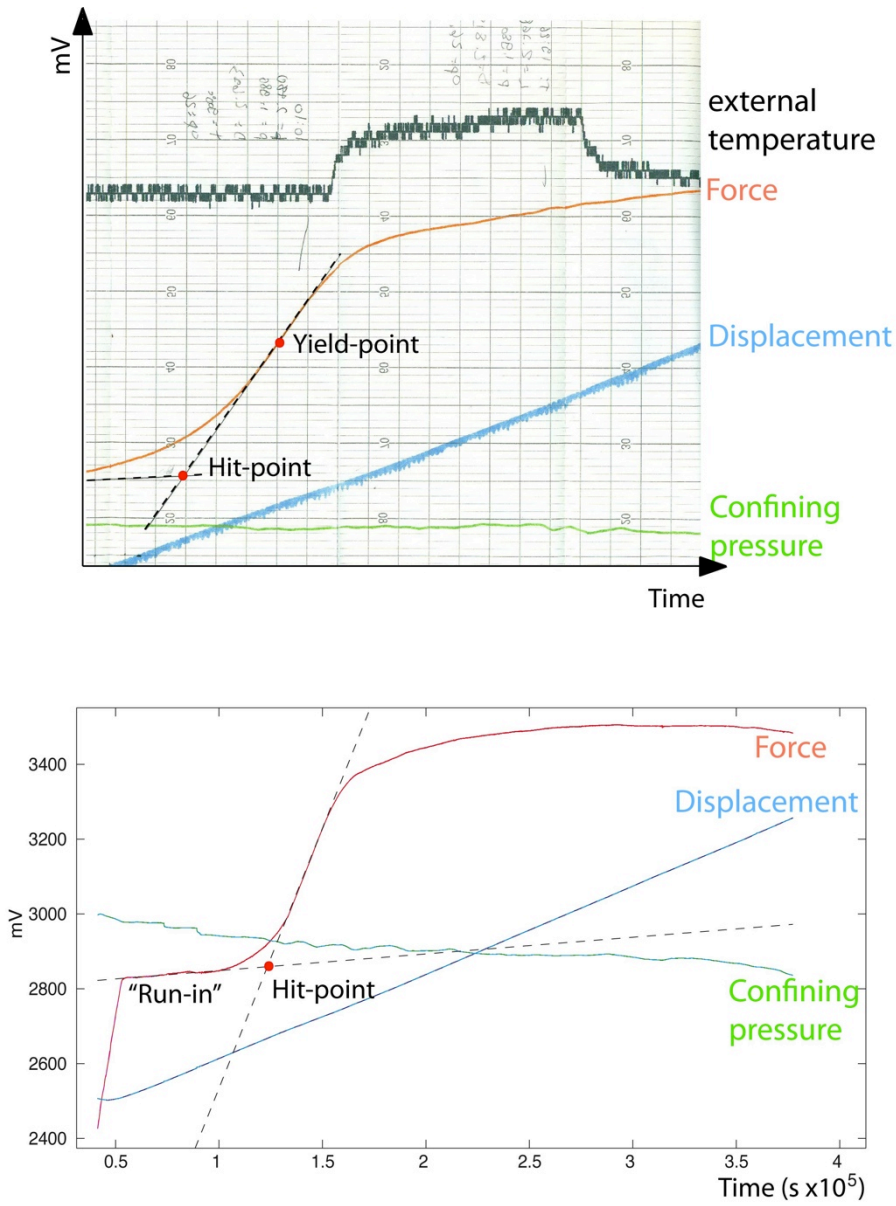

Fig. 2.6 Chart records. **(a)** Analogue chart record. **(b)** Digital chart record

The signals (force, confining pressure and displacement) registered by the computer program are corrected and converted to stress, strain and strain rate using the Matlab program RIG (http://sites.google.com/site/rigprogram/). The program corrects the raw data for elastic distortion of the apparatus and internal friction. In addition, the differential stress is corrected for changes in sample area and confining pressure during deformation. Full details regarding corrections and evaluation of the mechanical data can be found in Pec (2012). The corrected and converted digital data were used for the construction of the stress-strain diagrams presented in this thesis.

CHAPTER 3

The effect of deformation on the TitaniQ geothermobarometer: an experimental study

Marianne Negrini [1], Holger Stunitz [1], Alfons Berger [2,3], Luiz F.G. Morales [4]

[1] Institutt for geologi, Universitetet i Tromsø, N-9037 Tromsø, Norway

[2] Department of Geography og Geology, 1350 København, Denmark

[3] Institut für Geologie, Universität Bern, 3012 Bern, Switzerland

[4] GFZ German Research Center For Geosciences, Section 3.2, 14473 Potsdam, Germany

3.1 Abstract

In order to investigate the effects of deformation on the TitaniQ geothermobarometer, and to study the relationships between different deformation mechanisms and incorporation of Ti into recrystallized quartz grains, we performed high strain (up to 47 %) axial compression experiments on natural quartz single crystals with the addition of rutile powder (TiO_2) and ~0.2 wt% H_2O. Experiments were performed in a Griggs-type solid medium deformation apparatus at confining pressures of 1.0 - 1.5 GPa and temperatures of 800-1000 °C, at constant strain rates of 1 x 10^{-6} or 1 x 10^{-7} s^{-1}.

Mobility of Ti in the fluid phase and saturation of rutile at grain boundaries during the deformation experiments are indicated by precipitation of secondary rutile in cracks and along the grain-boundaries of newly recrystallized quartz grains. Microstructural analysis by light and scanning electron microscopy (the latter including EBSD mapping of grain misorientations) show that the strongly deformed quartz single crystals contain a wide variety of deformation microstructures, and show evidence for subgrain rotation (SGR) and grain boundary migration recrystallization (GBMR). In addition, substantial grain growth occurred in annealing experiments

after deformation. The GBMR and grain growth are evidence of moving grain boundaries, a microstructure favored by high temperatures.

Electron Microprobe Analysis (EMPA) shows no significant increase in Ti content in recrystallized quartz grains formed by SGR or by GBMR, nor in grains grown by annealing. This result indicates that neither SGR nor moving grain boundaries during GBMR and grain growth are adequate processes to facilitate re-equilibration of the Ti content in experimentally deformed quartz crystals at the investigated conditions. More generally, our results suggest that exchange of Ti in quartz at low H_2O contents (which may be realistic for natural deformation conditions) is still not fully understood. Thus, the application of the TitaniQ geothermobarometer to deformed metamorphic rocks at low fluid-contents may not be as straightforward as previously thought and requires further research.

3.2 Introduction

The reconstruction of metamorphic pressure-temperature (P-T) paths, especially in conjunction with the deformation history of rocks, is one of the primary tasks of tectonics and structural geology research. The pressures and temperatures of deformation can in some cases be determined with a reasonable degree of accuracy, based on the chemistry of coexisting mineral phases (conventional thermobarometry) or by thermodynamic modeling based on the properties of minerals (P-T-X pseudosections). However, the relationships between P-T conditions and deformation can only be established if the synkinematic nature of the mineral assemblage is demonstrated. The geothermobarometer titanium-in-quartz (TitaniQ), based on the temperature (Ostapenko et al. 2007; Wark and Watson 2006) and pressure dependence (Thomas et al. 2010) of Titanium (Ti^{4+}) substitution for tetrahedral Silicon (Si^{4+}), has the potential to determine the temperature and pressure of the deformation process directly (Kohn and Northrup 2009). This geothermobarometer is expected to be reset by dynamic recrystallization of quartz under a wide range of conditions that are well characterized (e.g., Hirth et al. 2001; Hirth and Tullis 1992; Stipp et al. 2002; Stipp and Tullis 2003). Since its introduction the TitaniQ geothermobarometer has been extensively applied to the analysis of plutonic rocks (e.g., Huang and Audétat 2012; Jacamon and Larsen 2009; Kawasaki and Osanai 2008), volcanic rhyolites (e.g., Campbell et al. 2009; Girard and Stix 2010; Smith et al. 2010; Vazquez et al. 2009; Wark et al. 2007; Wilson et al. 2012), hydrothermal quartzite (e.g., Barker et al. 2010; Rusk 2006), metamorphic rocks (e.g., Adachi et al. 2010; Sato and Santosh 2007; Spear and

Wark 2009; Storm and Spear 2009), and deformed rocks (e.g., Grujic et al. 2011; Härtel and Herweg submitted; Kohn and Northrup 2009; Menegon et al. 2011; Pennacchioni et al. 2010).

Several studies report P-T conditions calculated with the TitaniQ geothermobarometer that are in good agreement with data from other geothermobarometers (e.g., Campbell et al. 2009; Huang and Audétat 2012; Menegon et al. 2011; Vazquez et al. 2009). On the other hand, some studies have reported discrepancies between TitaniQ and other geothermobarometers (e.g., Grujic et al. 2011; Wilson et al. 2012). Conflicting results may arise from the relative difficulty of determining the Ti activity in the system when rutile is not present (e.g., Thomas and Watson 2012), from the growth rate of the quartz crystals (Huang and Audétat 2012), from mobilization of trace elements including Ti in the crystal structure (Rossi et al. 2005; Sinha et al. 1986), or from inhibited ionic exchange during formation of the quartz crystals. Mobilization of Ti could be caused by deformation of the quartz crystal structure, but currently there are no systematic experimental studies that investigate the effect of deformation on the TitaniQ geothermobarometer.

The effects of recovery and recrystallization in quartz on resetting of the TitaniQ geothermobarometer have been studied by Grujic et al. (2011). These authors found that at temperatures >500 °C the Ti contents of quartz are reset, which they attributed to grain boundary diffusion during grain boundary migration recrystallization as being an effective mechanism for Ti-exchange. At lower temperatures, they found no resetting of Ti contents, which they explained as a result of slow volume diffusion associated with development of bulging and rotation recrystallization microstructures. This observation challenges the earlier work of Kohn and Northrup (2009), who suggested that the temperatures of mylonitization can be determined using TitaniQ even at relatively low temperatures.

The problem of resetting the Ti-content in quartz during deformation is related to the exchange mechanism of Ti in quartz. In the piston-cylinder experiments performed to calibrate the TitaniQ geothermometer, the water content of the samples was up to 30% (Wark and Watson 2006). In this case the new quartz grains grew from a fluid saturated in Ti and Si. However, Ti-exchange during deformation in natural rocks takes place at considerably lower H_2O-contents, at lower quartz growth rates, and potentially by different exchange mechanisms. Recrystallization by progressive subgrain rotation is not likely to cause rapid ionic exchange, because new grain boundaries form by volume diffusion processes inside the original grains (e.g., Poirier 1985), with limited or no interaction with grain boundary fluids. On the other hand, during grain boundary migration recrystallization (GBM), quartz grains are expected to exchange ions through the moving grain boundary region and any

fluids present (Grujic et al. 2011; Härtel and Herweg submitted). The grain boundary migration process in the presence of an aqueous fluid film may be envisaged as a solution-precipitation process at the grain boundary interface (e.g., Urai et al. 1986). Likewise, grain growth (during, for example, static annealing processes) involves the migration of grain boundaries, and ionic exchange through the grain boundaries and grain boundary fluids is expected.

Based on these considerations, it is to be expected that the ionic exchange rate of Si and Ti will be much slower in quartz grains recrystallized by subgrain rotation (SGR) than quartz grains recrystallized by grain boundary migration recrystallization (GBM) and grain growth. This effect is expected to be compounded by the lower diffusion rate at the typically lower temperature of SGR and bulging recrystallization (at the same strain rate; Hirth and Tullis 1992; Stipp et al. 2010, 2006, 2002) compared to GBM (Grujic et al. 2011).

The aim of this work is to study experimentally the effects of different recrystallization mechanisms (bulging recrystallization, subgrain rotation recrystallization, grain boundary migration recrystallization) on the equilibration of Ti in quartz. We performed deformation experiments on quartz single crystals in the presence of Ti using a modified Griggs-type solid-medium deformation apparatus over a range of conditions that favor the activity of different deformation regimes and recrystallization mechanisms in quartz (Hirth and Tullis 1992; Stipp et al. 2002 a,b).

3.3 Methods

3.3.1 Starting material

The starting material for all experiments was cored from an euhedral natural quartz single crystal from a vein in the Aar Massif, Central Alps, Switzerland. Macroscopically the quartz crystal shows some crystalline inhomogeneity in the form of milky regions distributed randomly throughout the crystal. The varying opacity (milkyness) of the crystal is caused by the presence of H_2O-rich fluid inclusions with lengths of up to 200 µm. For our experiments, the milky regions of the quartz crystal were chosen, because the experiments require the presence of aqueous fluid during deformation. The clear quartz, where no fluid inclusions are observed, is essentially dry, whereas the water content of the milky regions is strongly inhomogeneous and depends on the size and distribution of the fluid inclusions (Thust et al. 2012). Further information concerning the nature and distribution of the fluid

inclusions, as well as mechanical and physical properties of the quartz crystal, can be found in Tarantola et al. (2012) and Thust et al. (2012).

Light microscope observations show that the quartz crystal is optically strain-free and that it contains no solid impurities. In particular, no rutile inclusions were observed. Electron microprobe analyses (EMPA; analytical methods described below) of the quartz crystal reveal uniformly very low Ti contents (below the detection limit of the EPMA of 20 ppm).

3.3.2 Sample preparation

We used two sets of samples during the experiments (Fig. 3.1a), cored in two crystallographic orientations in order to produce different recrystallization microstructures by activating different slip systems. The O^+ sample set, where slip occurs along the basal <a> and prism <c> slip systems, was cored at 45° to the basal plane and to the c-axis of the quartz crystal (e.g., Baeta and Ashbee 1969 a,b; Blacic and Christie 1984; Tarantola et al. 2010; Fig. 3.1a). The normal {m} set (⊥m), where slip occurs along the prism <a> slip system, was cored with the c-axis and one of the prism planes normal to the sample cylinder axis (Fig. 3.1a).

All samples had a diameter of 6.3 mm and a length ranging from 10 -12 mm. Two different sample arrangements were used: some samples consisted of a single cylinder, while in others we placed two short (5-6 mm) cylinders on top of one another to increase the total surface area for reaction with the TiO_2 powder.

The quartz cylinders were placed in a pre-annealed platinum (Pt) jacket and 0.01-0.03 g of fine-grained TiO_2 powder was carefully placed all around the quartz cylinders. In samples formed by two cylinders TiO_2 powder was also placed in between the two cylinders. Distilled H_2O (0.1- 0.3 µl) was added with a micropipette to the lower part of the sample in order to prevent evaporation during the welding process of the Pt-jacket. Mechanical welding was performed with a Lambert welding device using a millisecond welding time to minimize heating of the sample. All the samples were sandwiched between two Al_2O_3 pistons and placed in the center of a graphite furnace. In all experiments we used sodium chlorite (NaCl) liners as the solid confining medium. The sample assembly used in the experiments is illustrated in Fig. 3.1b.

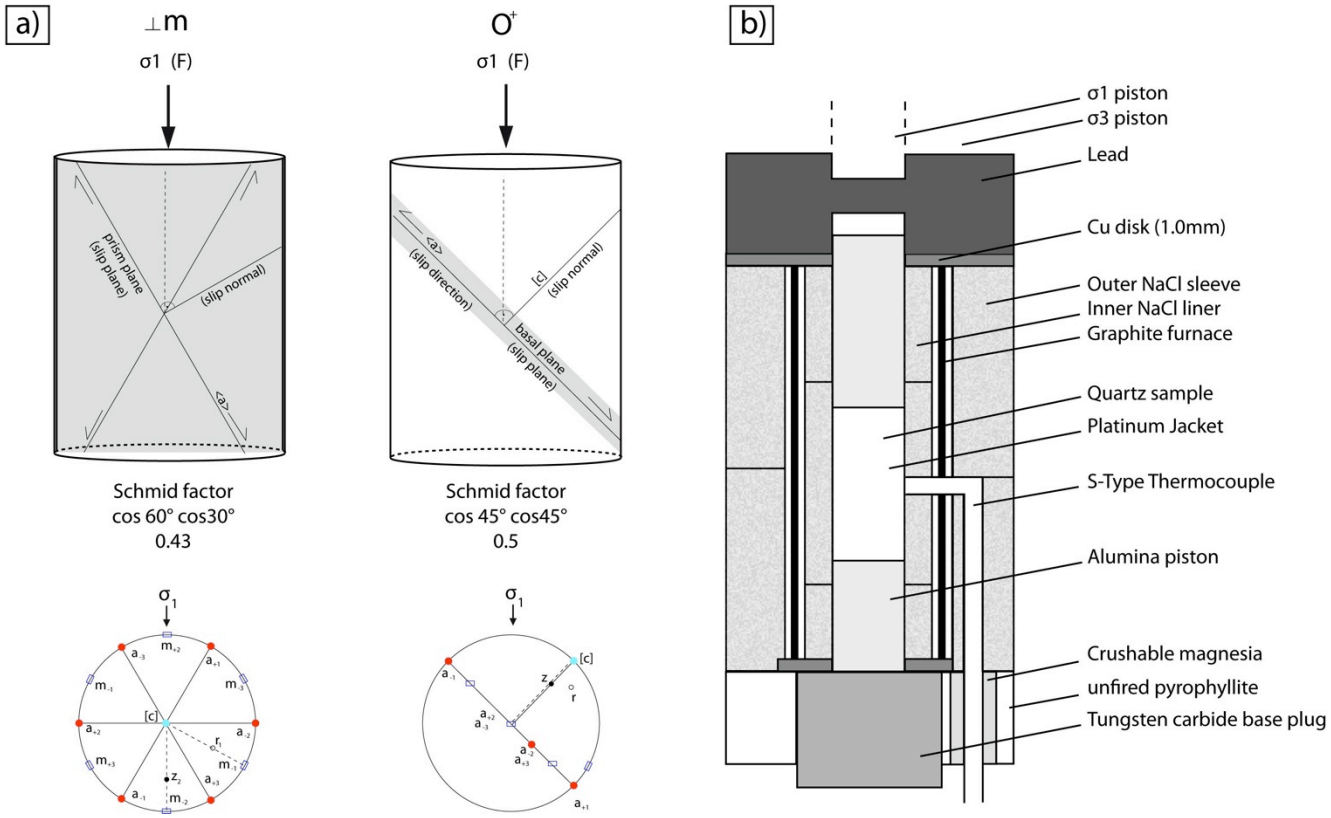

Fig. 3.1 (a) Schematic representation and stereographic projection of the sample orientations used in the experiments, (left) normal {m} and (right) O^+ orientation (modified after Thust et al. 2012). **(b)** Schematic drawing of the sample assembly used in this study for the deformation experiments performed in a Griggs-type solid medium deformation apparatus. Modified after Tarantola et al. (2010).

3.3.3 Experimental set-up

Sample	Pc [Gpa]	T [°C]	Strain rate [$10^{-6}s^{-1}$]	Time [h]				Strain [%]	Experiment type	Orien-tation	TiO_2	H_20
				before hit point	defor-mation	anne-aling	total time					
mn273	1.00	900	0	26	0	0	26	0	hydrostatic	⊥m	0.01g	0.1µl
mn275	1.00	900	1.4	58	60	0	118	32	axial	⊥m	0.01g	0.1µl
mn277	1.00	800	1.4	24	88	0	112	47	axial	⊥m	0.01g	0.1µl
mn299	1.00	900	1.2	33	80	0	113	37	axial	O^+	0.01g	0.1µl
mn301	1.50	1000	1.4	0	90	0	90	28	axial / prehit	O^+	0.01g	0.1µl
mn319	1.50	900	1.2	36	99	76	211	47	axial	O^+	0.02g	0.1µl
mn321	1.20	1000	1.1	24	30	0	54	16	axial / prehit	O^+	0.01g	0.1µl
mn326	1.50	1000	1.4	67	93	0	160	40	axial	⊥m	0.03g	0.1µl
mn331	1.50	1000	0.1	42	244	0	286	20	axial	⊥m	0.02g	0.3µl
mn332	1.50	1000	1.4	0	120	139	259	20	axial	⊥m	0.02g	0.3µl

Table 3.1. Deformation conditions (Pc= confining pressure, T= temperature, ἐ= strain rate, deformation time, and total strain) and sample parameters (sample orientation, added TiO_2 and added H_2O) of all deformation experiments.

High strain (up to 47 %) axial compression experiments were performed with a modified Griggs-type solid medium deformation apparatus (Griggs 1967; Tullis and Tullis 1986) at pressures of 1.0 - 1.5 GPa, temperatures ranging from 800-1000 °C, and constant strain rates of 10^{-6} s^{-1} and 10^{-7} s^{-1}. An overview of experimental conditions is presented in Table 3.1

As one of the main aims of the experiments was to study the effects of different recrystallization mechanisms on re-equilibration of the Ti content in quartz, the range of experimental conditions was chosen in an attempt to activate both subgrain rotation recrystallization and grain-boundary migration recrystallization in quartz according to the conditions determined by Stipp et al. (2002 a,b) and Hirth and Tullis (1992). For the range of experimental conditions used, the expected equilibrium Ti values of quartz (Thomas et al. 2010) and the predicted deformation mechanisms (Hirth and Tullis 1992) are summarized in Table 3.2.

Experimental conditions		Expected Ti [ppm]	Deformation regime	Expected deformation mechanisms
T [°C]	p[GPa]			
800	1.0	147	2	Subgrain rotation recrystallization (SGR)
900	1.0	310	3	Grain boundaries migration (GBM) + SGR
900	1.5	127	3	Grain boundaries migration (GBM) + SGR
1000	1.5	256	3	Grain boundaries migration (GBM) + SGR

Table 3.2. Ti-content and deformation behavior expected for quartz, deformed in the temperature range 800 to 1000 °C and at different confining pressures (1.0 – 1.5 GPa). Ti-content calculated as: $RT \ln X^{quartz}_{TiO2} = -60952 + 1.520 * T(K) - 1741 * p(kbar) + RT \ln a_{TiO2}$ (Thomas 2010), where a_{TiO2} was = 1 because rutile is present in all samples, R= 8.3145 J/K (gas constant), T is temperature in °K, and P is confining pressure in kbar. To convert X^{quartz}_{TiO2} into Ti [ppm] the formula of Thomas (2010) was used. Expected deformation regime and deformation mechanisms based on the experimental work of Hirth and Tullis (1992).

During each experiment, confining pressure and temperature were increased in a step-wise manner until the desired deformation conditions were reached, typically in ~8 hours. As the samples were fluid bearing, heating was started after reaching confining pressures (Pc) of at least 0.2 GPa in order to minimize the internal pressure of the capsule. Temperature was increased in steps of 100 °C at a rate of 25 °C per minute.

Temperature was monitored with a Pt-Pt10%Rh S-type-thermocouple placed in the center of the sample. In order to verify the thermal gradient in the sample during deformation, a double thermocouple experiment was performed in which one thermocouple was placed in the center and the other at the lower end of the sample. The results of this test show a maximum temperature difference of ~10 % from the center of the sample to the alumina piston (a distance of ~6 mm).

After reaching the desired conditions deformation was started by advancing the axial piston (σ_1) at a constant strain-rate (10^{-6} s^{-1} or 10^{-7} s^{-1}). During deformation, mechanical data (force applied to the sample, displacement of the piston, confining pressure, and external room temperature) were registered at 1 sec intervals. Once the desired total strain was achieved, in most experiments the temperature was quenched to 200 °C in 2 minutes or less in order to preserve the deformation microstructures. In two deformation experiments temperatures were held after deformation at 900 °C for 76 hours (mn319) and 1000 °C for 139 hours (mn332) in order to induce annealing and grain growth of the recrystallized grains and thus movement of grain boundaries.

Mechanical data were processed using the Matlab program RIG (http://sites.google.com/site/rigprogram/) taking into consideration internal friction and distortion of the deformation apparatus. Differential stress was corrected for changes in sample area and confining pressure during deformation. Full details regarding corrections and evaluation of the mechanical data can be found in Pec et al. (2011).

3.3.4 Analytical methods

Deformed samples were cut parallel to the loading direction (parallel to the sample cylinder axis) through the middle of the sample and polished thin sections were prepared with a thickness of 30 μm.

Major and trace element analyses were performed with a JEOL Superprobe JXA 8200x at the University of Copenhagen using an acceleration voltage of 20 kV, a beam current of 200 nA, a beam diameter of 3-15 μm, and counting times of 240 s on the peak and 120 s on each high and low background positions. Standardization was performed on rutile and SiO_2 using the same conditions as above. At these conditions the given detection limit of the instrument is on average 20 ppm for Ti.

EMPA analysis was chosen instead of Secondary Ion Mass Spectrometry (SIMS) and Laser Ablation Inductively Coupled Plasma Mass Spectrometry (LA-ICP-MS), because: (1) EMPA offers the best spatial resolution (smallest interaction volume) of these methods. One of the difficulties in measuring Ti in quartz is to avoid interaction of the measuring beam with the grain boundary regions, which are sites of potential rutile precipitation. In our case, EMPA allowed measurements of the internal parts of grains and near grain boundaries of small (several μm) recrystallized grains. (2) At the chosen experimental conditions, the expected equilibrium Ti values in quartz are high (varying from 127 to 310 ppm; Table 2) and well above the detection limit of the microprobe (20 ppm Ti), and in a range of sufficient quantitative resolution for the purpose of this study.

As reported previously (Bastin et al. 1984; Donovan et al. 2011; Fournelle 2007; Hermann et al. 2005; Wark and Watson 2006) Ti contents measured by EMPA have to be treated with care because of the "phantom" Ti-content (often described as secondary fluorescence, e.g., Hayden and Watson 2007; Sato and Santosh 2007; Wark and Watson 2006), which causes erroneously high Ti concentrations in quartz in the vicinity of Ti-phases. These effects are observed in the samples analyzed here (e.g., Figs. 3.2b, 3.5c, 3.6b, 3.9a). The element distribution maps (Figs. 3.2b, 3.6b) of the deformed quartz single crystals show spurious Ti-haloes around rutile inclusions, and locally along cracks that developed in the quartz crystals during deformation. EMPA point measurements along the spurious haloes show high Ti contents (thousands of ppm) and an interaction distance varying from 100 μm in zones adjacent to large rutile aggregates to a few μm around small rutile inclusions (Fig. 3.2c). As proposed by Cherniak et al. (2007) volume diffusion of Ti in quartz is very slow and negligible in our short experiments (1-11 days). Thus, the observed high Ti contents around rutile grains arise from "phantom" Ti in quartz and therefore have to be considered as an analytical artifact (see Figs. 3.5c, 3.9a). For this work, however, phantom Ti content does not present a significant problem, because the high Ti-values can always be correlated with detectable rutile inclusions or fine grained rutile precipitates along grain boundaries. Furthermore, as is shown below, Ti contents in all cases are lower than the expected equilibrium values and any correction for "phantom" Ti in quartz would result in even lower values.

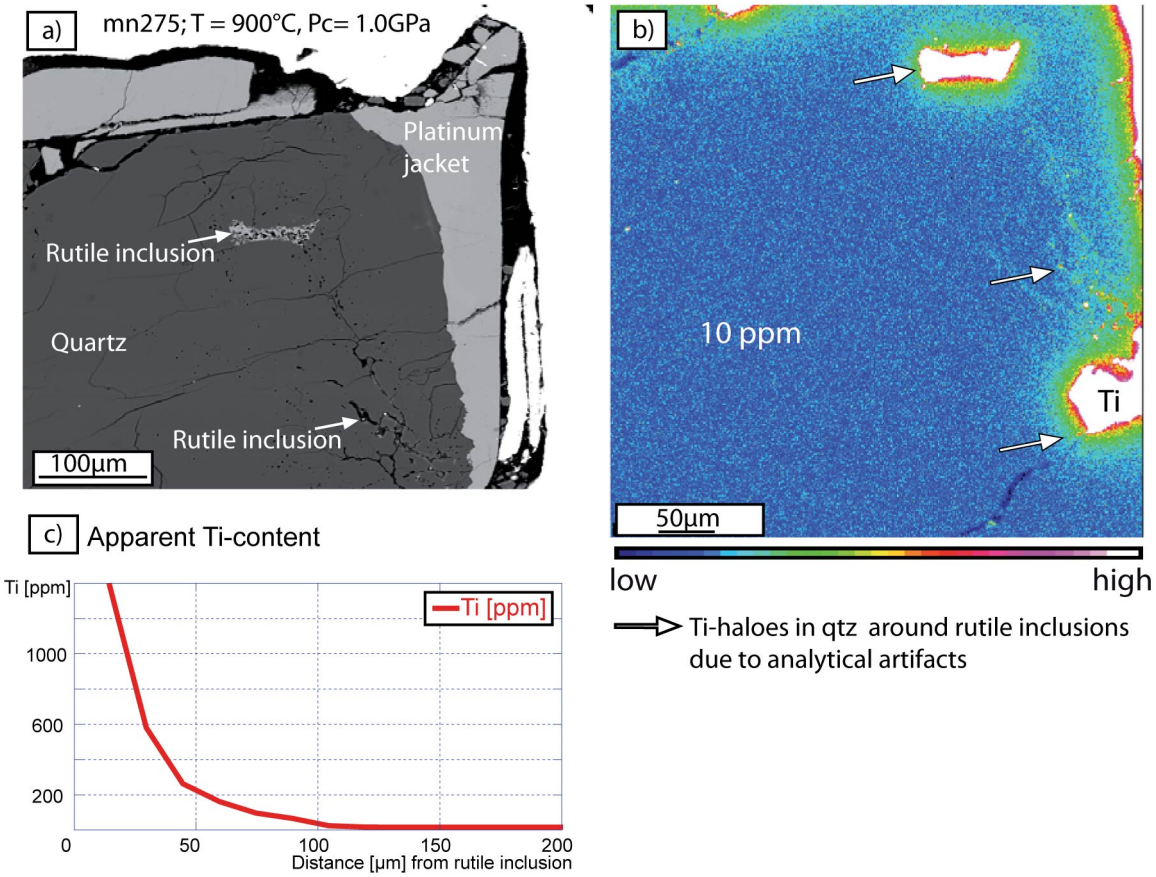

Fig. 3.2 Apparent spurious Ti-content in quartz (see Hermann et al. 2005) around rutile inclusions in sample mn275 deformed in presence of TiO_2 powder and fluid (H_2O) at 900 °C, 1.0 GPa. **(a)** Backscatter image of a large rutile inclusion formed inside the quartz single crystal during deformation and recrystallisation. The 100 μm long inclusion consists of randomly oriented, 10 μm long needles of rutile. Small rutile inclusions are found also along cracks (arrows). **(b)** Element distribution map showing the effect of spurious Ti in quartz around the rutile inclusion and the sample boundary due to the presence of phantom Ti in quartz. The Ti scale threshold was chosen in order to highlight the analytical artifacts and therefore cannot been linearly related to Ti contents measured in the sample. The distortion of the element map is caused by a difference in the imaging systems of the microprobe. **(c)** Spurious Ti content caused by phantom Ti in quartz. The effect is noticeable up to 100 μm distance from the rutile for large inclusions. Therefore, all measurements taken closer than 100 μm from large rutile grains are subject to error.

Initial microstructural observations of the deformed samples were made with a polarization light microscope. Crystallographic preferred orientation (CPO) analysis of selected samples was carried out using electron backscatter diffraction (EBSD; Adams et al. 1993; Prior et al. 1999) in a scanning electron microscope. For EBSD analysis we used a FEI Quanta 3D FEG dual-beam machine equipped with an EDAX-TSL Digiview IV EBSD detector and TSL-OIM system (v. 5.31) installed at the GFZ-Potsdam. After the standard polishing procedure, the thin sections were chemically polished using a soft cloth and an alkaline solution of colloidal silica (SYTON) (Flynn and Powell 1979) for about 3 h in order to remove damages and defects of the section surface caused by the

mechanical polishing. The analyses were conducted under low vacuum (10 Pa of H_2O) allowing the use of uncoated samples. For automatic mapping of crystallographic orientations the following parameters were used: 15 kV accelerating voltage; 8 nA beam current; 12 mm working distance; step size of 1 µm and 70° sample tilt. Post-acquisition treatment included standardization of the confidence index (CI) of different points and CI correlation between neighboring points. Only data with CI>0.2 were considered for further analysis. The pseudohexagonal symmetry effect on quartz caused by a rotation of 60° around [0001] was also corrected.

3.4 Results

3.4.1 Sample deformed at 800 °C and confining pressure of 1.0 GPa

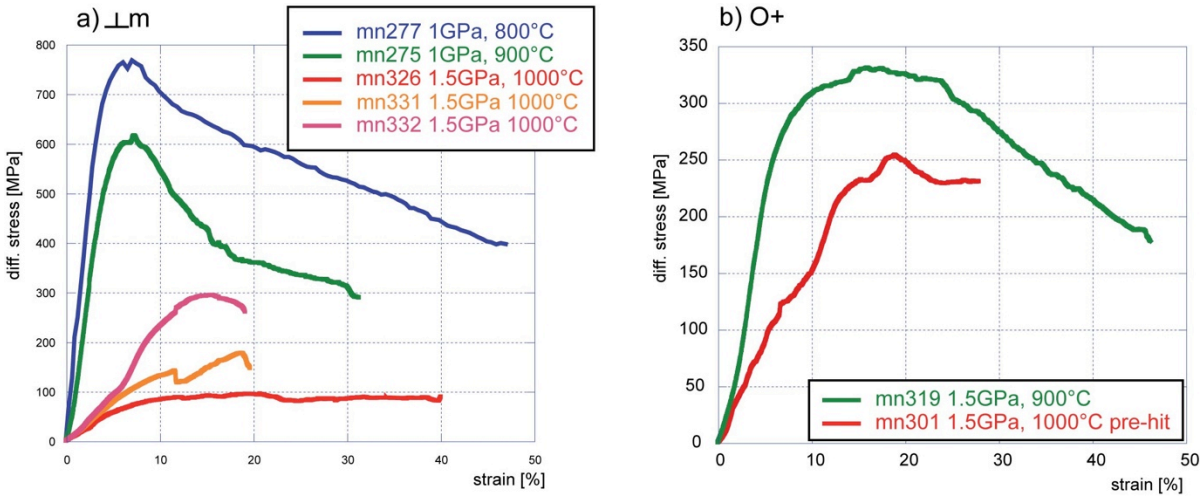

Fig. 3.3 Strain vs. differential stress curves of samples deformed at a strain rate of 1 x 10^{-6} s^{-1}. Axial compression **(a)** normal {m} and **(b)** O^+ orientation. Experiment mn301 was cracked prior deformation (pre-hit). Experiment mn331 was deformed with strain rate stepping (initially at 1 x 10^{-6} s^{-1} and after peak strength at 1 x 10^{-7} s^{-1}).

Quartz sample mn277, deformed up to a strain of 47 % at 800 °C and 1.0 GPa confining pressure, shows a peak strength of 750 MPa, followed by pronounced weakening to ~400 MPa (Fig. 3.3).

The heterogeneously deformed single crystal displays a wide range of deformation microstructures (Fig. 3.4).

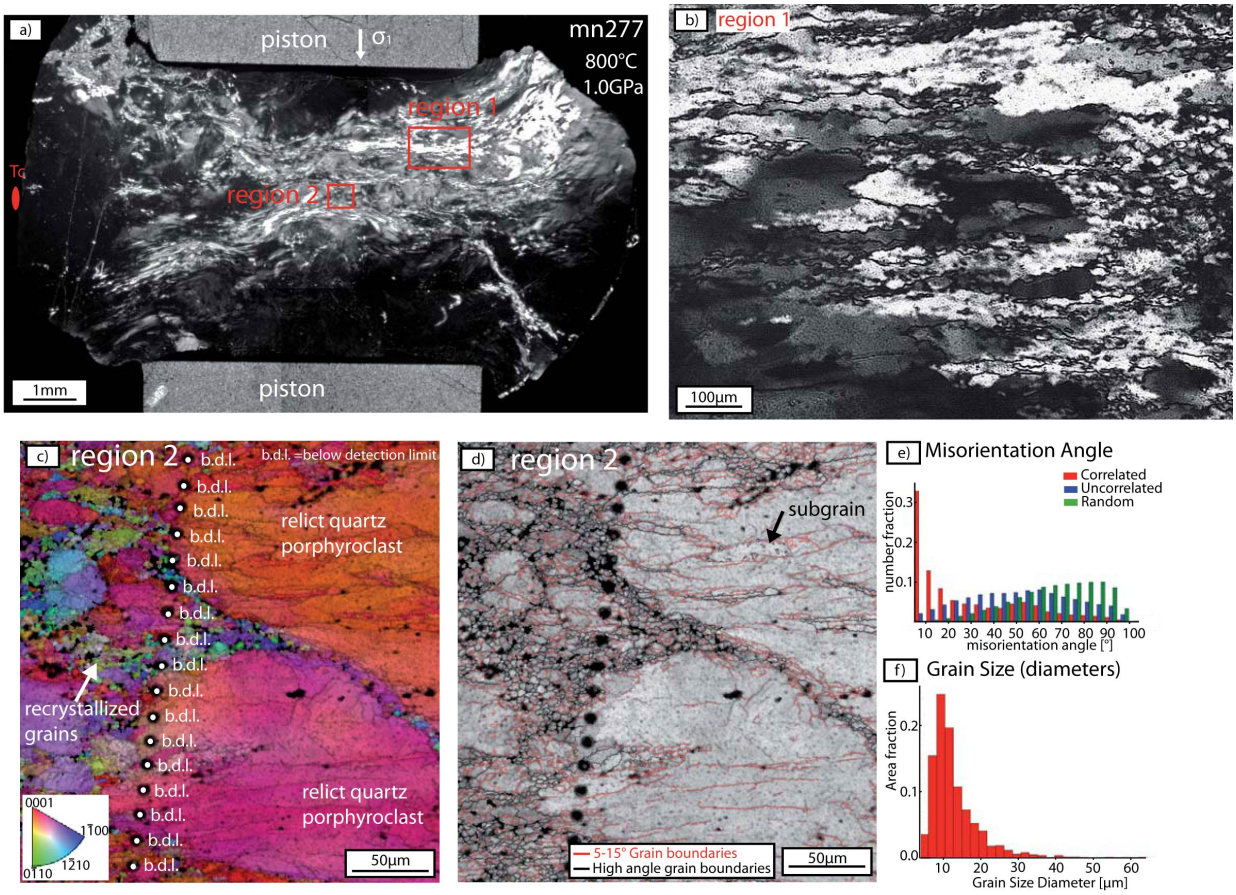

Fig. 3.4 Microstructures and Ti-content of sample mn277 deformed to an axial strain of 47 % at a strain rate of $1x10^{-6}$ s^{-1}, 800 °C, 1.0 GPa in the presence of TiO_2 powder and fluid (H_2O). Compression direction is vertical in all images. **(a)** Light micrograph (crossed polarizers) of sample mn277. Final position of the thermocouple (Tc) and positions of the analyzed regions are marked in red. **(b)** Light micrograph (cross-polarized) of typical microstructures of a strongly deformed part of the sample (region 1). Considering the temperature gradient in the sample, deformation occurred in this region at a temperature of 795 °C. **(c)** EBSD orientation image of region 2. Orientations according to the inverse pole figure given in the lower corner of the image. White numbers indicate the Ti contents (ppm) measured by EPMA. The expected equilibrium Ti content at 800 °C, 1.0 GPa is 147 ppm (Thomas et al. 2010). **(d)** Grain-boundary misorientation map of region 2 acquired with EBSD using nearest neighbor pairs. Misorientation angles of 5-15° are represented in red, misorientation >15° are represented in black. **(e)** Histogram of distribution of angles between nearest neighbor pixels (correlated, red bars) and for uncorrelated pairs (blue bars). Distribution for random orientation is given by green bars. Bins are at 5° interval. Measurements below 5° are omitted, because of inaccuracy (Kruse et al. 2001; Prior et al. 1999) **(f)** Grain size distribution (Area fraction) of the recrystallized region 2.

Strain is mainly accommodated along conjugate deformation bands (Fig. 3.4a), which extend from the piston edges and intersect in the center of the sample. Within the deformation bands, large (100-200 µm) porphyroclasts of relict quartz grains with undulatory extinction are surrounded by domains of small, recrystallized grains (Fig. 3.4b,c,d). Light microscope observations indicate the presence of small solid inclusions (probably rutile) along the boundaries of the newly recrystallized grains.

Undulatory extinction of the large porphyroclasts is caused by a slight change of crystal orientation visible in the orientation map (Fig. 3.4c). The grain boundary misorientation map produced by EBSD (Fig. 3.4d) shows a high density of low angle (5-15°) boundaries (in red) around and within the large quartz relicts. Some boundaries delineate strongly elongated subgrains, with an elongation direction approximately normal to the compression (σ_1) direction. The newly recrystallized grains, with mean grain size ranging from 6 - 12 μm (Fig. 3.4f), are delineated by grain boundaries with a misorientation > 15° (black lines in Fig. 3.4d). Many recrystallized grains have a similar size as the small subgrains with low angle boundaries (Fig. 3.4d). The histogram of the distribution of misorientation angles (Fig. 3.4e) shows a clear deviation from a random distribution and a high frequency of low misorientation angles between adjacent pairs (correlated). The small increase in frequency for misorientation angles between 50 - 60° probably represents Dauphiné twinning (60° rotation about the c-axis; Frondel 1962). The overall distribution of misorientation angles and the predominance of low angle grain boundaries suggest the presence of a crystallographic preferred orientation (CPO) in the recrystallized domains of the sample.

EMPA analyses (Fig. 3.4c) indicate uniformly very low Ti contents (mainly below the 20 ppm detection limit of the instrument) throughout the entire quartz crystal. In addition, no systematic compositional variations between the large porphyroclasts, subgrains, small recrystallized grains, and the undeformed parts of the sample were observed.

3.4.2 Sample deformed at 900 °C and confining pressure of 1.0 GPa

Sample mn275 (Fig. 3.2) was deformed up to a strain of 32 %. The mechanical data (Fig. 3.3) show a similar strength development as sample mn277, with a peak strength of 600 MPa followed by pronounced weakening to ~350 MPa. Deformation was accommodated mainly along a conjugate set of deformation bands oriented at 50° to the compression (σ_1) direction, crosscutting the whole sample. Dominant microstructures in the sample are deformation lamellae and pronounced undulatory extinction produced by crystal lattice distortion. Backscatter SEM images (Fig. 3.2a) and EMPA element distribution maps (Fig. 3.2b) show the presence of large (100 μm), newly formed rutile aggregates in the internal parts of the quartz crystal, together with small rutile inclusions along cracks formed during the experiments (Fig. 3.2b). EMPA measurements indicate Titanium contents below the detection limit throughout the entire quartz crystal, with the exception of the vicinity of the rutile inclusions along cracks and grain boundaries (due to analytical artifacts, see above).

3.4.3 Sample deformed at 900 °C and confining pressure of 1.5 GPa

Sample mn319 (O^+ orientation) was deformed for 99 h at 900 °C and confining pressure of 1.5 GPa, and then annealed at hydrostatic conditions for 76 h after deformation. The mechanical data show a peak strength of 330 MPa followed by pronounced weakening after a strain of ~25 % (Fig. 3.3).

The heterogeneously deformed sample shows localization of deformation into recrystallized bands oriented approximately 45° to the compression (σ_1) direction (Fig. 3.5a).

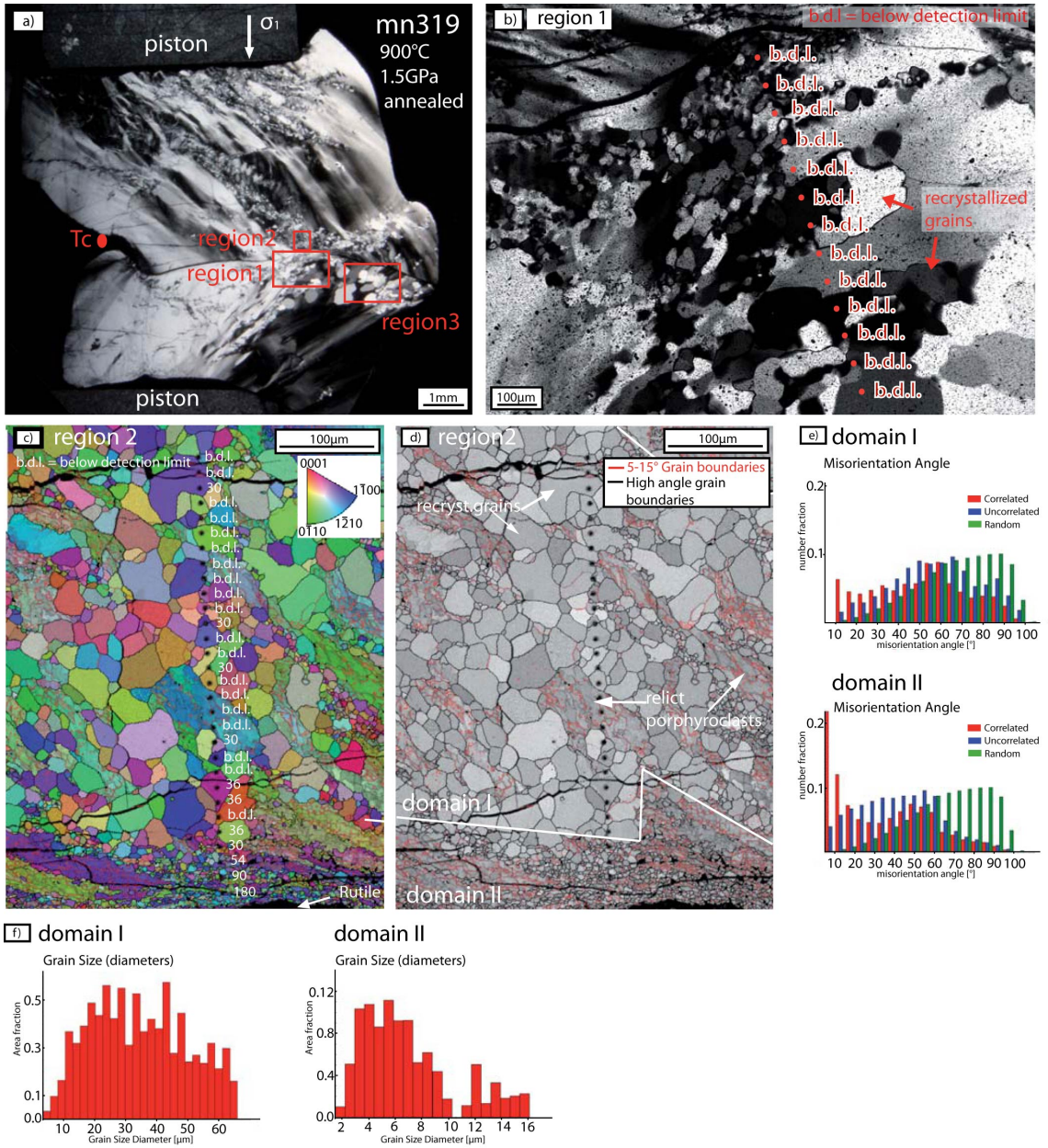

Fig. 3.5 Sample mn319 deformed at 900 °C, 1.5 GPa at a strain rate of $1x10^{-6}$ s^{-1}, in presence of TiO_2 powder and fluid (H_2O). Compression direction (σ_1) is vertical in all images. **(a)** Light micrograph (crossed polarizers) of sample mn319. Final position of the thermocouple (Tc) and position of the analyzed regions are marked in red. **(b)** Cross polarized light

micrograph of recrystallized region 1. Considering the temperature gradient in the sample, deformation occurred in this region at a temperature of 894 °C. Ti-contents measured by EPMA are marked in red (detection limit 20 ppm). The expected equilibrium Ti content is 121 ppm. **(c)** EBSD orientation image of region 2 (Ti-content in white numbers, expected Ti content: 127 ppm). Orientations according to the inverse pole figure given in the upper corner of the image. **(d)** Grain-boundary misorientation map of region 2 acquired with EBSD using nearest neighbor pairs. Misorientation angles <15° are represented in red, misorientation >15° are represented in black. Note the two distinct grain sizes of domain I and II. **(e)** Histogram of distribution of misorientation angles for domain I and II. Correlated (red bars), uncorrelated (blue bars) and random (green bars). **(f)** Grain size distribution (area fraction) of domain I and II of the recrystallized region 2.

The recrystallized bands are composed of coarse-grained domains (domain I) and fine-grained domains (domain II). The coarser-grained domains consist of grains with variable size ranging up to 65 μm (Fig. 3.5b,c,d,f), although locally grains can reach 500 μm (region 3, Figs. 3.5a, 3.6a).

The large recrystallized grains, which show no undulatory extinction, have irregular to polygonal shapes and smoothly curved grain boundaries where local pinning occurs (Fig. 3.6a). High angle grain boundaries separate the large recrystallized grains from neighboring, strongly elongated relict porphyroclasts (Fig. 3.5d). The relict porphyroclasts contain subgrains of considerably smaller size (~3-7 μm) defined by misorientation angles of 5-15° (Fig. 3.5d). The size of the subgrains is similar to the size of the recrystallized grains in domain II (Fig. 3.5c,d,f).

A narrow but distinct zone with smaller grains is present close to the boundary of the two sample pieces (domain II in Fig. 3.5c,d). In this zone the recrystallized grains show a mean grain size of ~5 μm (Fig. 3.5f). The histogram of the distribution of misorientation angles (correlated, red bars) (Fig. 3.5e) from domain II shows a high frequency of small misorientation angles. This indicates that progressive subgrain rotation is the likely recrystallization mechanism, consistent with the similar size of subgrains and recrystallized grains. The submaximum in misorientation angles at 50-60° may represent Dauphiné twin boundaries (Frondel 1962).

The bimodal grain size distribution of the whole sample is consistent with abnormal grain growth during annealing. Thus, during annealing the population of grains with sizes of 10-65 μm and curved, polygonal grain boundaries most likely grew from the originally dynamically recrystallized grains (~3-7 μm).

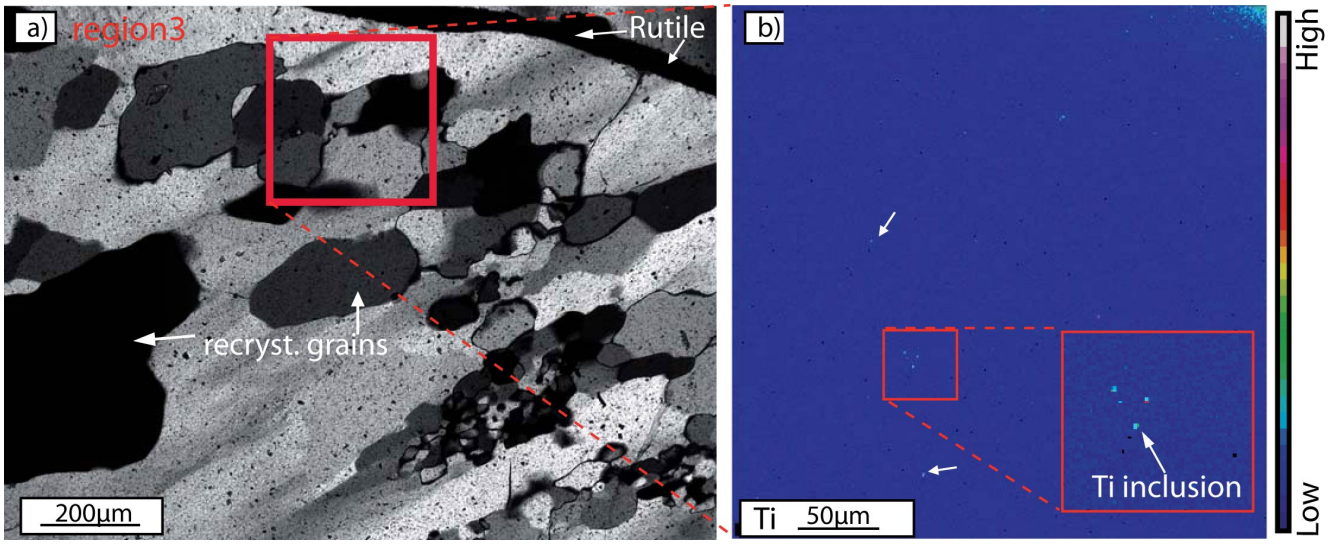

Fig. 3.6 Ti-distribution in the recrystallized region 3 of sample mn319. **(a)** Cross-polarized light micrograph of the recrystallized zone. Estimated deformation temperature: 890 °C. The red square indicates the position, where the element distribution map was acquired (see part b). Note the large (up to 300 μm) recrystallized grains with lobate grain boundaries and irregular grain shape typical for grain boundary migration recrystallization (GBM) induced by static recrystallization. **(b)** Element distribution map of the region with recrystallized grains and original undeformed single crystal. Arrows indicate small Ti inclusions distributed along grain boundaries and in grain triple junctions. The inset shows a detail of small Ti inclusions. The upper right corner of the map show a higher Ti content produced by analytical artifacts caused by the presence of rutile along the sample boundary.

EMPA measurements were performed in three different regions within the sample. Considering the temperature gradient in the sample (temperature decrease of around 10 % from center to the edges) the analyzed regions were deformed at temperatures of 894 °C (region 1 Fig. 3.5b), 900 °C (region 2, Fig. 3.5c), and 890 °C (region 3, Fig. 3.6). All EMPA analyses in region 1 and in domain I of region 2 show Ti concentrations below or close to the detection limit. The Ti values measured in the undeformed and recrystallized parts of this region are the same as the Ti concentration of the starting material (Figs. 3.5b, 3.6b). An EMPA element distribution map (Fig. 3.6) displays small rutile inclusions at grain boundaries (few µm in size). In the upper right corner of the map shown in Fig. 3.6 a local Ti enrichment of quartz is observed. This region is in close proximity to the sample edge, where primary rutile is present (see analytical artifacts in Methods section). In domain II of region 2, the increased Ti values in the fine grained recrystallized quartz grains are due to phantom Ti – otherwise all Ti-values are below the detection limit, except a few measurements at grain boundaries (Fig. 3.5c).

3.4.4 Samples deformed at 1000 °C and confining pressure of 1.5 GPa

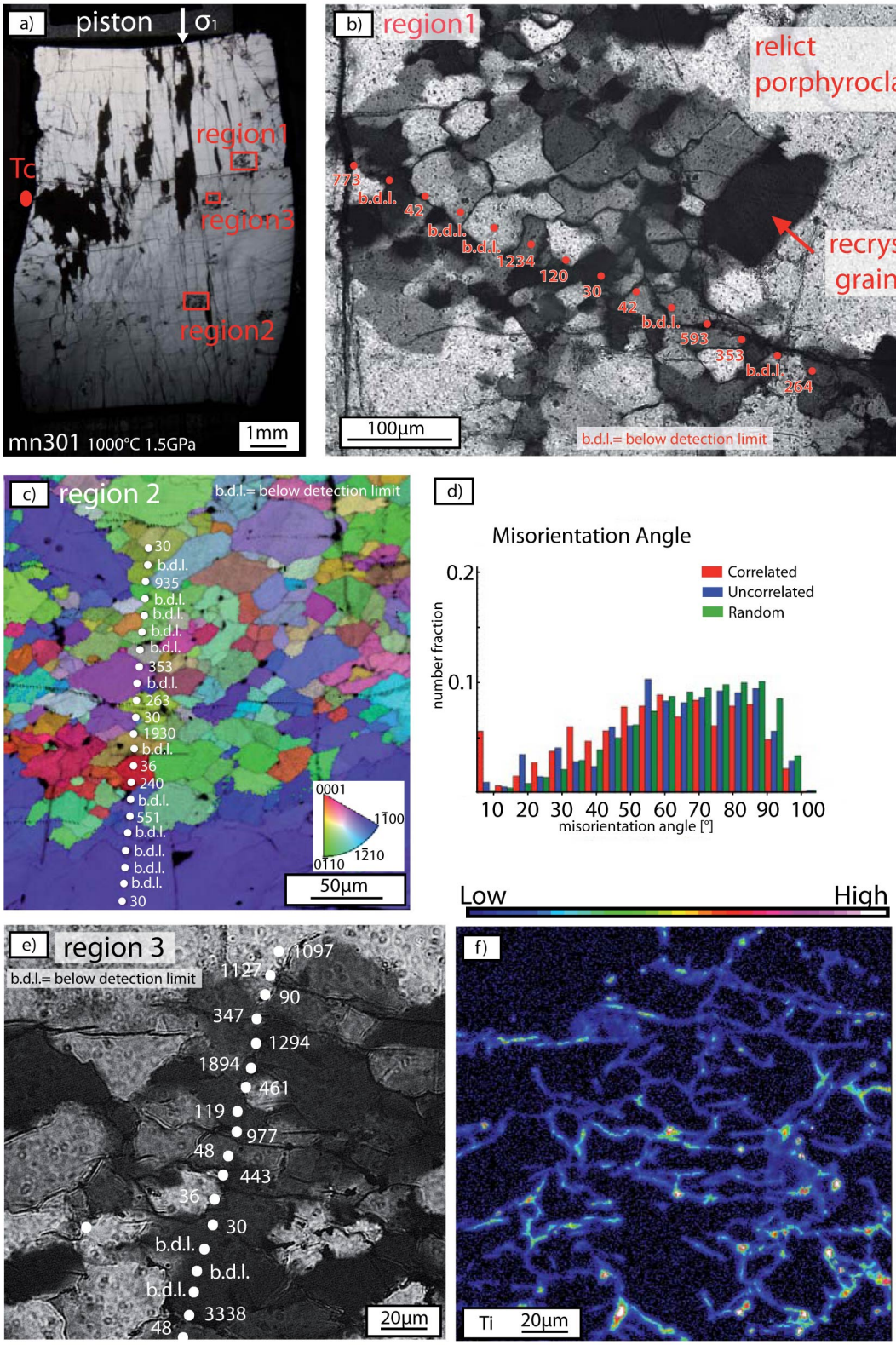

Fig. 3.7 Microstructures and chemical composition of sample mn301 deformed at 1000 °C, 1.5 GPa in the presence of TiO_2 powder and fluid (H_2O). Experimental shortening direction is vertical in all images. **(a)** Cross polarized light

micrograph of sample mn301. Final position of the thermocouple (Tc) and position of the analyzed regions are marked in red. Longitudinal cracks are visible as a consequence of hitting the sample at low confining pressure and temperature prior deformation. Horizontal cracks developed during quenching and unloading of the sample after deformation. Crystal-plastic deformation is localized in distributed pockets of recrystallized quartz grains (red boxes). **(b)** Light micrograph (cross polarized) image of a recrystallized pocket (region 1), local temperature 981°C. In red are marked the Ti [ppm] content measured by EMPA. Expected equilibrium content at these conditions is 226 ppm Ti. Note the large variation of Ti content in the zone: the central parts of the recrystallized grains show uniformly low contents (below detection limit to 42 ppm) whereas grain boundaries can show extremely high Ti contents (264-1234 ppm). **(c)** EBSD Orientation map of region 2. The crystallographic orientations in the map are color-coded according to the inverse pole figure given in the lower corner of the image. Indicated in white are the Ti contents (ppm) measured with the microprobe (detection limit 20 ppm). Grain boundaries and grains triple junctions show high Ti contents, whereas the central parts of the recrystallized grains and the undeformed quartz (lower part, in blue) show Ti contents much lower than the expected equilibrium value of 186 ppm. **(d)** Frequency distribution of misorientation angle between nearest neighbor pixels (correlated, red bars) and for any pairs in the data set (uncorrelated, blue bars). For reference, the distribution of a data set with random orientation (green bars) is given. **(e)** Light micrograph of recrystallized region 3 with measured Ti contents (in ppm). **(f)** Element distribution map acquired by EPMA. Rutile grains (red to light blue color) are present along grain boundaries and triple junctions, indicating mobility of TiO2 during the experiment

Samples deformed at a temperature of 1000 °C and 1.5 GPa confining pressure exhibit variable mechanical behavior (Fig. 3.3a,b). Peak strength varies from 90 MPa in sample mn326 to 300 MPa in sample mn332. Samples mn301 and mn332 show some weakening after reaching peak strength, whereas sample mn326 achieved steady state flow (80 MPa) at relatively low strains (Fig. 3.3a). Sample mn331, which was deformed up to peak strength at a strain rate of $1x10^{-6}$ s^{-1} and then at a strain rate of $1x10^{-7}$ s^{-1}, shows peak strength of 180 MPa.

Sample mn301, deformed in the O^{+} orientation (Fig. 3.7), was deliberately pre-cracked during the loading process and subsequently deformed to a strain of 28 %. This sample does not show extensive recrystallization. The initial cracking at low confining pressure produced longitudinal fractures oriented parallel to the compression direction (Fig. 3.7a). Subsequent crystal plastic deformation has produced bulges of the sample, together with isolated patches of recrystallized quartz aggregates (Fig. 3.7a,b,c). The patches are connected with the initial cracks and consist of grains of variable size (10 µm - 100 µm), with irregular shapes and lobate grain-boundaries. The frequency distribution of misorientation angles (Fig. 3.7d) for neighbors (red bars) and uncorrelated grains (blue bars) shows a more random distribution compared to lower temperature experiments. The frequency of misorientation angles <15° is lower than in experiments at 800 °C and 900 °C, except for the very low misorientation angles (<5°).

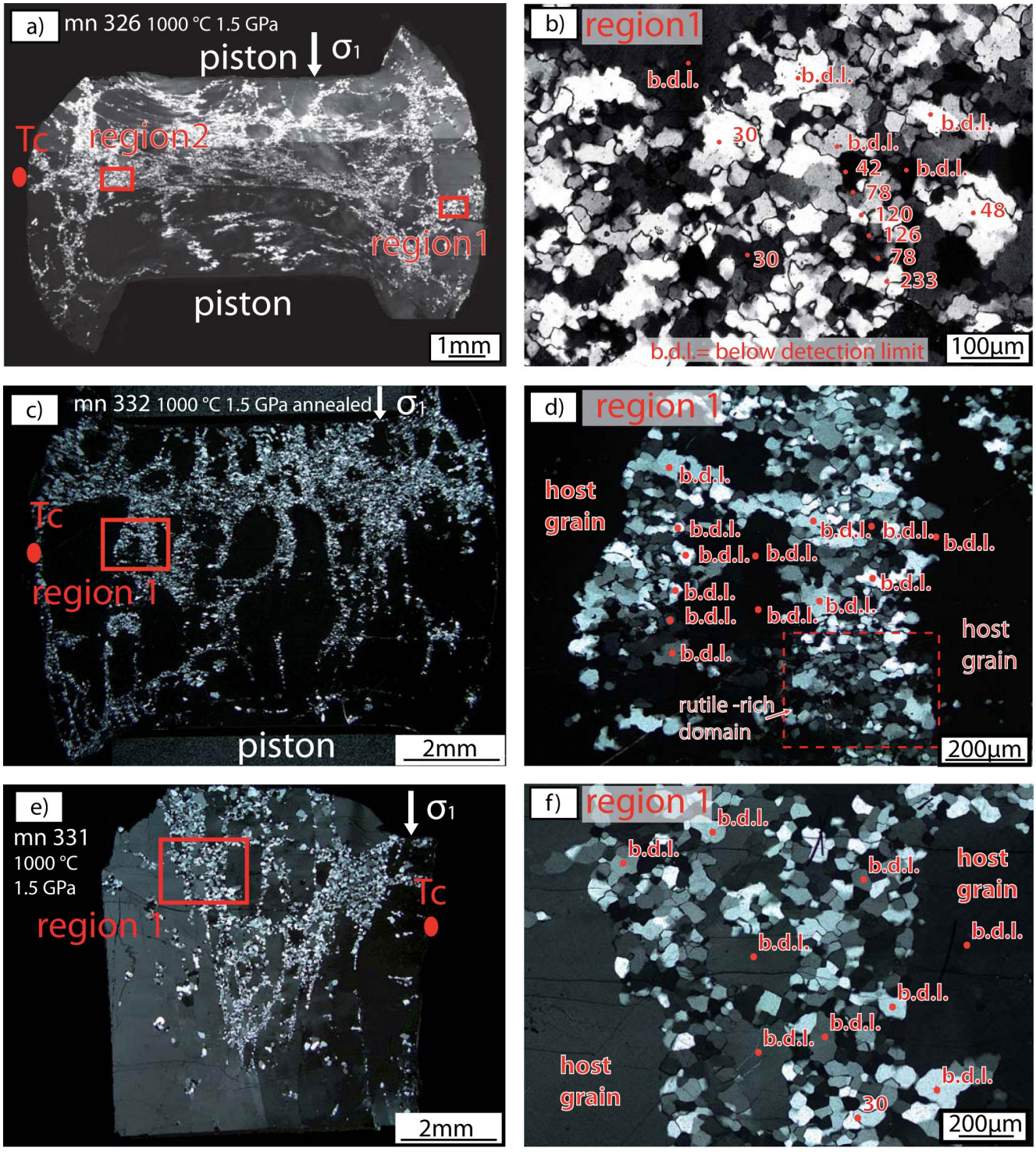

Fig. 3.8 Recrystallized microstructures and chemical composition of a quartz single crystals deformed with the addition of TiO_2 powder and fluid (H_2O) at 1000 °C, 1.5 GPa. All images are cross polarized light micrographs. Compression direction is vertical in all images. Final position of the thermocouple (Tc) and position of the analyzed regions are marked in red. **(a)** and **(b)** sample mn326 deformed at a strain rate of 10^{-6} s^{-1} for 93 hours. **(c)** and **(d)** sample mn332 deformed at a strain rate of 10^{-6} s^{-1} for 120 hours and annealed afterwards for 139 h at the same conditions. **(e)** and **(f)** sample mn331 deformed at a strain rate of 10^{-7} s^{-1} for 244 h. All samples show the typical high temperature recrystallization microstructures. Note the strongly irregular grain shape, the variable grain size and the lobate grain-boundaries with local pinning structures typical for recrystallization by grain boundary migration (GBMR) in the samples

mn326 and mn332. Note the small grain size of the recrystallized quartz grains in the rutile-rich domain of sample mn332. Sample mn331 shows variable grain size and quite straight grain boundaries. The Ti contents in ppm, marked in red, show the same trend as in sample mn301 with high Ti content at grain boundaries and low contents in the central part of the recrystallized grains.

The chemical composition of three recrystallized patches in sample mn301 was analyzed by microprobe. Considering the relative position of the patches with respect to the final position of the thermocouple and the temperature gradient in the sample, a deformation temperature of 981 °C was calculated for region 1 (Fig. 3.7b), 953 °C for region 2 (Fig. 3.7c) and 1000 °C for region 3 (Fig. 3.7e). EMPA analyses show strong variations in the Ti content for all three patches, ranging from values below the detection limit to 3338 ppm (Fig. 3.7b,c,e). High Ti contents are always measured close to grain triple junctions, along grain boundaries, or along cracks (Fig. 3.7b,c,). The element distribution map acquired in region 3 (Fig. 3.7f) shows high Ti-values in discrete points, triple junctions of quartz grains, along cracks and in very narrow lines, all of which coincide with grain boundaries (Fig. 3.7e,f). Thus, Ti-contents above the detection limit are only recorded from areas related to newly formed rutile precipitates on triple junctions and grain boundaries of quartz, whereas the internal parts of grains show Ti contents uniformly below or close to the detection limit of the instrument.

The microstructures of all three samples of ⊥m orientation are quite similar to each other (Fig. 3.8).

Sample mn326 (Fig. 3.8a,b), which was deformed in direction normal {m} up to a strain of 40 %, shows extensive recrystallized bands surrounding relicts of more weakly deformed host quartz (Fig. 3.8a). The quartz relicts display undulatory extinction, a high density of low angle misorientations, and incipient subgrain formation at their boundaries (red in Fig. 3.9a). The subgrains have an estimated mean size of ~10 -25 µm. The recrystallized bands consist of grains with irregular grain shapes and with a grain size varying from ~5 to 65 µm (mean size of ~25 µm; Figs. 3.8b,3.9c). Locally some single grains can reach diameters of up to 150 µm (Fig 3.8b). Grains have lobate boundaries and pinning structures are also present (Fig. 3.8b). Some recrystallized grains show internal deformation and subgrain boundaries (marked in red in Fig. 3.9a). The misorientation angle distribution (Fig. 3.9b) shows an elevated frequency of low angle misorientations <15°, but these are less frequent than in lower temperature samples. On the other hand, high misorientation angles (50-90°) are much more frequent than in samples deformed at lower temperatures but less frequent than random (Fig. 3.9b).

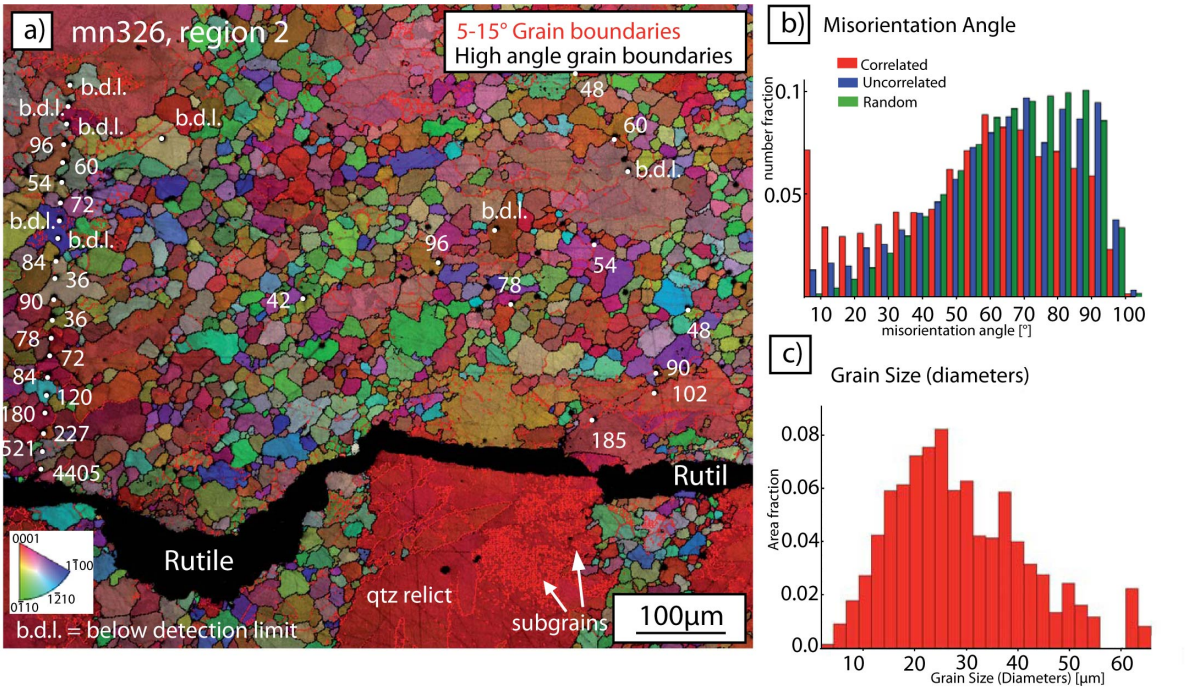

Fig. 3.9. EBSD results of sample mn326 deformed at 1000 °C, 1.5 GPa. **(a)** EBSD Orientation map of region 2. The crystallographic orientations are color-coded according to the inverse pole figure given in the lower corner of the image. Black lines represent grain-boundaries with misorientation angles >15°, red lines misorientation angles <15°. Ti contents (ppm) are marked by white numbers. Note the high Ti contents close to the rutile (in crack) caused by phantom Ti in Quartz. Small (~10 -25 μm) subgrains are visible within and at the boundaries of quartz relicts. **(b)** Frequency distribution of misorientation angles between nearest neighbor pixels (correlated, red bars, uncorrelated pairs, blue bars, random orientation, green bars). **(c)** Grain size distribution (area fraction) of recrystallized region 2. The grain size of the recrystallized grains varies from a few μm up to 65 μm, but the mean grain size is on the order of 20-25 μm.

EMPA analysis on two recrystallized regions deformed at 978 °C (region 1, Fig. 3.8b) and 1000 °C (region 2, Fig. 3.9b) shows in both cases a strong variation in the Ti content: a majority of the spot analyses result in Ti contents close to the detection limit of the microprobe (20 ppm), whereas a few analyses show values of several hundred ppm Ti (Fig. 3.8b). Ti contents below and close to the detection limit are measured in the internal parts of the recrystallized grains, whereas high Ti contents (78-233 ppm) are found at grain boundaries and grain triple junctions (Fig. 3.8b).

Sample mn332 (Fig. 3.8c,d) was deformed in direction normal {m} for 120 h and then annealed at hydrostatic conditions (1000 °C and 1.5 GPa) for 139 h. Even though recrystallization is distributed throughout the sample, deformation is not uniformly accommodated: recrystallization occurs in discrete bands that have an orientation approximately parallel to the loading direction (σ_1). Many bands appear in a crack-like distribution, especially in the lower, less recrystallized, part of the sample (Fig. 3.8c). Between the recrystallized bands, lesser deformed relict crystal material is

present (Fig. 3.8c,d). The recrystallized quartz shows variable grain size: the grains in the relatively rutile-free areas are up to 150 μm in width, whereas those within rutile-rich areas are smaller (15 μm) (Fig. 3.8d). Where rutile needles are present at the grain boundaries, the grains show evidence of pinning structures (Fig. 3.8b,d). EMPA measurements on sample mn332 were carefully taken only in the central parts of recrystallized grains; all values are below the detection limit of the instrument (Fig. 3.8d).

Sample mn331 (Fig. 3.8e,f) in ⊥ {m} orientation was first deformed with a strain rate of 10^{-6} s^{-1} up to peak strength and afterwards was deformed for 244 h with a strain rate of 10^{-7} s^{-1}. In the heterogeneously deformed sample strain was accommodated principally in the central part of the sample (the upper part was lost during sample preparation; Fig. 3.8e), whereas the lower and edge regions display only weak deformation characterized by undulose and patchy extinction. The crack-like distribution of the recrystallized bands is even more pronounced than in sample mn332, especially in the lower part of the sample (Fig. 3.8e). The recrystallized quartz bands often consist of diamond-shaped grains with sizes varying from 15 to 180 μm (Fig. 3.8e) and with weakly lobate grain boundaries (Fig. 3.8f). EMPA analyses of the internal parts of newly recrystallized grains reveal Ti contents below the detection limit of the instrument (Fig. 3.8f). Further, no Ti variation was observed between undeformed host quartz grains and recrystallized new grains (Fig. 3.8f).

In samples deformed at 1000 °C, there appears to be a succession of progressively evolving microstructures from low strain samples, in which recrystallized bands have a crack-like distribution (Fig. 3.8e; sample mn331), to high strain samples, in which the recrystallized bands accommodate most of the bulk strain (Fig. 3.8a; sample mn326). In all samples, however, the recrystallized grain shapes are similar (Fig. 3.8).

3.5 Discussion

3.5.1 Mechanical data

Strength differences between 0^+ and ⊥m orientations at 900 and 1000 °C (Fig. 3.3) are not systematic and most likely do to strain partitioning, which is a general feature of many single crystal experiments. Localization of recrystallization is common and leads to strain partitioning.

The experiments on natural “wet” single crystals carried out in this study under controlled crystal orientation, P, T, and strain rate conditions only show approximately reproducible mechanical

behavior (Fig. 3.3). The direct comparison of single crystals versus polycrystalline material experiments is difficult, because in single crystals, the onset of recrystallization requires higher strain, and strain partitioning is more pronounced. However, a qualitative comparison of the mechanical behavior of the two different materials is possible.

In our series of experiments, samples deformed at 800 and 900 °C show high peak strengths followed by pronounced weakening, whereas at 1000 °C samples deform by more steady state flow at lower stresses (flow stresses of ~80-250 MPa; Fig. 3.3). In the experiments of Hirth and Tullis (1992) the same pronounced weakening after peak strength is observed in polycrystalline Heavitree quartzite deformed in "regime 1", where the recrystallization takes place by bulging recrystallization, but at lower temperatures (700 °C). In our experiments, the recrystallization mechanism is somewhat different for the same type of mechanical behavior (see section below).

Hirth and Tullis (1992) observed steady state flow in samples deformed at 800 °C and higher (regime 2 and 3), where deformation was accompanied by rotation recrystallization (progressive subgrain rotation, SGR) and grain boundary migration recrystallization (GBM). Comparison of our mechanical data with those of Hirth and Tullis (1992, for as-is samples) indicates that our experiments show generally similar mechanical behavior, but at flow stresses, which are 100 to 300 MPa higher at the same temperatures and strain rates. The data by Stipp et al. (2006), who performed water-added experiments as in our case, show 50 MPa lower flow stress in 1000 °C experiments, 40 to 140 MPa lower in 900 °C experiments, and 230 MPa lower in 800 °C experiments at similar strain rates as in our experiments (comparing end-strengths at the highest volume of recrystallized grains in our samples).

The differences in flow stress between polycrystalline and single crystal experiments most likely arise from the inhomogeneous distribution of strain within the single crystal samples. The strain partitioning coincides with the location of regions of recrystallization (e.g., Figs. 3.4,3.5,3.8) and the distribution and content of H_2O (in the form of fluid inclusions). Although we carefully chose homogeneous milky regions of the quartz single crystal, the local distribution of fluid inclusions varies within a sample and causes strain partitioning. Nevertheless, the experiments show a general trend of decreasing flow stress with increasing temperature, and, together with the dynamic recrystallization microstructures, indicate the activation of dislocation creep deformation.

3.5.2 Microstructures

The recrystallization mechanisms are expected to be very important for the exchange of Ti in quartz (Grujic et al. 2011; Härtel and Herweg submitted). Therefore, one of the main tasks of this study was to test the potential effect of different recrystallization mechanisms on Ti-exchange. Below, the recrystallization mechanisms in the experimens are first discussed and then related to the measured Ti-content of the new quartz grains.

Dynamic recrystallization commonly occurs by the transformation and/or movement of grain boundaries through the crystal. In polycrystalline rocks grain boundaries are already present in the starting material, whereas in single crystals they first need to be formed. As demonstrated by (Vernooij et al. 2006a,b), the initial stage of recrystallization in a quartz single crystal may occur by the formation of micro-fractures. Along those microcracks small fragments and local crystal misorientations are formed. With increasing strain, these fragments and the small misoriented crystal domains grow and form recrystallized grains that undergo crystal plastic deformation. The same features have been observed by Stünitz et al. (2003) in feldspar single crystals.

In our lower strain samples, initiation and localization of deformation in longitudinal narrow bands oriented parallel to the σ_1 direction is evident (fig. 3.8e). With increasing strain (fig. 3.8a,c) the recrystallized bands widen and become locally displaced. The specific dynamic recrystallization mechanism operating in the bands is temperature, strain rate, water content, and grain size dependent (e.g., Hirth and Tullis 1992; Stipp et al. 2002a,b; Stipp et al. 2006, 2010). As the experiments reported here were performed over a relatively wide range of pressure and temperature conditions, different recrystallization mechanisms are activated during deformation.

The sample (mn277) deformed at 800 °C and 1.0 GPa shows crystal lattice distortion in low strain domains leading to the formation of deformation lamellae and bands of undulatory extinction (Fig. 3.4). In high strain domains the microstructure is characterized by core and mantle structures, consisting of elongated porphyroclasts surrounded by small recrystallized grains, commonly with slightly different crystallographic orientations. The grain size of the subgrains within the porphyroclasts is relatively homogenous (varying from 6 -12 μm) and similar to those of the newly recrystallized grains. The progressive development of subgrains and new grains by rotation recrystallization in sample mn277 is well documented by the grain-boundary misorientation map and the high frequency of low angle misorientations (Fig. 3.4). Based on these microstructural

observations, it is inferred that sample mn277 recrystallized predominantly by subgrain rotation recrystallization (SGR, e.g., Guillope and Poirier 1979; Urai et al. 1986; Wheeler et al. 2001; White 1967).

Sample mn319, deformed at 900° and subsequently annealed hydrostatically after deformation for 76 h, shows two distinct microstructural domains (Fig. 3.5). Domain II is a fine grained, strongly sheared band and extensively recrystallized in the center of the sample (Fig. 3.5c,d). Elongated porphyroclasts with undulatory extinction, formation of subgrains of 3 to 7 μm in size (concentrated principally at the boundaries of porphyroclasts), similar size of subgrains and recrystallized grains, and the high frequency of low misorientation grains indicates rotation recrystallization (SGR). Domain I consists of larger grains up to 500 μm in diameter. The irregular shapes and lobate and partly straight grain boundaries with local pinning structures are evidence for migration of grain boundaries (e.g., Gottstein and Mecking 1985; Jessell 1987; Urai et al. 1986). It is most likely that a large part of the grain boundary migration occurred during the annealing stage of the experiment, but some of the migration may have started during deformation at lower strain rates in these domains when deformation partitioned into other parts of the sample.

At 1000 °C, recrystallization of the quartz single crystal occurs by a combination of subgrain rotation recrystallization and grain-boundary migration. The samples show relatively small subgrains developed within and at the margins of porphyroclasts, surrounded by domains of much coarser recrystallized grains with lobate boundaries (Fig. 3.7-3.9). Evidence for grain boundary migration is the relatively low frequency of low misorientation angles, caused by the elimination of high-energy interfaces (Wheeler et al. 2001). In samples mn301, mn326 and mn331 the grain-boundary migration microstructures represent dynamic recrystallization, because these samples were quenched immediately after deformation.

The equilibrium grain size of dynamically recrystallized rock (during steady state flow) is dependent on the applied stress (e.g., Derby 1991). Considering the stable flow stress of c. 80 MPa reached by sample mn326, the equilibrium recrystallized grain size predicted by the quartz piezometer of Stipp and Tullis (2003) at our experimental conditions would be ~15μm. The size of the subgrains observed within and around the porphyroclasts in the central part of the sample is ~10-25 μm (Fig. 3.9), corresponding to a flow stress of 30 to 80 MPa (Stipp and Tullis 2003), and suggesting that the original size of newly recrystallized grains in this sample was similar to that predicted by the quartz piezometer. However, large recrystallized grains with diameters up to 150

μm are present in the peripheral regions of the sample. As discussed above (for the recrystallization bands), with increasing strain partitioning parts of the sample may cease to deform (e.g., close to the alumina pistons). In this situation grain growth is favored over dynamic recrystallization. The local abnormal grain growth in sample mn326 is interpreted as a result of annealing of parts of the samples during strain partitioning.

According to Stipp et al. (2010), the highest temperature/lowest strain rate conditions attainable in deformation experiments yield microstructures in a transition region between GBM and SGR mechanisms (between regime 2 and 3). In our samples, however, there is ample evidence for dominant boundary migration microstructures (i.e. regime 3). We suggest that the most important reason for this difference is the strain partitioning and partial annealing discussed above.

3.5.3 Relationship between deformation mechanisms and Ti re-equilibration in quartz

The amount of Ti that can be incorporated into a quartz crystal depends on temperature (Ostapenko et al. 2007; Wark and Watson 2006), pressure (Ostapenko et al. 2007; Thomas et al. 2010), and the growth rate of the crystals (Huang and Audétat 2012). Based on the data of Thomas et al. (2010) and the fact that TitaniQ can be applied to deformed and metamorphic rocks as suggested by Kohn and Northrup (2009), we would expect recrystallized grains in our deformed quartz samples to have Ti values ranging from 117 to 256 ppm (see table 3.3). However, the recrystallized grains of the deformed samples show much lower Ti contents, mostly below the detection limit (20 ppm) of the electron microprobe.

In samples deformed at 800 °C, EPMA analysis on the undeformed regions, along bands of undulatory extinction, and in zones with core and mantle structures, shows no Ti exchange. All measurements of Ti were below the detection limit (20 ppm) of the instrument. Also in the experiments at 900 °C the Ti values were uniformly low across the whole sample. Element distribution maps and point analyses reveal no Ti enrichment in the small, recrystallized grains or in large grains, which underwent grain growth.

Sample	Exp. T [°C]	Region	T [°C] deviation	Calculated T [°C]	Expected Ti [ppm]	Measured Ti [ppm](repr. value)
mn277	800	2	0	800	147	b.d.l.
mn319	900	1	- 6	894	121	b.d.l.
		2	0	900	127	b.d.l.
mn301	1000	1	- 19	981	226	b.d.l.
		2	- 47	953	186	b.d.l.
		3	0	1000	256	b.d.l.
mn326	1000	1	- 22	978	222	30
		2	0	1000	256	36
mn331	1000	1	0	1000	256	b.d.l.
mn332	1000	1	0	1000	256	b.d.l.

Table 3.3. Calculated and measured Ti contents in the deformed quartz single crystal. Calculation of the expected equilibrium Ti content in the analyzed zones, considering the temperature deviation caused by the temperature gradient (= temperature decrease of around 10 % from the center of the sample to its end). Expected Ti contents were calculated as: $RT \ln X^{quartz}_{TiO2} = -60952 + 1.520 * T(K) - 1741 * p(kbar) + RT \ln a_{TiO2}$ (Thomas 2010), where a_{TiO2} was 1 since rutile is present in all samples, R= 8.3145 J/K (gas constant), T is temperature in °K and p is confining pressure in kbar. The conversion from TiO_2 to Ti [ppm] occurred according to the formula of Thomas (2010). The representative value for the measured contents was calculated as the average of the measurements, which were taken at a minimal distance of 100 µm from the rutile inclusions, in order to avoid errors caused by phantom Ti in quartz. Note that all the representative values are close or below the detection limit (b.d.l.) of the instrument.

In experiments performed at 1000 °C very high Ti values locally alternate with values below the detection limit. Element distribution maps indicates no titanium re-equilibration in the internal parts of the recrystallized grains and high Ti contents along grain boundaries, caused by the presence of small rutile needles which crystallized in dilatant sites or by small rutile inclusions distributed along the grain boundaries. The presence of precipitated Ti-phases along grain-boundaries generates secondary analytical artifacts, leading to apparently high Ti contents in the border regions of adjacent quartz grains. However, point analyses of grains deformed at 1000 °C indicate uniformly low Ti contents (below the detection limit) in the interior parts of the recrystallized grains. We conclude that the Si—Ti substitution in quartz, the basis for the TitaniQ geothermobarometer (Ostapenko et al. 2007; Wark and Watson 2006), does not occur in our experimentally deformed quartz single crystals under the deformation conditions investigated here.

Possible factors that may inhibit Ti re-equilibration during these experiments are:

(1) No Ti was available at the sites of exchange due to limited mobility of Ti during the experiments. (2) The kinetics of the exchange processes are too slow in the experiments (for example a slow growth rate of recrystallizing grains). (3) The recrystallization mechanisms do not allow ionic exchange during the experiments. (4) The activation energy for the atomic substitution is too high in the solid state and complete reconstitution by solution precipitation has not been achieved in the experiments. Below, we discuss each of these possibilities individually;

1) 0.2 g of fine-grained TiO_2 powder was placed around the quartz single crystal or between individual pieces of single crystals in a welded jacket prior to deformation. After deformation we observed large aggregates of euhedral rutile inside deformed quartz grains. Rutile precipitates occur on grain boundaries of recrystallized quartz grains and along cracks (Fig. 3.2). The nucleation and growth of rutile in these sites indicates that Ti was available at the locations of recrystallization and that essentially all new quartz grains recrystallized under rutile saturated conditions. Ti was most likely transported in the sample through fluids during the deformation process. Due to the presence of rutile in all samples we assume a TiO_2 activity of $= 1$ (see also Thomas et al. 2010).

2) The kinetics and growth rate of crystals have an influence on the amount of trace elements that can be incorporated in the crystal. Huang and Audétat (2011) propose an increase in titanium concentration with increasing growth rate of newly formed quartz. This arises from the fact that trace element incorporation is aided by imperfect crystal growth, which is more likely to occur in crystals that are relatively fast grown (e.g., Martin and Armington 1983) and/or by the fact that in fast-grown crystals diffusional reorganization of the crystal lattice is limited (Watson 2004; Watson and Liang 1995).

In domain II of sample mn319 the newly recrystallized grains formed by subgrain rotation have a size of 2-10 µm (Fig. 3.5). During deformation and annealing the quartz grains grew up to 500 µm due to the mobility of some grain boundaries (abnormal grain growth). At a run time of 5 days (time calculated after reaching peak strength, which should coincide with the onset of recrystallization, Hirth and Tullis 1992) and considering an initial grain size of 2-10 µm and a concentric growth of the grains, this translates to a growth rate varying from <1 to 50 µm/day (table 3.4). A growth rate difference of around 50 µm/day led in the experiments of Huang and Audétat (2012) to Ti variations of around 80 ppm. However, in our experiments large grains and small grains (which grew at different growth rates) show no systematic difference in Ti content and in both cases the Ti values

are much lower than expected. We conclude that the growth rates of the new grains formed by recrystallization and the growth rate variation are not responsible for the lack of Ti exchange in the deformed samples.

Sample	T [°C] experiment		Grain size (diameter) [μm]	Time after peak strength [days]	Growth rate [μm/day]
mn319	900	Region 2	6 - 100	5	<1 - 10
		Region 3	30 - 500	5	3 - 50
mn301	1000	Region 1	10 - 150	3	1 - 25
		Region 2	10 - 80	3	1 - 13
mn326	1000	Region 1	10 - 150	4	1 - 19
		Region 2	10 - 65	4	1 - 8
mn331	1000	Region 1	15 - 180	10	<1 - 9
mn332	1000	Region 1	15 - 150	10	<1 - 7

Table 3.4. Grain size and growth rate of the recrystallized quartz grains. The grain size (diameter) is defined by the major diameter of an ellipse having the same area as the grains. Growth rate [µm/day] calculated as grain size (radius) divided by the experimental time after reaching peak strength (onset of recrystallization)

3) At temperatures of 800 and 900°C in our experiments, deformation occurred mainly by subgrain rotation recrystallization (SGR). During SGR, new grains develop by progressive misorientation of the crystal lattice, but the new grains inherit the internal structure and defects of the old grains. During this process, new grain boundaries form by volume diffusion processes inside the old quartz grains without interacting with a fluid. In this case, no re-equilibration of Ti is expected, which is in agreement with our measurements and observations.

At higher temperatures (1000°C), recrystallization of quartz occurred by a combination of subgrain rotation recrystallization and grain-boundary migration (i.e. local displacement of the grain boundaries; Gottstein and Mecking 1985; Urai et al. 1986). The migration of grain boundaries (regardless of whether this occurs by grain boundary migration recrystallization or by grain growth) involves the transfer of material across the boundary and normally requires elevated temperatures and/or the presence of a diffusion-enhancing fluid film along the boundary (Drury and Urai 1990). In

this case, ionic exchange is expected. Chemical changes in the solid material produced by migration of boundaries and related ionic exchange have been documented in experiments conducted on carbonate bicrystals by Evans et al. (1986) and Hay and Evans (1987a,b).

In our experiments, both GBM and grain growth occurred by boundaries migrating across Ti-saturated zones (fluid film). Therefore, ionic exchange between the recrystallized quartz grains and the Ti-saturated fluid was expected. However there was incomplete or no Ti-exchange in the grains deformed by grain boundary migration. We conclude that titanium was not incorporated (or only at levels below the equilibrium concentration) into the crystal structure despite extensive structure reconstitution during recrystallization by boundary migration and grain growth, and ideal conditions for ionic exchange (high temperatures, presence of Ti-saturated fluid, mobility of grain boundaries)

(4) Atomic substitution of Si by Ti is demonstrated in the studies of Wark and Watson (2006), Thomas et al. (2010), Huang and Audetat (2012) where the synthetic quartz crystals were crystallized and rapidly grown from amorphous SiO_2 in rutile-bearing H_2O fluid. Likewise, during crystallization from a melt, substituting elements are likely to be incorporated into the quartz structure as observed by Rankama and Sahama (1950) and Jacamon and Larsen (2009). Once the quartz crystals have formed, Si has to be exchanged for Ti to adjust the composition to the new equilibrium composition, e.g., at changing P,T conditions.

As predicted by Ostapenko et al. (2007) and Wark and Watson (2006) the incorporation of Ti into quartz occurs by a simple substitution, where a tetravalent Ti atom is substituted with a tetravalent Si atom. Atomic substitutions in crystalline materials occur when the valences of substituting ions are similar (difference not greater than = 1) and when the substituting ions have a similar size (size difference <15%). The ionic radius of Si^{4+} (0.40 Å) is almost 40 % smaller than that of Ti^{4+} (0.61 Å) (Perkins 2002). Furthermore, the Si—O bond is a very strong covalent bond (Flem et al. 2002), so that the energy required for the solid state substitution of Si by Ti is high. Therefore, it is conceivable that substitution of Si by Ti takes place by complete dissolution of the quartz and precipitation from a fluid-rich aqueous environment, where Ti-transport is very fast. Larsen et al. (2004) also observed the immobility of Ti during recrystallization of igneous quartz.

Incorporation of Ti atoms into the quartz lattice during dynamic recrystallization could be insufficient because of sluggish Ti-transport and because of incomplete reconstitution processes of the quartz crystal structure during grain boundary migration. Hay and Evans (1987a,b) and Evans et al. (1986) observed progressive chemical changes behind repeated oscillatory grain boundary

movement in carbonates. Thus, it may be necessary to move grain boundaries repeatedly through a crystal structure to achieve an equilibrium composition by ionic exchange. Some of the more elevated Ti-contents of recrystallized grains in our experiments may indicate limited Ti-exchange (Figs. 3.7,3.9), but the values are much lower than the expected equilibrium contents. The total strain for strain induced grain boundary migration and time required to reach equilibrium contents may well exceed the conditions of our experiments.

3.5.4 Applicability of the TitaniQ geothermometer to deformed rocks

Kohn and Northrup (2009) suggested that TitaniQ accurately measures dynamic recrystallization temperatures and therefore can be applied to quartz-bearing mylonites. However, our experiments demonstrate that Ti is not incorporated into the crystal structure during recrystallization, even in a fluid-bearing and Ti-saturated environment at the investigated deformation conditions (T = 800-1000 °C, P = 1-1.5 GPa, strain rates 10^{-6} -10^{-7} s^{-1}, total strains of up to 47%), regardless of the specific recrystallization mechanism. This raises questions as to the applicability of the TitaniQ geothermobarometer to prograde metamorphic rocks which experienced deformation and recrystallization.

On the other hand, during retrograde deformation, the decrease of temperature and/or pressure should lead to the removal, by exsolution or diffusion, of the Ti-atoms from the quartz structure. The removal process is energetically and kinetically favored over the incorporation process due to the fact that the Ti-atoms in the quartz crystal structure act as a defect (larger grain size, see above). The removal of Ti from the crystal lattice causes precipitation and accumulation of Ti-phases along the grain boundaries. As shown here, measurements on fine-grained recrystallized regions where rutile is present at grain boundaries can lead to erroneous results due to analytical artifacts caused by phantom Ti (EMPA measurements) or poor spatial resolution (large spot size of SIMS, LA-ICPMS). The problem of measuring the real Ti content in fine grained aggregates could explain the conflicting results obtained by applying the TitaniQ to naturally deformed rocks (e.g., Grujic et al. 2011, Wilson et al. 2012). We conclude that the application of the TitaniQ geothermobarometer to deformed metamorphic rocks at low fluid-contents may not be as straightforward as previously thought and requires further research.

3.6 Conclusions

Our experiments demonstrate that in a fluid-present and Ti-saturated environment, the isomorphic Si—Ti substitution in quartz is not likely to occur during deformation, regardless of the recrystallization mechanism involved in the deformation process. In our experiments, neither quartz grains formed by subgrain rotation recrystallization nor those showing evident grain boundary migration features (lobate grain boundaries, pinning, grain growth) show re-equilibrated Ti-contents. Instead, the Ti-contents are similar to the original, undeformed quartz single crystal. Where Ti-contents are higher, they never reach equilibrium concentrations for the given temperature-pressure conditions. The TitaniQ geothermobarometer has been demonstrated to accurately determine P-T conditions of quartz crystallization from a melt or hydrothermal fluid (Barker et al. 2010; Rusk et al. 2008). However, Si-Ti-exchange appears to be inhibited, or take place by different mechanisms, in experimentally deformed quartz crystals. One major difference between the experiments reported here and those used to calibrate the TitaniQ geothermobarometer (deformation and hydrostatic piston cylinder experiments; Wark and Watson 2006; Hayden and Watson 2007; Thomas et al. 2010; Huang and Audetat 2012) is our use of considerably lower H_2O-contents. The lower H_2O-contents most likely correspond more to those in natural deformation settings. Due to the limited or inhibited exchange of Ti during dynamic recrystallization of quartz at low concentrations of H_2O, care should be taken when applying the TitaniQ geothermobarometer to deformed rocks under prograde metamorphic conditions. Si-Ti-exchange in quartz crystals and Ti-equilibration is more likely to occur during retrograde conditions in recrystallized quartz, because Ti has to be exsolved and/or removed by diffusion. The exchange mechanisms of exsolution under such conditions may be kinetically more favorable. It remains uncertain whether TitaniQ can be applied to determine the P-T conditions of migmatite in which partial melting occurs (e.g., Storm and Spears 2009; Spear and Wark 2009, Grujic et al. 2011; Menegon et al. 2011).

CHAPTER 4

Partial melting and compositional changes in perthitic K-feldspar during experimental deformation at high pressure and temperature

4.1 Abstract

To investigate the relationships between deformation, cracking and partial melting in the lower continental crust we performed axial compression and hydrostatic experiments on natural perthitic K-feldspar single crystals. The experiments were performed with a Griggs-type solid medium deformation apparatus at temperatures of 700 °C and 900 °C, confining pressures varying from 0.75-1.5 GPa, total strains ranging from 3 to 40 %, and at constant strain rate of ~ 10^{-6} s^{-1}. Samples were deformed "as is" and with added H_2O.

The samples deformed at 700 °C showed typical brittle behavior, including the formation of fractures and conjugate cracks, and peak stresses that increase with confining pressure. Deformation at 900 °C was also largely accommodated by shear fractures oriented at ~40-50° to σ_1. The mechanical data at 900 °C, however, show an inverse dependence of normal stress with confining pressure and peak stresses well below the Goetze criterion, indicating that along the fractures deformation was not dominantly friction controlled. Microstructural observations and Electron Micro Probe chemical analyses reveal the presence of melt pockets (less than 6 vol%) with inhomogeneous compositions along fractures and shear zones. Gouge fragments changed composition where they occur in association with melt domains.

In hydrostatic experiments performed under identical pressure and temperature conditions, no melt and no compositional changes were observed, demonstrating that melt kinetics were, at least in part, controlled by the cracking process during the experiments.

Our observations indicate that deformation of single K-feldspar crystals at high pressure and temperature is controlled by the simultaneous formation of micro-fractures and melt. The formation of wet melt is strongly accelerated and kinetically favored by cracking as demonstrated by the

absence of melting in the hydrostatic single crystal experiments. The melt along fractures accommodates deformation by viscous processes, but it does not dramatically weaken the samples because melt domains are not interconnected. The coalescence of the initial micro-fractures generates conjugate fracture systems in which fine-grained gouge fragments undergo chemical homogenization. The dominant deformation mechanism in the gouge is likely to be melt-enhanced diffusion creep, which may also assist the chemical homogenization process.

4.2 Introduction

The relationships between deformation and melting have attracted extensive interest because of their fundamental influence on crustal rheology. The presence of melt has a tremendous effect on the mechanics and rheology of rock, and therefore controls a range of both large and small-scale tectonic processes (e.g., Beaumont et al. 2001; Clark and Royden 2000; Davidson et al. 1994; King et al. 2010a; Royden et al. 2008). Similarly, deformation influences the melting process, both in terms of the grain scale distribution of melt in polycrystalline aggregates, and the segregation and extraction of melt in partially molten continental crust and mantle rocks (e.g., Brown 2007; Brown 1994; Bussod and Christie 1991; Collins.W.J and Sawyer 1996; Cooper 1990; Holtzman et al. 2003a; Holtzman et al. 2003b; Holtzman and Kohlstedt 2007; Kohlstedt et al. 2010; Kohlstedt and Zimmerman 1996; Marchildon and Brown 2002; Parsons et al. 2004; Sawyer 2001; Weinberg 1999; Zimmerman et al. 1999).

Since the late 1970s laboratory experiments have demonstrated a close relationship between rock strength and melt content (e.g., Arzi 1978; Mecklenburgh and Rutter 2003; Rutter and Neumann 1995; Scott and Kohlstedt 2006). Rosenberg and Handy (2005) report dramatic weakening (strength loss of about 80 %) at a melt fraction of 0.07, caused by the onset of melt interconnectivity. At that low melt fraction, however, the bulk stress was still supported by the solid framework. The breakdown of the solid framework occurs at a melt fraction between 0.1 and 0.3 which produces a second pronounced weakening (Arzi 1978; Molen and Paterson 1979; Wickham 1987).

The distribution of melt in a rock also has a great influence on rheological behavior (Cooper et al. 1989; Kohlstedt 1992). Melt films that are spread along grain boundaries provide high – diffusivity pathways that can drastically enhance creep rates (Hirth and Kohlstedt 1995a,b; Jin et al. 1994; Pharr and Ashby 1983), whereas melt confined to grain triple junctions may result in only moderate enhancements of the diffusion creep rate (Cooper and Kohlstedt 1984; Dimanov et al.

1998). In addition, melt may influence the main deformation mechanisms of the rock. Experimental deformation of partially molten granitic aggregates suggests a switch from dislocation creep to predominantly melt-enhanced diffusion creep with increasing melt fraction (Dell'Angelo et al. 1987; Dell'Angelo and Tullis 1988).

Field observations indicate that localization of deformation into melt-weakened zones in the continental crust plays an important role in the formation of orogens and mountain belts (Beaumont et al. 2001; Davidson et al. 1994; Lexa et al. 2011; Schulmann et al. 2008; Slagstad 2005)
The spatial distribution of melt in a rock and the segregation and migration of melt in partially molten crust are dependent on the applied forces and on the regional stress field (Brown 2010, 2007, 1994; Daines and Kohlstedt 1997; Davidson et al. 1994; King et al. 2010; Kohlstedt and Holtzman 2009; Kohlstedt and Zimmerman 1996; Rosenberg and Handy 2001; Zimmerman et al. 1999; Zimmerman and Kohlstedt 2004). Shear stresses cause the segregation of melt from grain boundaries where it was originally formed, producing aligned melt domains distributed within melt-laden shear bands (e.g., Holtzman and Kohlstedt 2007). Furthermore, deformation leads to the migration of melt from high angle bands towards bands oriented at a lower angle to the main compression direction (Holtzman and Kohlstedt 2007). Many natural examples of melt segregation and melt extraction controlled by deformation and tectonic stress fields have been reported (e.g., Brown and Solar 1998; Collins and Sawyer 1996; Vigneresse 1995a,b; Weinberg 1999).

The relationships between deformation and partial melting are especially important in terms of the rheological behavior of the lower crust, where P-T conditions are often high enough for partial melting to occur. In order to gain insights into the deformation behavior of partially molten continental crust we performed deformation experiments on natural perthitic single crystals of K-feldspar. Feldspar was chosen in this case because it is a very common mineral of the continental crust. The quartz-free assemblage K-feldspar + plagioclase has a higher melting temperature than granitic compositions (containing quartz), so that this system has advantages in experimental deformation studies where crystal plastic deformation and melting effects are to be studied. In addition, there are few experimental studies (Tullis and Yund 1977; Willaime et al. 1979) on the deformation behavior of K-feldspars at high pressures and temperatures.

The experiments were performed with a solid medium deformation apparatus at pressures and temperatures where feldspar is expected to undergo partial melting (above the solidus temperature) and deform predominantly by crystal-plastic deformation mechanisms. The experiments were designed to study the relationships between cracking and partial melting, and to understand the influence these processes have on the chemical and mechanical properties of the material.

4.3 Methodology

4.3.1 Starting materials

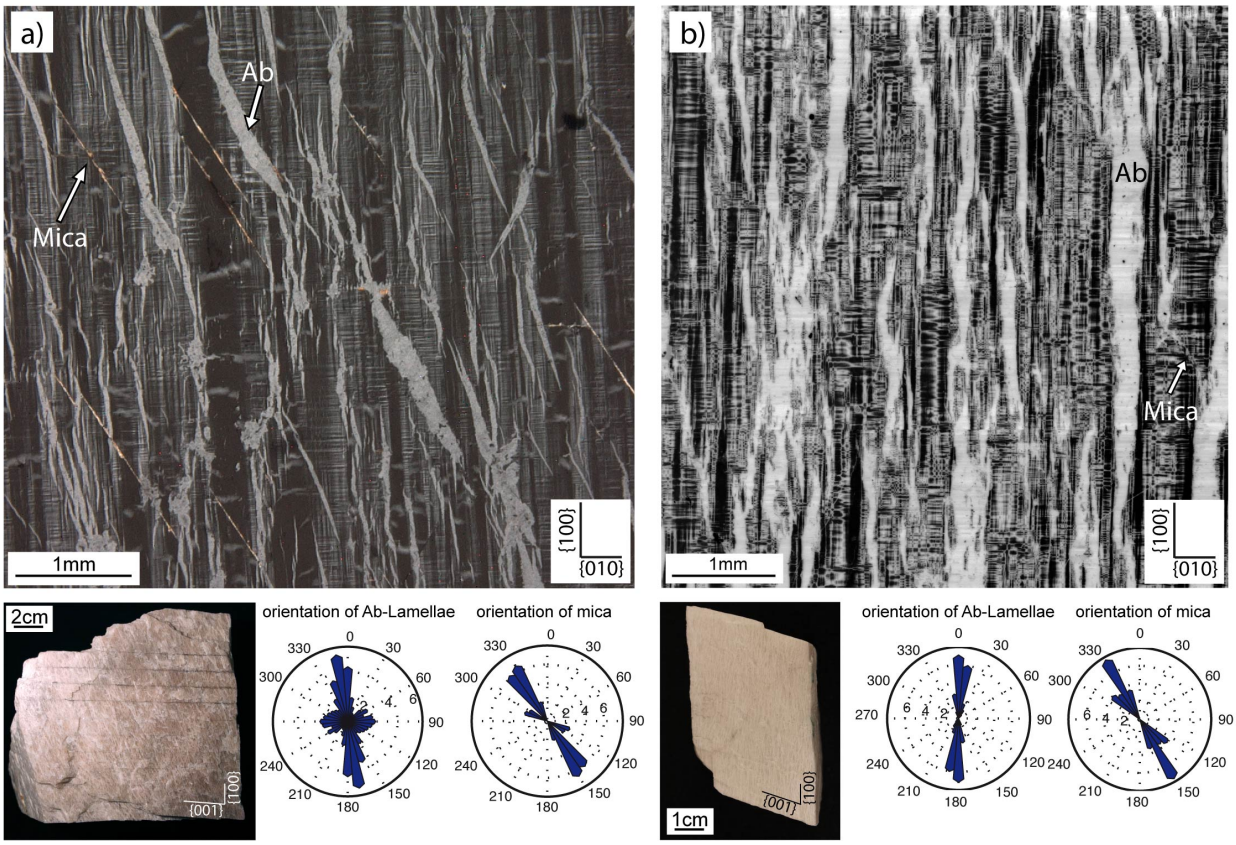

Fig. 4.1. Characterization of the two starting materials. **(a)** Pink K-feldspar and **(b)** White K-feldspar. Specimens were cored normal to the {010} plane. Both crystals contain albite lamellae, oriented mica grains (30° to the {100} plane), and two sets of twins (albite and pericline laws). The rose diagrams show a large number of small perthite lamellae oriented approximately parallel to the {100} plane in both crystals. The pink K-feldspar (a) contains some coarse albite lamellae oriented at 35° to {100} and shorter albite lamellae oriented parallel to {010}.

Two different natural K-feldspar single crystals were used (Fig. 4.1): (a) A pink variety and (b) a white variety. (a) The pink perthitic K-feldspar crystal (Fig. 4.1a) contains 84% K-feldspar ($Ab_{06}An_{0}Or_{94}$), 15% albite ($Ab_{98}An_{1.5}Or_{0.5}$), and volumetrically insignificant white mica (0.5%) and quartz (0.2 %). The chemical compositions of the different phases are given in Table 4.1.

The mineral appears uniform in color in hand specimen but 3 distinct sets of albite exsolution lamellae are observed under the light microscope (Fig. 4.1): (i) The main set of lamellae is oriented at 10-20° to the {100} plane. These lamellae, which have widths up to 250 μm and lengths in the mm-range, are often twinned, following the albite twin law. The thicker lamellae have sharp boundaries and locally open up in pockets containing small quartz grains. (ii) Small perthite lamellae (stringlets type after Alling 1938) 10-30 μm in width and up to 200 μm long are oriented predominantly parallel to the {100} plane (Fig. 4.1a). This set of lamellae is inhomogeneously distributed: lamellae rich regions alternate with perthite-free regions. (iii) Short perthite lamellae with poorly defined boundaries are oriented parallel to the {010} direction (Fig. 4.1a). These are typically 30-60 μm wide and terminate at the contacts with the main set of lamellae, but never crosscut them. Polysynthetic twinning is pervasively and homogeneously distributed throughout the whole pink K-feldspar matrix. The twinning occurs in two sets (albite and percline laws, Smith and Brown 1988) that intersect at approximately right angles and form a quadrille structure (cross-hatched twinning, FitzGerald and Mclaren 1982; Putnis 2002; Smith and Brown 1988). Thin (10 μm) and long (up to 700 μm) white mica domains are oriented at 30-40° to {010} corresponding to the {110} cleavage plane of the feldspar (Fig. 4.1a).

The pink K-feldspar contains a small amount of water. In a sample heated at 1000 °C for 2 h we determined by loss of ignition a water content of ~0.1-0.2 wt%. The water is assumed to be present in the form of fluid inclusions, structurally bound H_2O, and some absorbed H_2O.

(b) The white perthitic K-feldspar (Fig. 4.1b) contains 81% K-feldspar with a composition $Ab_{11}An_0Or_{89}$ and 19% albite lamellae ($Ab_{98}An_{01}Or_{01}$) (Table 4.1). The specimen shows similar macroscopic and microscopic characteristics to the pink K-feldspar. The major differences are: (i) The twin density in the white K-feldspar is higher, with shorter and thinner albite and pericline twins. (ii) The inhomogeneously distributed mica in the white K-feldspar forms shorter and thinner domains compared to the pink K-feldspar (iii) Albite exsolution lamellae of the main set do not terminate in quartz pockets. Instead, small (30-60 μm) quartz crystals are distributed along the boundaries of the albite lamellae. Occasionally, the small quartz crystals form aggregates around 50 μm in size. (iv) A higher amount of porosity is found along the albite lamellae/K-feldspar boundaries. (v) The set of albite exsolution lamellae oriented parallel to the {010} plane is missing.

	pink K-feldspar			white K-feldspar	
Phase	Matrix (K-fsp)	Ab-Lamellae	Mica	Matrix (K-fsp)	Ab-Lamellae
SiO_2	64.74	67.65	43.92	64.79	69.02
Al_2O_3	18.71	19.77	35.78	17.85	19.87
FeO	0.00	0.00	1.61	0.46	0.01
CaO	0.00	0.36	0.01	0.03	0.18
Na_2O	0.68	11.73	0.49	1.25	12.06
MgO	0.00	0.00	0.04	0.00	0.00
K_2O	15.70	0.08	10.59	15.25	0.16
MnO	0.06	0.00	0.01	0.00	0.00
Total	99.90	99.59	92.44	99.62	101.30
Ab %	6.20	97.88		11.02	98.31
An %	0.00	1.66		0.13	0.82
Or %	93.80	0.46		88.85	0.85

Table 4.1 Chemical compositions (determined from EMPA analyses) of the two feldspar single crystals used as starting material. Measurements are given in wt%.

4.3.2 Sample preparation

Two different types of samples were prepared: (i) cylindrical samples for axial compression and hydrostatic experiments and (ii) powder samples for hydrostatic experiments.

(i) All cylindrical samples, which had a length of 10-12 mm and a diameter of 6.3 mm, were cored normal to the {010} plane of the crystals (the orientation of the crystals was determined macroscopically using the geometry of the well-developed crystal planes and the orientation of the albite lamellae). The samples were air-dried at 120 °C and wrapped in Ni-foil prior to inserting them into the can-shaped Pt-jackets and weld sealing. In samples with H_2O added, 0.1-0.2 μl distilled water (corresponding to 0.1-0.2 wt%) was introduced using a micropipette to the lower part of the capsule, beneath the sample, in order to reduce potential evaporation of the water during the subsequent welding process. Evaporation of the water during the welding process was also prevented by using a milli-second welding time in order to minimize heating of the sample.

(ii) For the powder experiments the K-feldspar starting material was ground in an agate mortar. The powder fraction with a grain size of 12-20 μm was obtained by sieving the ground rock through a series of filter papers and subsequently drying the powders at 110 °C. 0.1 g of dry powder was placed between 45° pre-cut alumina forcing blocks inside a Ni-foil and weld-sealed Pt-jacked.

4.3.3 Experimental and analytical procedures

Two different types of experiment were performed in a modified Griggs type solid medium deformation apparatus (Tullis and Tullis 1986): axial compression and hydrostatic experiments. Both types of experiment were performed on K-feldspar single crystals, and additional hydrostatic experiments were also performed on powder samples in order to evaluate the microstructures, chemical effects, reactions and melting processes with and without deformation. In all experiments NaCl was used as the confining medium and Alumina was used for the outer pistons. The temperature was monitored with a Pt-Pt10%Rh S-type-thermocouple placed in the middle of the sample (along the outer margin).

Sample	Pc [GPa]	T [°C]	έ [x$10^{-6}$$s^{-1}$]	Total time [h]	Strain [%]	Experiment type	Starting material	Water added
mn216	1.00	900	2.1	48	33	Axial compression	White K-Fsp	As Is
mn218	1.00	900	1.6	44	9	Axial compression	White K-Fsp	0.2wt%
mn221	1.00	900	1.3	38	15	Axial compression	White K-Fsp	0.1wt%
mn222	1.00	900	1.2	69	23	Axial compression	Pink K-Fsp	As Is
mn223	1.00	900	1.3	89	36	Axial compression	Pink K-Fsp	0.1wt%
mn250	1.50	900	1.8	50	25	Axial compression	Pink K-Fsp	As Is
mn258	0.75	900	1.4	76	28	Axial compression	Pink K-Fsp	As Is
mn265	1.00	900	0	95	0	Hydrostatic	Pink K-Fsp	As Is
mn267	1.00	900	0	42	0	Hydrostatic	Pink K-Fsp	Powder
mn271	1.00	900	0	71	0	Hydrostatic	Pink K-Fsp	As Is
mn276	1.50	900	1.5	87	35	Axial compression	Pink K-Fsp	As Is
mn292	1.00	900	1.1	37	3	Peak strength	Pink K-Fsp	As Is
mn293	0.75	900	1.1	44	2	Peak strength	Pink K-Fsp	As Is
mn294	0.75	900	1.1	32	3	Peak strength	Pink K-Fsp	As Is
mn295	0.75	900	1.2	68	18	Axial compression	Pink K-Fsp	As Is
mn296	1.50	900	1.6	93	30	Axial compression	Pink K-Fsp	As Is
mn297	1.50	900	1.2	41	2	Peak strength	Pink K-Fsp	As Is
mn298	1.00	700	1.1	89	21	Axial compression	Pink K-Fsp	As Is
mn300	0.75	700	1.3	41	12	Axial compression	Pink K-Fsp	As Is

Table 4.2 Summary of deformation conditions of all performed experiments (Pc= Confining pressure, T= Temperature, ε̇= strain rate, t= total time at Pc and T).

For each experiment the hydrostatic conditions (temperatures of 700 - 900 °C and pressures of 0.75-1.5 GPa) were typically reached in 6 h or less by a step-wise increase of confining pressure and temperature. Once the desired conditions were reached, the samples were deformed by advancing the piston (σ_1) at a constant strain rate of ~10^{-6} s^{-1} up to a maximum axial shortening of 40%. At the end of the experiments the motor was stopped and the samples immediately quenched to 200 °C. Subsequently, pressure and load were slowly decreased to atmospheric conditions in order to minimize the formation of unloading fractures.

The samples for hydrostatic experiments were prepared and taken to conditions (900 °C, 1.0 GPa) in the same way as for axial compression experiments. The samples were held at hydrostatic conditions for 71 hours, corresponding to the period of time necessary to reach 35 % strain in an axial compression experiment. After the hydrostatic heat treatment the samples were quenched and slowly depressurized to atmospheric conditions. The conditions of all the experiments are summarized in Table 4.2.

Force and displacement data recorded during each experiment were processed using the Matlab program RIG (http://sites.google.com/site/rigprogram/). All stress-strain curves presented in this work have been corrected for a cross-section increase during deformation on the assumption of homogeneous deformation at constant volume.

After deformation the samples were cut normal to the (often conjugate) set of shear planes that accommodated the main displacement during deformation. This section orientation is always normal to the {100}-plane. The cut surfaces were impregnated with epoxy and standard polished petrographic sections with a thickness of 30 μm were prepared. Examination of the samples was conducted using optical and scanning electron microscopy (SEM). Backscattered imaging (BSE image) in the SEM was carried out using a field-emission Philips XL30 ESEM with an EDX detector (ZMB Basel) and a ZEISS EVO50 at the University of Bern. The images were taken at a beam current of 15 nA and an acceleration voltage of 20 kV. Quantitative element analyses were performed with a JEOL Superprobe 8200x (University of Copenhagen and ETH Zürich) at 15 kV and 20 nA, using a spot size of 5 μm. Compositions of the melt phase, which is commonly unstable under normal beam settings, were measured with a low beam current of 10-12 nA, a spot-size of 10-12 μm, and counting time <10 s in order to avoid significant Na- and H_2O-loss.

Crystallographic preferred orientation (CPO) data were collected using the electron backscatter diffraction (EBSD) method (Adams et al. 1993) in a FEI-Quanta 3D FEG-FIB scanning

electron microscope equipped with an EDAX-TSL Digiview IV EBSD detector and TSL software OIM 5.31 at the GFZ-Potsdam. The samples were polished using standard methods with diamond pastes of different grain sizes down to 0.25 μm and chemically polished using a soft cloth and an alkaline solution of colloidal silica (SYTON) (Flynn and Powell 1979) for 2 hours. The EBSD analyses were conducted under low vacuum (10 Pa of H_2O) on an uncoated sample using 15 kV accelerating voltage, 8 nA beam current, 12 mm working distance, step size of 1 μm, and 70° sample tilt. The acquired diffraction patterns for the chemically homogenized feldspar grains (high temperature monoclinic structure) were indexed using the crystallographic data for sanidine. The standardization of the confidence index (CI) of different points and CI correlation between neighboring points were carried as filtering procedures, and only data with CI>0.2 were considered in the pole figures, which were plotted using one point per grain.

The distribution of mineral phases and the amount of melt formed in the specimens were estimated from SEM images processed with Adobe Photoshop and ImageSXM (www.liv.ac.uk/~sdb/ImageSXM/), as well as a number of macros developed by Renee Heilbronner (http://pages.unibas.ch/earth/micro/index.html). Melt pockets were recognized in backscattered electron images (BSE) by means of their characteristic morphology and the presence of spherical fluid bubbles (described below).

4.4 Results

4.4.1 Mechanical data

Representative stress-strain curves from the experiments are shown in Fig. 4.2

At 700 °C the K-feldspar single crystals show peak stresses ~10 % above the confining pressure values (Fig. 4.2a). The peak-strength increases with increasing confining pressure (Fig. 4.2a). After peak stress (at ~5 % strain) there is pronounced weakening of at least 10 % in differential stress. This behavior, i.e., strength above the confining pressure values and the positive dependence of peak stress on confining pressure, is characteristic of brittle deformation.

At 900 °C there are no systematic strength differences between the pink and white K-feldspars (Fig. 4.2b,c). Furthermore, the addition of 0.1 wt% H_2O does not systematically change the mechanical behavior with respect to as-is-samples (Fig. 4.2b). The addition of 0.2 wt% H_2O results in a lower strength of the K-feldspar, so that subsequently samples were deformed without addition of H_2O in order to avoid variability due to different H_2O contents. As there is no systematic

difference in mechanical behavior, all samples are described in the following text without differentiating between as-is, water added, and pink or white perthite.

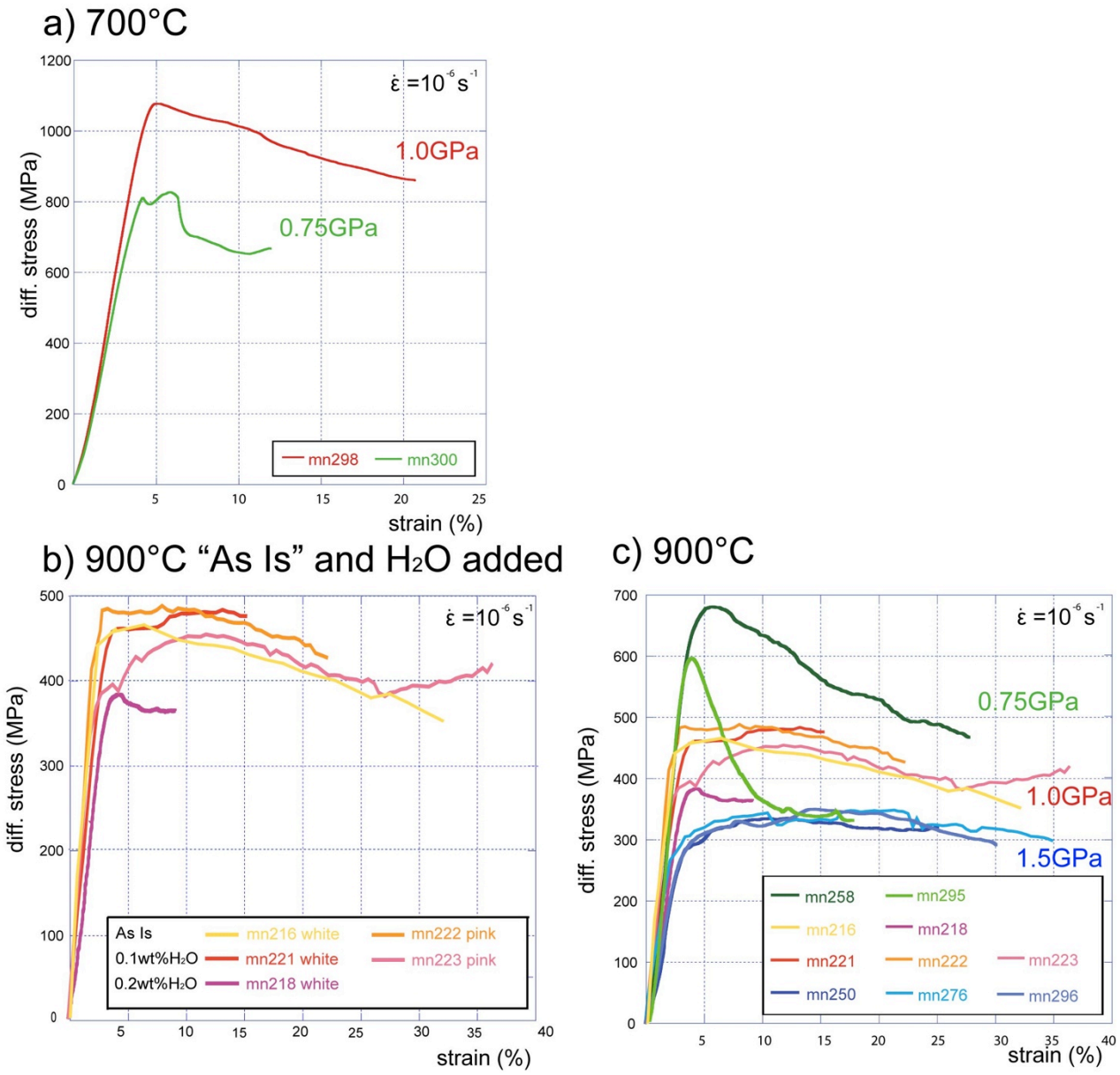

Fig. 4.2 Stress-strain diagrams for K-feldspar deformed at different confining pressures and temperatures at a strain rate of ~1 x 10^{-6} s^{-1}. **(a)** Experiments at 700 °C and confining pressure of 0.75 GPa (green) and 1.0 GPa (red). Samples were deformed as-is. **(b)** Samples deformed as-is and with added H_2O (0.1 and 0.2 wt%) do not show systematically different strengths at 900 °C, 1.0 GPa confining pressure. **(c)** White K-feldspar (mn216, mn218, mn221) and pink K-feldspar (all others) deformed at 900 °C and confining pressure of 0.75 GPa (green), 1.0 GPa (red-yellow) and 1.5 GPa (blue). Note that there is no systematic strength difference between the two starting materials.

Samples deformed at 900 °C show flow stresses of 30 - 70 % confining pressure (Pc) values after 5-10 % strain (Fig. 4.2c). There is a clear dependence of flow stress on confining pressure:

Samples deformed at Pc =0.75 GPa show a peak strength 20-30 % higher (600-680 MPa) than at 1.0 GPa confining pressure, and 60-80 % higher than at 1.5 GPa confining pressure. Samples deformed at 1.5 GPa confining pressure attain the lowest flow stresses (330 MPa at steady state) after 5-10 % strain, while the 1.0 GPa confining pressure experiments show intermediate flow stresses (390-480 MPa). Weakening after peak stress is pronounced at 0.75 GPa confining pressure, whereas at 1.5 GPa there is no weakening but instead the samples deform by steady state flow after yielding. Sample mn295 (deformed at 0.75 GPa) weakened to the stress levels of the 1.5 GPa experiments after ~10 % strain. Thus, with increasing confining pressure at 900 °C, both the peak and flow stresses decrease, and weakening becomes less pronounced.

4.4.2 Microstructural observations

4.4.2.1 Samples deformed at 700 °C

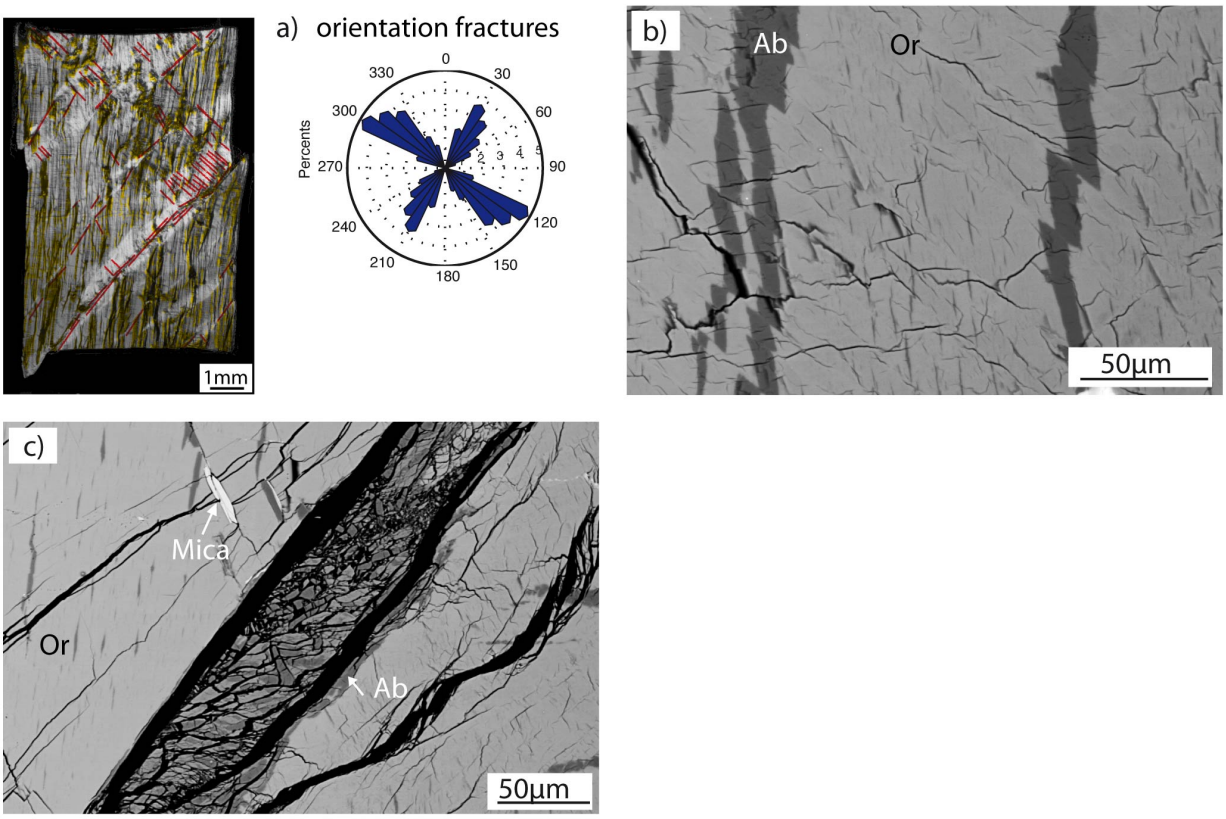

Fig. 4.3 Microstructure of K-feldspar deformed "As Is " at 700 °C and confining pressure of 1.0 GPa. Compression direction is vertical in all figures. **(a)** Cross-polarized light micrograph of the deformed sample. Red lines mark the cracks, whose orientations are represented by the rose diagram on the right. Albitic lamellae are colored in yellow. **(b)**

SEM backscatter image (BSE) showing extensive cracking in the deformed samples. The albitic lamellae are displaced by very small shear cracks oriented at 50° to the compression direction. Sub-horizontal cracks are interpreted as unloading cracks forming during decompression of the sample after deformation. **(c)** SEM backscatter image (BSE) of a fault gouge along the major through-going shear-fracture. Note that the fine grained fragments have two different composition (dark material = albite, lighter part = K-felspar).

Experiments performed on K-feldspar single crystals at 700 °C show extensive cracking distributed throughout the whole sample (Fig. 4.3). Major through-going fractures and asymmetric shear cracks develop at 45-55° to the compression direction (Fig. 4.3a). The through-going shear cracks have displacements up to 1 mm (Fig. 4.3a) and are surrounded by ~0.5 mm wide regions with patchy undulatory extinction and different extinction angles (lattice rotation ~15°) (Fig. 4.3a). The lattice rotation, which occurs in the regions around major cracks, is accommodated by closely spaced (few μm) fractures with displacements up to 20 μm (determined from offset twins and albite lamellae; Fig. 4.3b). These observations are similar to those made by Tullis and Yund (1987) in experimentally deformed plagioclase. Along the through-going shear-fractures the grain size is significantly reduced and fault gouge is present (Fig. 4.3c). EPMA analyses show that the small gouge fragments maintain the original chemical composition of the surrounding orthoclase matrix and/or the albitic lamellae. Narrow albite lamellae close to major shear fractures maintain well defined boundaries (Fig. 4.3b). White mica does not show any signs of decomposition, even in densely cracked regions (Fig. 4.3c). Samples deformed at 1.0 and 0.75 GPa do not show systematic differences in microstructures, although there is a higher density of cracks in the samples deformed at higher confining pressures.

4.4.2.2 Samples deformed at 900 °C

Fracturing and brittle microstructures

Three types of fractures were observed in samples deformed at 900 °C: (i) axially oriented fractures, (ii) conjugate shear fractures and (iii) through-going shear zones

(i)Axial fractures that are oriented subparallel to the compression direction (σ_1) developed in all specimens, but are more prominent in the samples with H_2O added. The fractures, which are 300-

500 μm long and lack displacement, typically surround the main shear fracture systems and terminate in trails of aligned porosity, most likely representing healed fractures (Fig. 4.4).

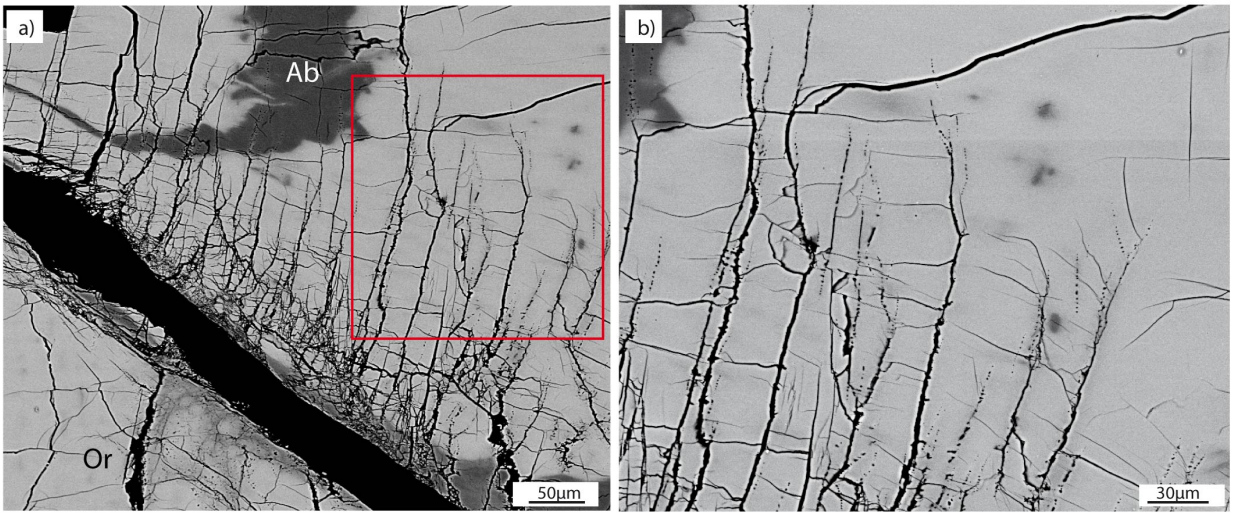

Fig. 4.4 Microstructures of a pink K-feldspar deformed at 900 °C, 1.0 GPa with addition of 0.1 wt% H_2O. Compression direction is vertical in all images. **(a)** Axial cracks oriented subparallel to the maximal compressive principal stress nucleate from major shear cracks. The red rectangle marks the position of the detailed picture in (b). **(b)** The parallel axial cracks have lengths of 300-500 μm and a spacing of few μm and terminate as trails of aligned porosity, marking the propagation direction of the fractures and probably representing healed cracks.

(ii) Shear fractures oriented at 30-60° to the compression direction are pervasive in all samples (Fig. 4.5). In low-strain-samples the shear cracks form short (from 10´s of microns to ~1 mm length), parallel sets that are concentrated in the more strongly deformed parts of the samples (Fig. 4.5a), corresponding to the highest temperature regions. In higher strain samples (Fig. 4.5b) the shear fractures are longer and interconnect to form conjugate sets. Displacement along the shear fractures is revealed from the offset of albite lamellae or twins and varies from a few μm in low strain experiments to 100-150 μm in high strain experiments.

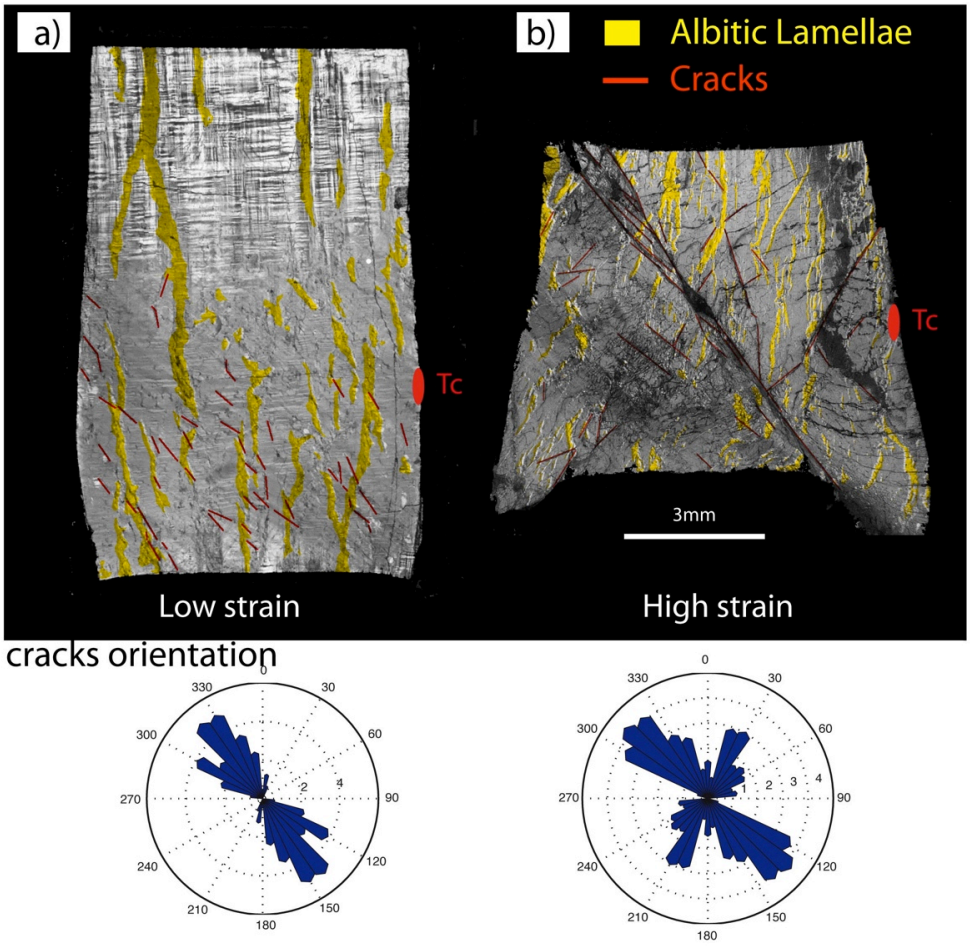

Fig. 4.5 Light micrographs (crossed polarized) of deformed samples, showing the distribution and types of brittle features formed at low (a) and high (b) strain. Albite lamellae are colored in yellow and cracks in red. The final position of the Thermocouple (Tc) is also marked. The rose diagrams show the orientation of the cracks with respect to the axial shortening direction (vertical). **(a)** White K-feldspar (mn218) deformed with 0.1 wt% H_2O added, at 900 °C, 1.0 GPa up to 9% strain. Short parallel cracks are oriented at 30-50° to σ_1. The deformation is concentrated in the lower part of the sample, where the temperature was highest during deformation. **(b)** A pink K-feldspar sample (mn250) deformed at 900 °C, 1.5 GPa up to 25% strain. Cracking is concentrated along a through-going deformation zone oriented at 50° to σ_1. Asymmetric conjugate shear cracks, which develop mainly in the central part of the sample, are oriented at an angle of 30-60° to the main compression direction. Displacement along the cracks is well visible by the relative position of the displaced albite lamellae.

(iii) High strain samples may develop pronounced through-going shear zones at an angle of 40-45° to σ_1 (Fig. 4.5b). These are surrounded by a large number of smaller, subparallel microfractures whose density increases towards the shear zones. The presence of micro-fractures around the main shear zones causes the variable extinction angle of such regions with respect to the intact crystal, as observed by (Tullis and Yund 1987, 1977). Locally, along the through-going shear zones fine-grained fault gouges are found (Figs 4.6a-d).

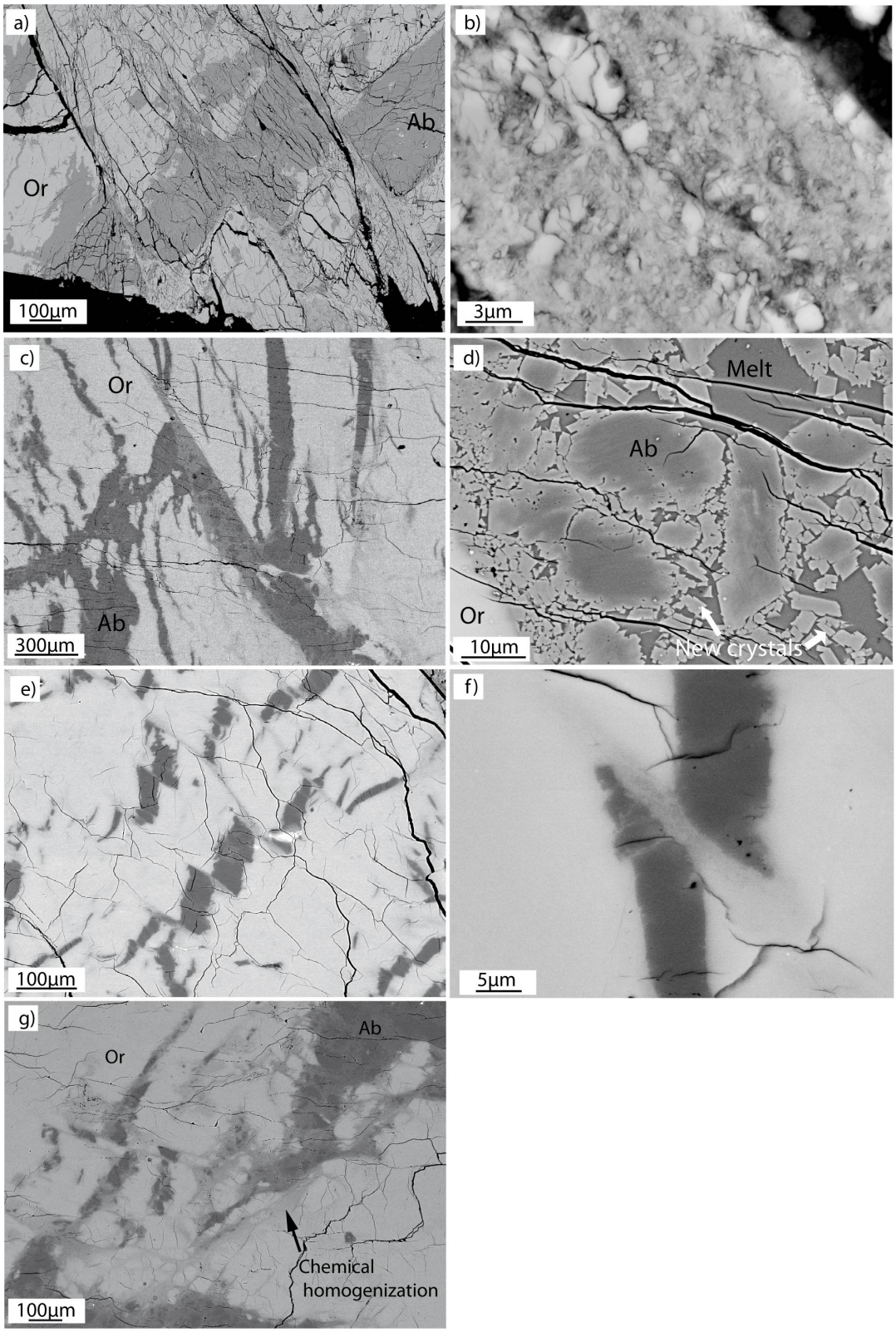

Fig. 4.6 SEM backscatter images (BSE) of cracks and related microstructures in pink and white K-feldspar samples, both deformed as-is. Compression direction is vertical in all images. **(a)** Formation of parallel shear cracks in the lower part of

sample mn250 (900 °C, 1.5 GPa). Differential movement of the fractures is evident from the offset of the albite lamellae. Formation of fine-grained gouge often occurs along the main fractures. **(b)** Detail of (a). Fine-grained crushed fragments in through-going fractures. Angular fragments have a size of <<1 to 3 μm. Neither melting nor compositional changes are observed. **(c)** Gouge formed along a shear fracture in the central part of the sample mn222 (900 °C, 1.0 GPa). Note the chemically homogenized composition of the fine-grained gouge. **(d)** Detailed picture of (c). The small gouge fragments show a chemically homogenized composition. On the contrary the core of the larger (20-50 μm) fragments maintain the same composition as the starting material. Melt is present in between the gouge fragments. **(e)** Sample mn216 (900 °C, 1.0 GPa). Shear fractures oriented at 50° to the compression direction are detectable only due to the related formation of 20 μm wide zones of chemical homogenization. **(f)** Displacement along the shear cracks is clearly visible by the displaced albite lamellae. In the chemical homogenized zone no particles are distinguishable by means of SEM.

At the edges of the samples (Figs. 4.6a,b) the gouges are melt free and the very fine-grained angular fragments (with sizes ranging from submicron to 20 μm) can be clearly resolved in SEM images. On the contrary, in the central and hottest parts of the samples (Figs. 4.6c,d) the gouges consist of a few larger fragments surrounded by an extremely fine-grained (individual fragments cannot be resolved at a magnification up to 17000x) and chemically homogenized matrix. The few larger (20-70 μm) fragments show no chemical homogenization in their cores, but develop a thin rim of homogenized composition, most likely from crystallization of new grains on their edges (Fig. 4.6d). Melt is found in small pockets randomly distributed in the chemically homogenized matrix (Fig. 4.6d) of the gouges (chemical homogenization and melt are described in detail in the following sections).

Partial melting

Melting in the perthite single crystals is almost always spatially associated with brittle deformation: melt occurs along through-going fractures containing fine-grained gouges (Fig. 4.6d) and along smaller, isolated shear cracks (Fig. 4.7).

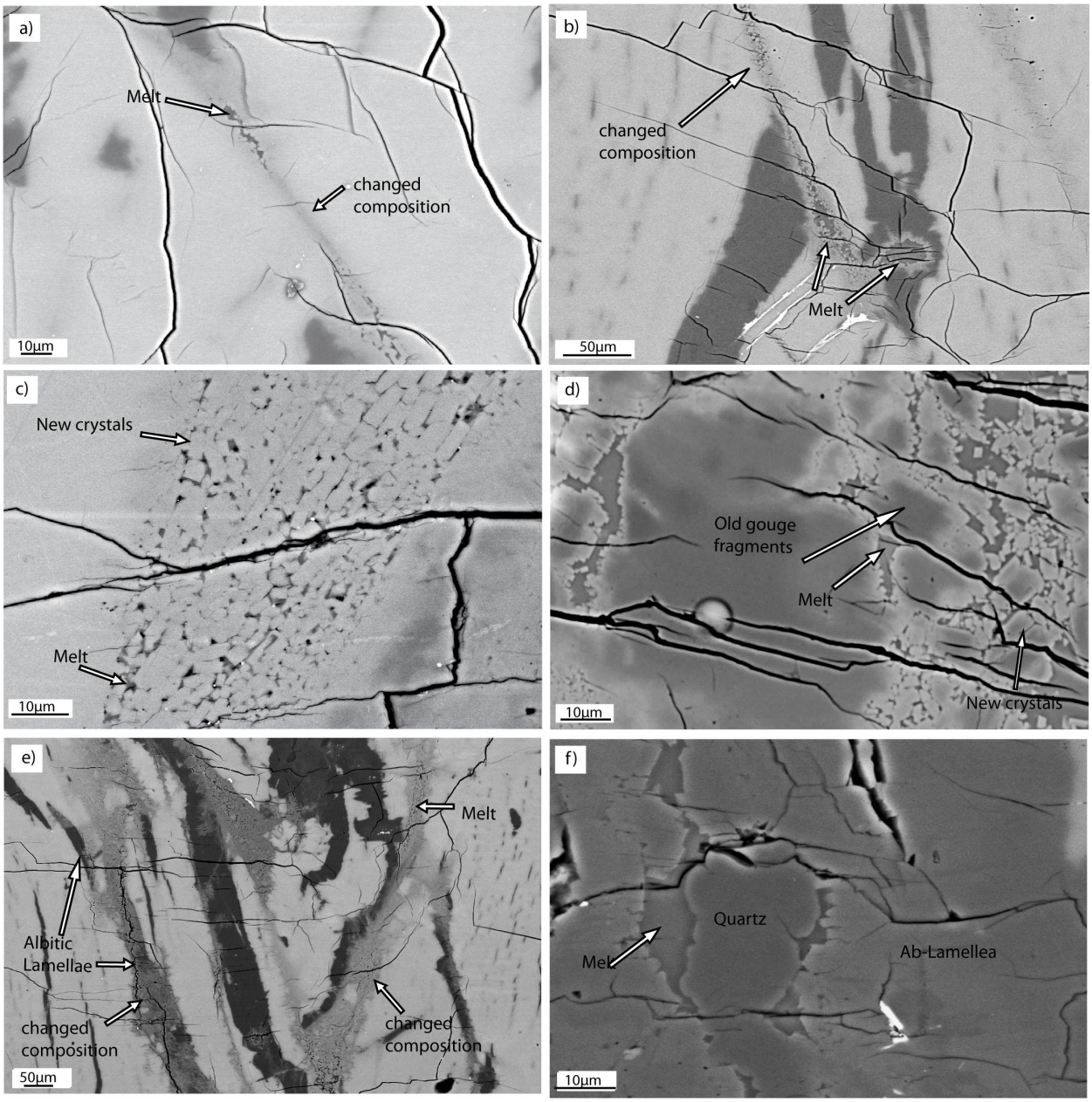

Fig. 4.7 SEM backscatter micrographs of microstructures involving melting in experiments at 0.75, 1.0 and 1.5 GPa, 900 °C. Compression direction is vertical in all images. **(a)** Formation of isolated melt pockets, containing euhedral new crystals, along a shear fracture in sample mn258. The crack is visible as a chemically homogenized region. The elongated melt domains are orientated at ~40° to the compression direction. **(b)** Melt pockets formed along a shear crack, with displacement of ~100 μm. A chemically homogenized zone surrounds the melt domain, which contains small newly formed crystals. Melt is also found in the albitic lamellae, where it is collected in an oval pocket with a diameter of around 40 μm. **(c)** Formation of oriented euhedral crystals with homogeneous composition along a shear fracture in sample mn276. The crystals are oriented in the direction of shear. Residual melt occurs in interstitial spaces. **(d)** Melt pockets distributed in a gouge (sample mn222). The chemically unchanged cores of the larger fragments are overgrown by chemically homogenized rims, whereas the small grains have a completely homogenized composition. **(e)** Extensive

compositional changes in sample mn296, (900 °C, 1.5 GPa). The backscattered SEM image shows different compositions (different grey contrast) of homogenized regions, suggesting that chemical homogenization arises by the mixing, in different amounts, of the Or-rich matrix with the albitic lamellae present in the starting material. Melt is present in the chemically homogenized regions. **(f)** Melt formed around a small quartz grain contained in an albite lamellae in sample mn223. The melt is distributed along grain boundaries oriented parallel to the compression direction. The quartz grain shows rounded edges indicating partial melting.

The melt is typically distributed interstitially between large clasts and gouge particles but it may also coalesce to form melt domains of different size and irregular shape (Figs. 4.7d,f). Locally, elongation of melt domains occurs along the shear fractures (Figs. 4.7a,b). Often the melt domains contain densely packed, small (up to 20 μm), newly formed euhedral crystals (Fig. 4.7c) with a chemical composition intermediate between the original composition of the K-feldspar matrix and the albite lamellae (Fig. 4.8).

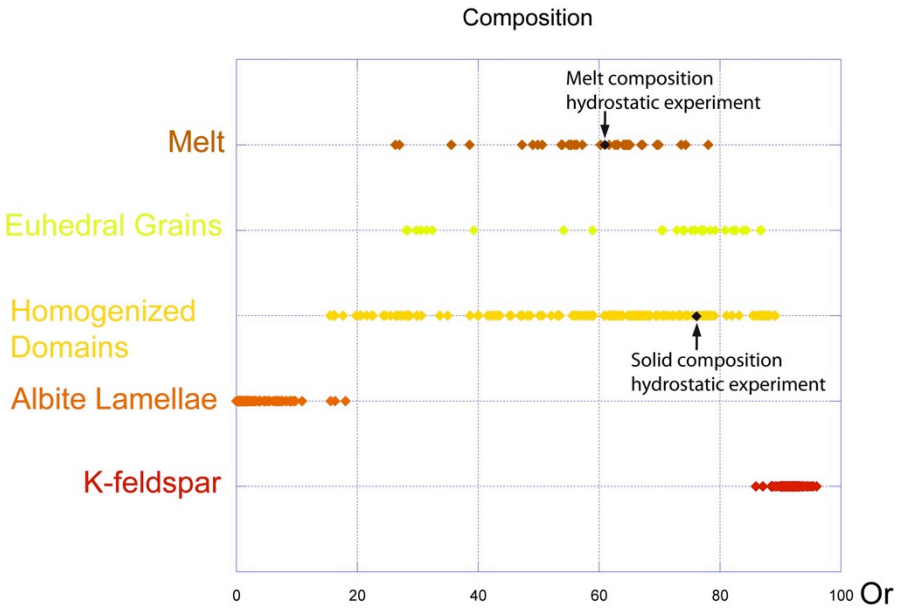

Fig. 4.8 Chemical compositions of albite lamellae, K-feldspar matrix, chemically homogenized domains, melt and new euhedral grains. The compositions of albite lamellae and K-feldspar are fairly consistent but the chemically homogenized domains and melt show a wide range of compositions suggesting that they are derived from mixing between the K-feldspar and the albite lamellae. The newly formed euhedral crystals show, for the most part, two distinct compositions of ~$Ab_{70}Or_{30}$ and ~$Ab_{20}Or_{80}$. The compositions of the melt and homogenized fragments in the hydrostatic powder experiment are marked in black.

EBSD analysis (Fig. 4.9) of zones containing melt and newly formed euhedral crystals shows a well-defined and strong crystallographic preferred orientation. In the pole figures (Figure 4.9d), the orientation of the new euhedral grains shows a strong alignment of their (010) planes subparallel to the orientation of the shear plane, while the poles of (100) axes are parallel to the inferred shear direction of the fractures.

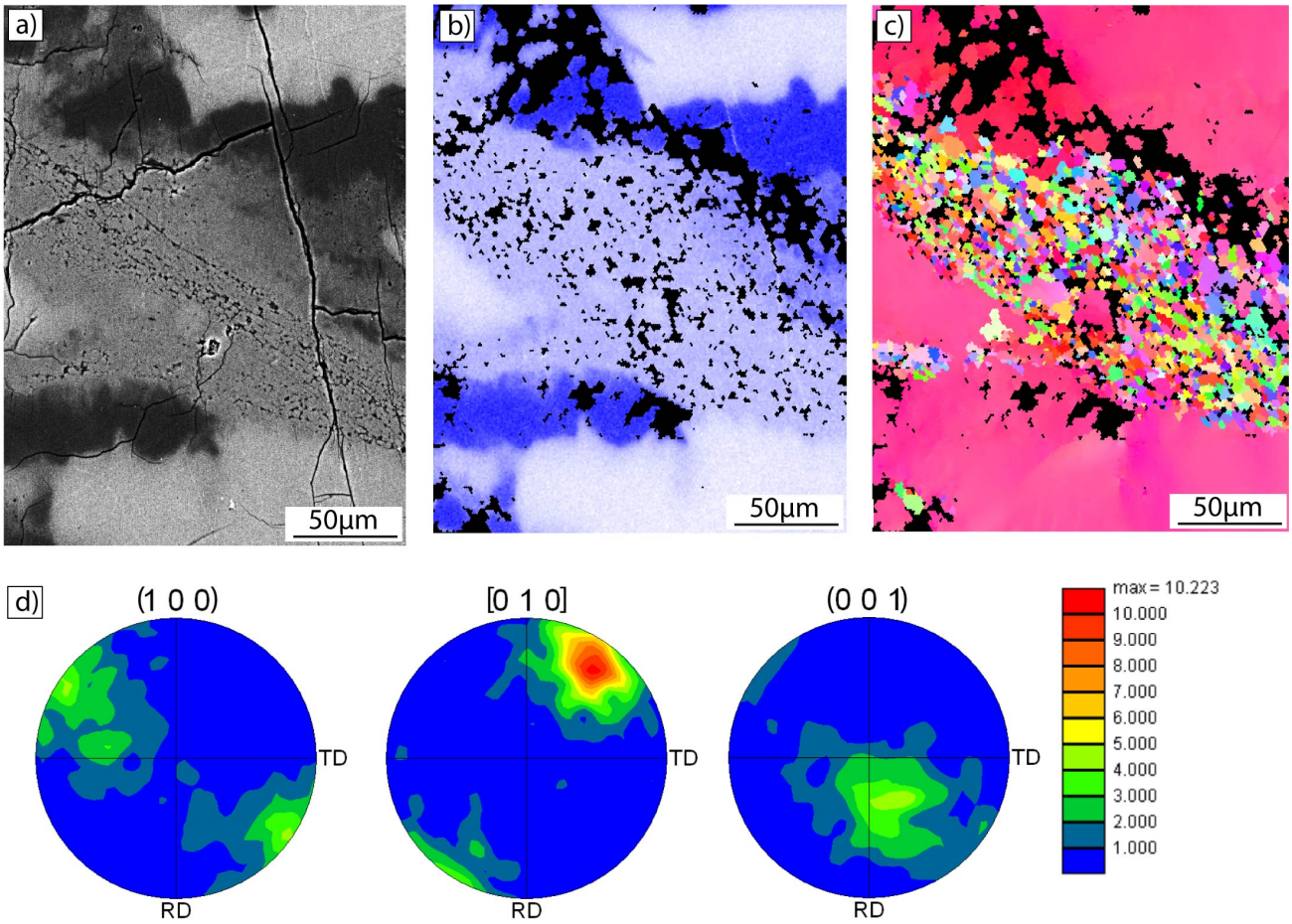

Fig. 4. 9 Crystallographic preferred orientation (CPO) measured with EBSD of a chemical homogenized region containing melt and newly formed euhedral crystals. The compression direction is horizontal in all figures. **(a)** SEM backscatter image of the analyzed region. Albite lamellae (dark gray), Or-rich matrix (light grey) and chemical homogenization (intermediate grey in the center of image) are easily distinguishable. **(b)** Na element distribution map. **(c)** Processed orientation maps of the homogenized region. **(d)** Pole figures (equal area, upper hemisphere) of the chemically homogenized domain showing a strong CPO.

Melt domains in the fine-grained gouge (Fig. 4.7d) are generally larger (diameter up to 20 μm) than the elongated melt regions along the shear fractures, and also typically contain newly formed crystals. The new grains either nucleate on gouge fragments forming irregular rims, or as

new euhedral grains with straight boundaries, randomly distributed in the melt domains (Fig. 4.7d). All new grains have a chemical composition different from that measured in the starting material. This composition is intermediate between the Or-rich matrix and the albite lamellae (Fig. 4.8). Below, this intermediate composition is referred to as "chemically homogenized".

Melt also forms around small quartz grains contained in the albite lamellae (Fig. 4.7f). In this case the melt is present as a film (up to 10 μm thick) along grain boundaries. The relict quartz crystals show smooth, lobate boundaries resulting from the partial melting process (Fig. 4.7f).

The chemical composition of the melt is inhomogeneous and varies from ~$Ab_{70}Or_{30}$ to ~$Ab_{20}Or_{80}$ (Fig. 4.8) depending on the amount of material that has melted and the local composition (i.e., local volume ratio of Albite and K-feldspar). Melt formed in the K-feldspar-rich regions of the perthite shows Or-rich compositions whereas melt formed close to albite lamellae shows more albitic compositions.

White mica, if present along the {110} cleavage planes (Fig. 4.1), is usually preserved in the undeformed and/or colder parts of the samples (e.g., sample ends close to pistons). In the regions of melt formation (corresponding to the more cracked and deformed regions of the samples), there is either no white mica observed or mica is replaced by fine grained aggregates that have a dark brown color in the optical microscope.

Determination of the melt content

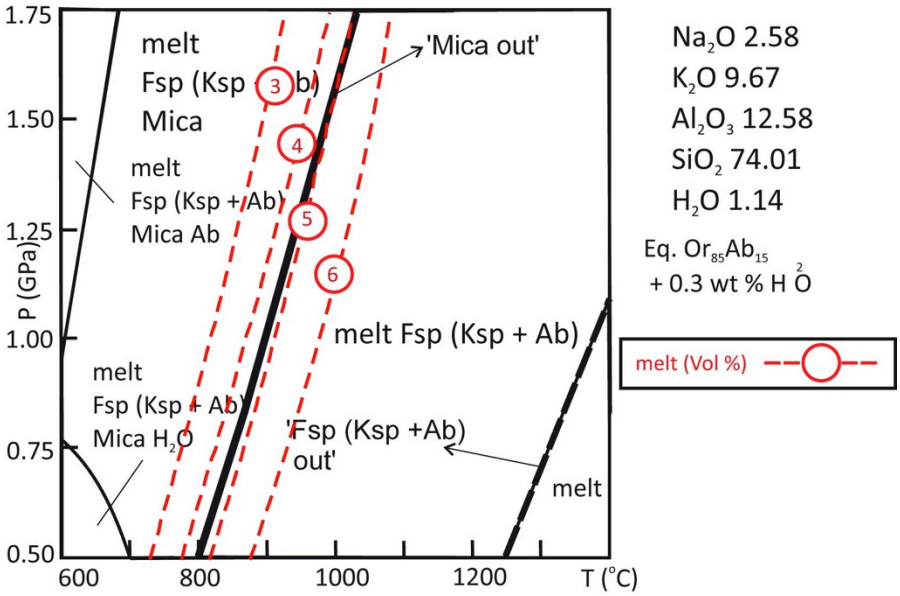

Fig. 4.10 P-T Pseudosection for the system Ab-Or-H_2O. Phase topology of sanidine (Ksp + Ab), mica and melt are shown in red. The volume isoplate of the melt is shown in black. Thermodynamic data predict at 1.0 GPa and 900 °C a melt volume of around 5 wt%.

In order to determine the theoretical melt content expected for our deformation conditions we modeled a phase diagram for alkali feldspar (Na-K binary feldspar) in the NKASH system using

PerpleX_07 (Connolly 2009). The re-integrated composition of the pink perthite single crystal (Fig. 4.2, table 4.1) and a water content of 0.3 wt% were used for the calculation. For the pseudosection calculation the following solution models were used (refer to the solution_model.dat file for details): mica (Coggon and Holland 2002), melt (Holland and Powell 1998) and sanidine (Thompson and Waldbaum 1969).The CORK model (Holland and Powell 2001; Holland and Powell 1998) was used as fluid equation of state for H_2O.

The calculated pseudosection predicts a melt content of around 5 vol% at 1.0 GPa and 900 °C (Fig. 4.10). With increasing pressure the melt fraction decreases at any given temperature due to the normal dependency of the melting temperature with pressure (i.e., increase of melting temperature with increasing pressure). It should be emphasized that the amount of melt calculated is almost within the error of the thermodynamic modeling. Therefore, the calculated phase diagrams serve only to discuss the phase relationships in a semi-quantitative way.

The negative dependency of melting point with increasing pressure present in the lower left corner of the diagram is caused by the presence of mica in the system. The presence of mica in the system also influences the theoretical melt initiation, shifting the melting point towards lower temperatures due to the extra water released during mica breakdown.

To determine the total melt percentage of the K-feldspar-Ab-H_2O-system a hydrostatic experiment was performed on pink K-feldspar powder (grain-size of 12-20 μm) at 900 °C and 1.0 GPa for 42 h (Fig. 4.11).

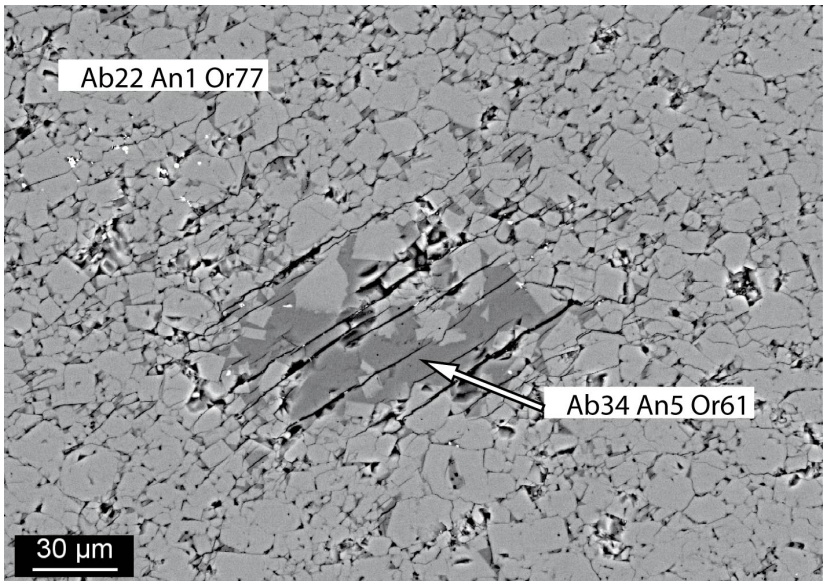

Fig. 4. 11 SEM backscatter image of a powder sample (mn267) hydrostatically hot pressed at 900 °C and 1.0 GPa for 34 h. The original powder material was composed of albite and K-feldspar fragments. After hot pressing the material shows a completely homogenized chemical composition of $Ab_{22}An_1Or_{77}$ and formation of melt with a composition of $Ab_{34}An_5Or_{61}$. Most of the melt is collected in large melt pockets randomly distributed in the sample

The powder was placed between alumina pistons cut at 45° to the compression direction but was not deformed. In the hydrostatic powder experiment (Fig. 4.11) most of the melt collected in relatively

large melt pockets of homogeneous composition ($Ab_{34}An_5Or_{61}$) randomly distributed throughout the solid powder phase (also with uniform composition $Ab_{22}An_1Or_{77}$). Image analysis indicates that the fine-grained powder produces a melt fraction of $\phi_{vol} \sim 0.05$ to 0.06, consistent with estimates from thermodynamic modeling discussed above (Fig. 4.10). The H_2O content of the melt is ~10 wt%, determined as the difference between the total of the EPMA analyses and 100 %. This value may have an error of at least ± 1 wt% given the problems of determining the H_2O-contents of melts (Johannes and Holtz 1996). The H_2O-content of the melt was only determined in the powder sample, because most melt domains in the deformed samples are too small to be measured by EMPA.

In the deformed single crystal experiments the estimation of the melt fraction was difficult due to the low and variable melt percentage, and because the melt was well dispersed between the fine-grained gouge fragments formed along the shear fractures. However we observed in samples deformed at 900 °C and 0.75 GPa a general increase of melt fraction with increasing strain (Fig. 4.12): the most strongly deformed sample (18% strain) contains a considerably larger amount of melt than the low strain experiment (3% strain) in which almost no melt was detected. Conversely, in samples deformed at 900 °C and 1.5 GPa the melt fraction did not depend on strain. After only 3% deformation (where the stress is ~300 MPa, 10% below maximum peak values) the sample contained almost the same amount of melt as the high strain samples.

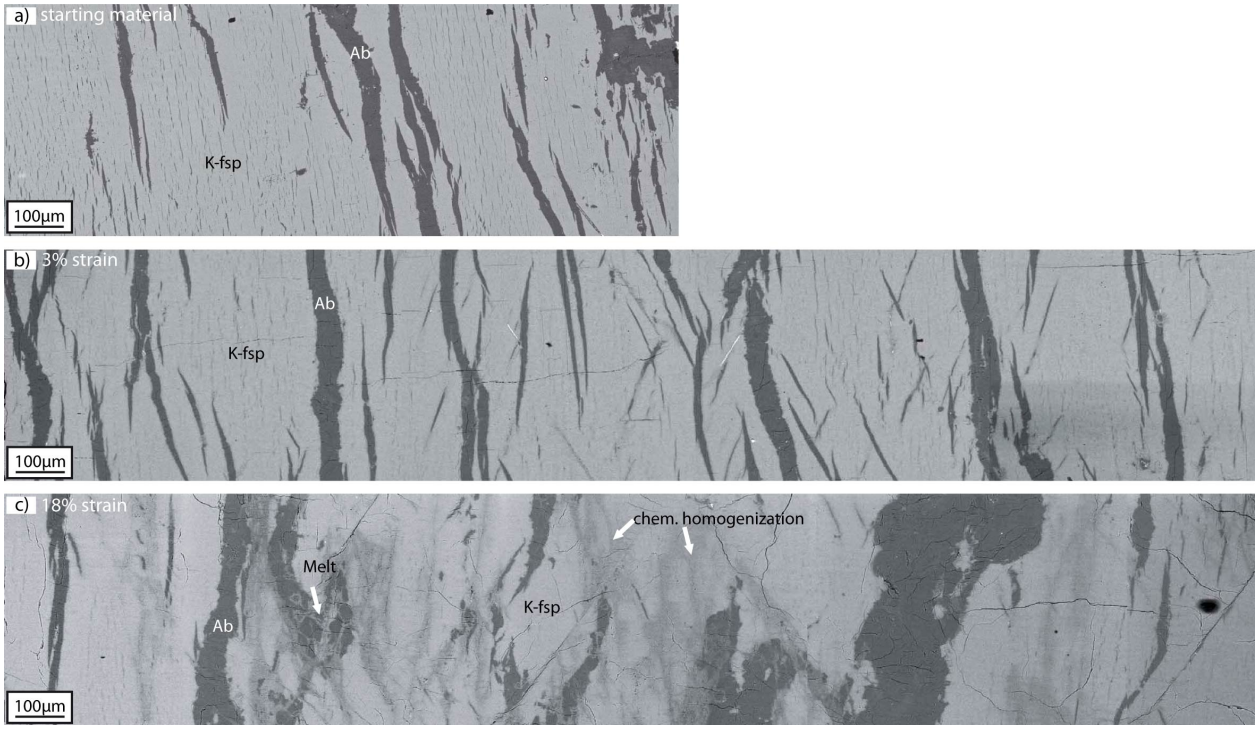

Fig. 4.12 SEM backscatter images showing the relationship between microstructure, melt formation, and strain. **(a)** Pink

K-feldspar starting material. **(b)** Microstructure of axial compression experiment stopped at peak strength (mn294, 900 °C, 0.75 GPa, 3% strain). A few cracks are present in the central part of the sample, where little homogenization occurred. No melt was detected at this strain. **(c)** Microstructure of axial compression experiment (mn295) at 900 °C, 0.75 GPa, 18% strain. The sample shows pervasive fracturing and related chemical homogenization. Melt pockets are present in homogenized regions and along shear cracks

Chemical homogenization of solid material

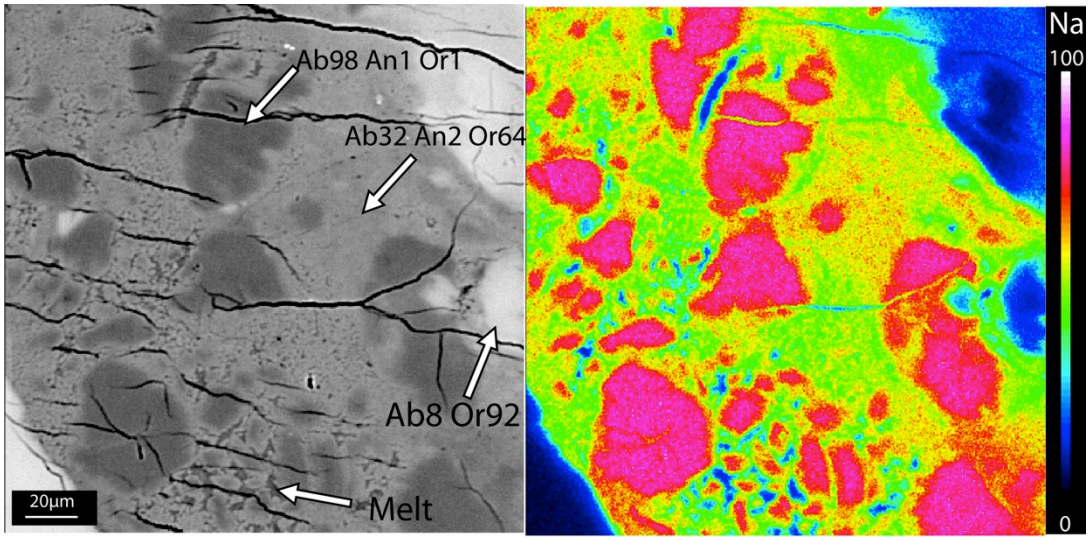

Fig. 4.13 Chemical analysis of a gouge formed in a high strain sample (mn222, 900 °C, 1.0 GPa). **(a)** Backscatter electron image. Note that chemical homogenization ($Ab_{32}An_2Or_{64}$) occurs in the fine-grained matrix, whereas the larger fragments maintain the original albitic composition of $Ab_{98}An_1Or_1$. The surrounding intact material is Orthoclase (Ab_8Or_{92}). **(b)** The EPMA element distribution map of Na shows inhomogeneous composition of the chemical homogenized matrix, which is represent in the yellow-greenish color. The small blue regions in the middle of the gouge represent melt pockets. The albitic fragments with a high Na- content are shown in pink**.**

Deformed samples contain chemically homogenized zones (Figs. 4.7a,b,e, Fig 4.13c) which are found exclusively in fractured regions (Fig. 4.6c,d). The chemically homogenized zones are found either in gouges formed along shear fractures (Fig. 4.13), as symmetric rims (up to 90 μm wide) surrounding fractures (Fig. 4.6e,f) or locally as overgrowths sealing old fractures. As shown in Figure 4.14 the orientation of chemically homogenized zones broadly corresponds to the orientation of the conjugate fractures, confirming the close link between cracking and chemical homogenization.

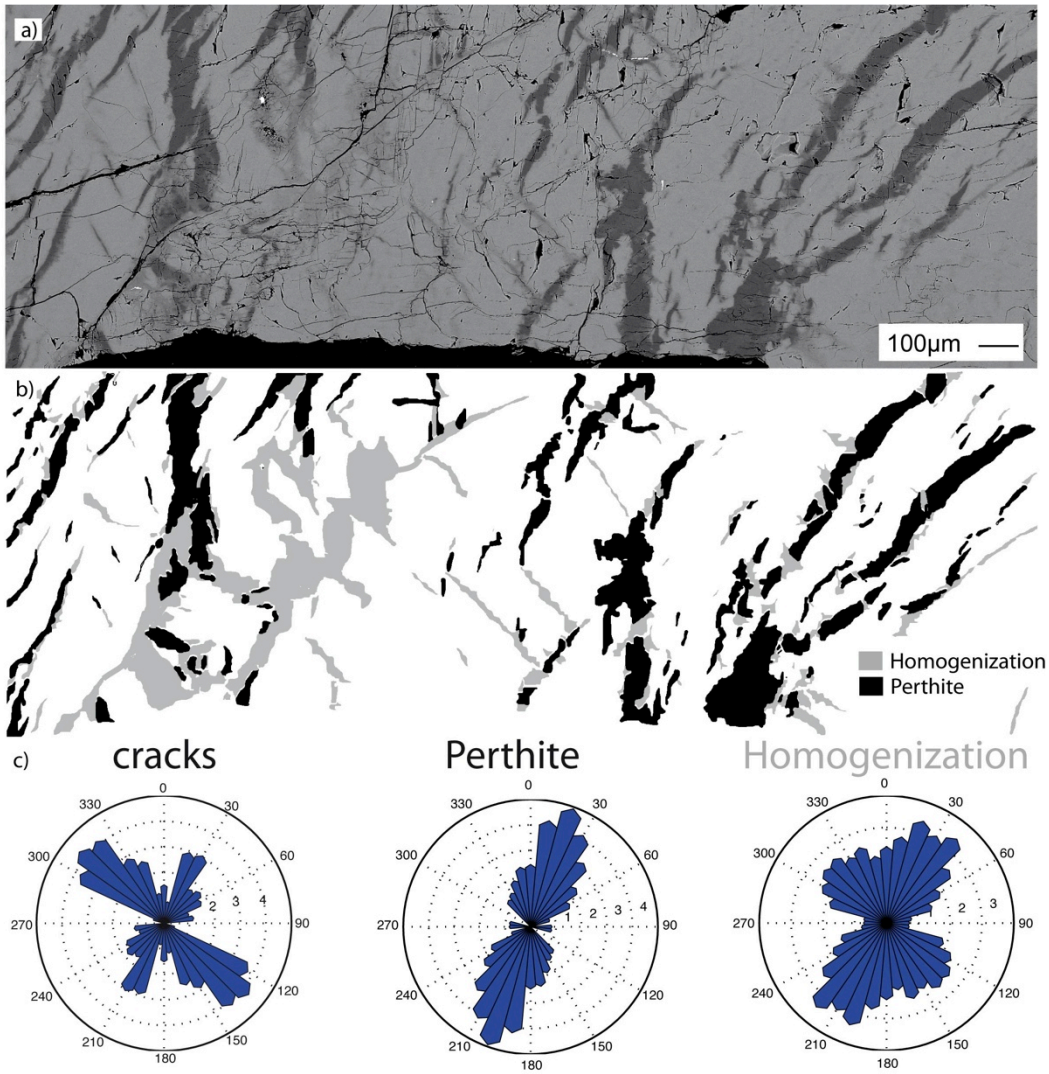

Fig. 4.14 Relationship between cracks and chemical homogenization in sample mn250 deformed at 900 °C, 1.5 GPa. Compression direction vertical. **(a)** SEM backscatter image. Three phases are visible: K-feldspar matrix (light grey), albitic lamellae lamellae (dark grey) and chemical homogenized region (intermediate grey). **(b)** Grey level slicing of the BSEM images created with Image SXM showing the distribution of the albitic lamellae and the chemical homogenized regions. **(c)** Rose diagram showing the orientation relationship between cracks, albitic lamellae and homogenize zone respect to the compression direction (vertical)

Chemical distribution maps (Fig. 4.13), EPMA measurements, and BSE images show well-defined transitions (over less than 5 μm distance) between the chemically homogenized regions and the surrounding undisturbed K-feldspar starting material. The composition of the chemically homogenized zones varies from $Ab_{10}Or_{90}$ to $Ab_{83}Or_{17}$ (Fig. 4.8) and suggests that compositional changes arise from differential mixing of the Or-rich matrix ($Ab_8An_0Or_{92}$) with the albite lamellae ($Ab_{98}An_1Or_1$) present in the starting material. However by means of SEM it was impossible to

resolve individual fragments in zones subjected to chemical compositional changes (Figs. 4.6e,f, 4.7a,b) (on the contrary, in non-homogenized gouge even submicron-sized fragments are clearly identified, Fig. 4.6b). In order to better characterize the chemically homogenized regions we attempted EBSD measurements in such zones. It was possible to acquire and index individual EBSD patterns, indicating the crystalline nature of the material. However, it was not possible to identify regions with the same orientation larger than a few points (at a step size of 1 μm), so it is likely that these zones consist of extremely fine grained material with a grain size that cannot be resolved by our EBSD technique.

In powder experiments held at hydrostatic conditions (900 °C, 1.0 GPa) for 34 h, homogenization is extensive in the whole sample, producing a completely homogenized (none of the crystal fragments show the original composition) groundmass with a composition of $Ab_{22}An_{1}Or_{77}$ (Fig. 4.12).

4.4.2.3 Hydrostatically heated samples

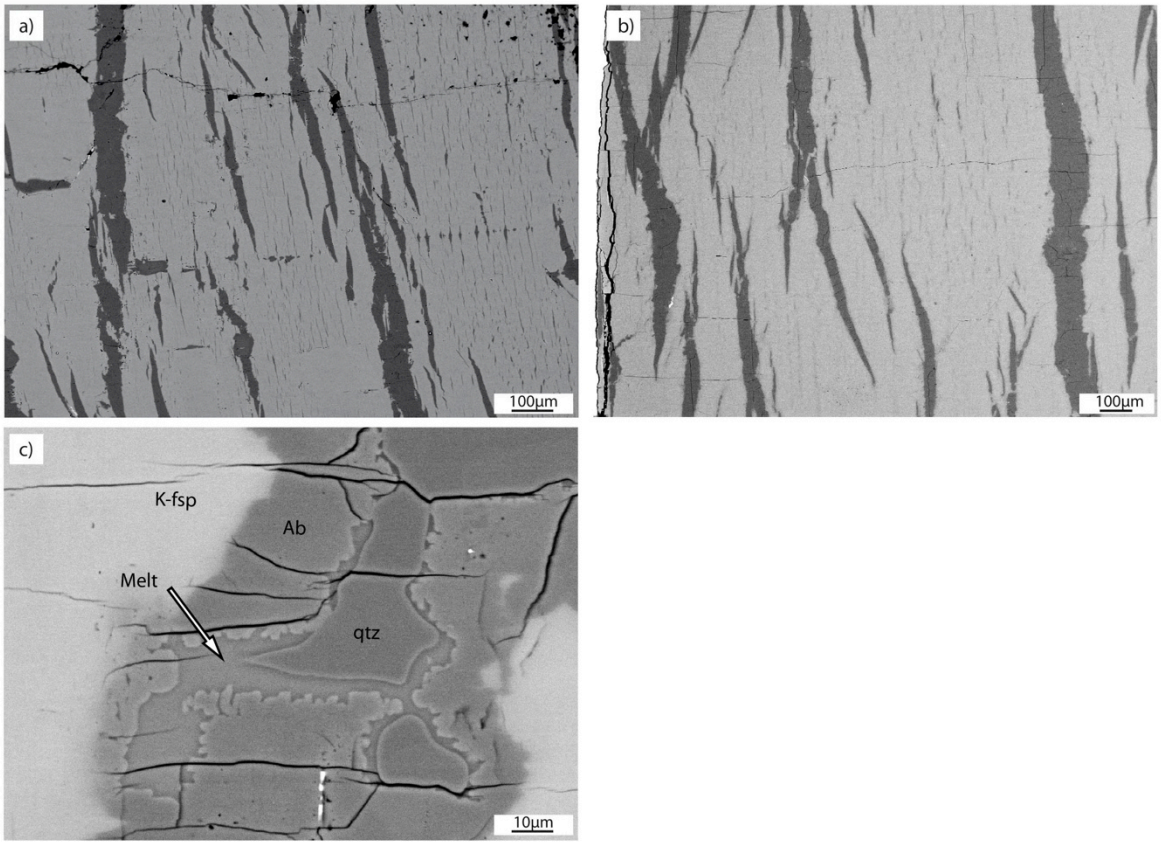

Fig. 4.15 SEM backscatter image (BSE) showing the microstructure of the hydrostatic experiment (sample mn271) kept

at 900 °C and 1.0 GPa for 71 hours. **(a)** Backscatter image of the starting material (pink K-feldspar). **(b)** Microstructure of the hydrostatic experiment. Comparison between starting material (a) and hydrostatic experiment (b) shows no substantial changes. Albitic lamellae and matrix do not show any chemical homogenization and no shear cracks were formed. **(c)** Melt formation in the hydrostatic experiment was observed only around quartz grains present in the albitic lamellae. The melt film forms a homogeneous rim all around the quartz crystal.

Hydrostatic experiments (Fig. 4.15) were performed in order to distinguish between microstructures formed during pressurization and heating and those produced by deformation. In hydrostatic experiments cracking is rare and only present at the border regions of the sample, producing small axial fractures with no displacement. A few isolated fractures are found close to mica inclusions. These fractures are oriented at ~35° to the {100} direction, corresponding to the orientation of the mica flakes in the starting material.

Compositional changes are almost absent in comparison to deformed samples. Some chemical homogenization seams are present along the fractures in the vicinity of mica, but no homogenization occurs between albite and K-feldspar. Even the thinnest albite lamellae (1-10 μm) are undisturbed and maintain the same appearance and characteristics as the lamellae in the starting material (Fig. 4.15a,b). Melt is present only as thin films around quartz inclusions in some albite lamellae (Fig. 4.15c).

4.5 Discussion

4. 5.1 Starting materials

Both starting materials show similar values of peak and flow stress, and similar trends in mechanical behavior. In addition, the microstructures that developed during deformation were essentially identical. Therefore, we suggest that the behavior of the deformed samples is representative of the general behavior of natural perthitic K-feldspar at high pressures and temperatures.

The amount of water in the samples determined by loss of ignition is 0.1 - 0.2 wt%. Considering analytical errors, as well as break down of the mica in the deformed samples and some structurally bound H_2O, we assume a slightly higher (0.2 - 0.3 wt%) water content in the samples

during deformation. This indicates that the starting material is not water saturated. A further indication of water undersaturation in the starting material is the lower (10 wt%) water content measured in the quenched melt of the hydrostatic sample with respect to the H_2O content (16 wt%) for water-saturated K-feldspar of the same composition determined by Holtz et al. (1995).

The starting materials contain small mica needles preferentially oriented along the cleavage planes {110} and distributed inhomogeneously throughout the crystals. Microstructural analysis suggests that the preferred orientation of mica may control the location of some of the fractures. A variable mica content between samples may explain some of the scattering in the mechanical data registered during the deformation experiments.

4.5.2 Mechanical data and microstructures

The stress-strain curves for samples deformed at 700 °C show trends typical of brittle deformation: peak strength approximately or slightly higher than confining pressure values and a positive dependence of peak stress on confining pressure. Brittle deformation as the dominant deformation mechanism at 700 °C is also supported by microstructural observations that show extensive cracking of the samples, the formation of shear and conjugate fractures, and grain size reduction to produce gouges. In addition, EPMA analyses indicate that neither the starting materials nor the small gouge fragments undergo chemical changes during deformation.

At 900 °C deformation was also mainly accommodated along brittle structures such as shear-cracks and systematically oriented arrays of fractures. However, the mechanical data show an inverse dependence of flow stress on confining pressure, differential stresses far below the Goetze criterion, and low friction coefficients on fractures oriented at ~50° to the compression direction (μ= 0.1-0.2 for experiments at Pc of 1.0 GPa -1.5 GPa). These observations suggest that along fractures deformation was not controlled entirely by brittle processes. Previous deformation experiments performed on anorthosite by Tullis and Yund (1992, 1991) suggested that at 900 °C and 1.0 GPa feldspars deform mainly by dislocation creep. However, our deformed samples do not show microstructural evidence for dislocation glide or dynamic recrystallization. Instead, the samples deformed here contain widespread evidence for melting associated with brittle fracturing, and chemical homogenization in extensively fractured regions. The role of these two processes in the deformation behavior of feldspars is discussed below.

4.5.3 K-Feldspar melting in water bearing systems

Thermodynamic models predict that for perthitic K-feldspar (system Ab-Or-H_2O, 0.2 wt%-0.3 wt% H_20) at high confining pressures (1.0 GPa) melting will commence at temperatures between 788 - 850 °C (Ebadi and Johannes 1991). This is in agreement with our experiments: samples deformed below the solidus temperature (700 °C and 1.0 GPa) show no melt formation. At 900 °C (1.0 GPa), ~ 50-110 °C above the solidus temperature, melting is expected and confirmed by the presence of melt in all deformed samples. Microstructural observations indicate that in deformed samples melt is formed only along cracks and in fault gouges, whereas the undeformed parts of the samples are melt free. Also in the hydrostatically heated single crystal (1.0 GPa and 900 °C), where neither cracks nor gouges are produced, no melt is formed. This indicates that intact material does not melt even at temperatures above the solidus, and that the melting process is kinetically controlled. Kinetically-induced variations of melt content in deformed samples have been reported previously by Misra et al. (2009), Molen and Paterson (1979) and Tumarkina et al. (2011).

The localized formation of melt along fractures can be explained by the fact that melting in feldspar involves an increase in volume. In the case of K-feldspar the volume increase is = 0.5192 J/Bar/mol ($V_{\text{solid material}}$ =10.8878 J/Bar/mol; V_{melt} =11.4070 J/Bar/mol; Holland and Powell 1998). At high confining pressures (such as in the experiments) melting is inhibited because of the lack of "free space", and thus the impossibility of accommodating volume expansion. This is the case of the hydrostatic experiments. On the contrary, during deformation significant cracking and shear fracturing result in local dilation allowing the K-feldspar material to melt and expand. Thus, in the experiments the melting process at high temperatures (above the solidus) is promoted by dilatational effects caused by deformation (see also van der Molen and Paterson 1979; Tumarkina et al. 2011).

The strong feedback between cracking and melting is highlighted by the microstructures observed in the perthitic K-feldspar samples deformed at confining pressures of 0.75 GPa. Experiments stopped at peak strength (mn293, mn294) show only minor crack formation and therefore subordinate melting. During progressive deformation (mn258, mn295) larger and more continuous cracks are formed and a higher melt fraction is produced. On the contrary, in high-pressure experiments (1.5 GPa; mn297), the formation of discrete through-going fractures is initially prevented by the high confining pressure. Instead, deformation is accommodated by a large number of microcracks pervasively distributed throughout the warmer parts of the sample. The pervasive microcracking leads to significant and distributed dilatancy, which enhances the melting process at a relatively early stage of deformation.

4.5.4 Melt content and distribution

Pseudosection calculations (Fig. 4.10) predict a melt content of 4.8 vol% for water bearing perthitic K-feldspar deformed at 900 °C and 1.0 GPa. This is in good agreement with the melt content determined in the hydrostatically heated K-feldspar powder (~5-6 vol %; mn267). In the deformed single crystal samples the exact amount of melt was more difficult to quantify, but it is almost certainly less than that in the powder experiment. This is because the amount of melt in the powder experiment is expected to represent the highest possible melt fraction at a given set of conditions, as melting is favored by the increase in reaction area in fine-grained aggregates (Greenwood and Hess 1998).

The presence of a relatively small melt fraction in the deformed single crystals is supported by the relatively high flow stresses (values comparable to deformed single crystals of feldspar in absence of melt, e.g., Stünitz et al. 2003) during deformation, which indicates that the bulk stress of the samples was supported by the solid framework, and suggests that during deformation grain interfaces and fracturing were largely controlling the behavior of the sample rather than the presence of melt. As demonstrated in deformation experiments by Bruhn et al. (2000) a small melt fraction does not induce the breakdown of the solid framework since the melt remains isolated in pockets. On the contrary, at melt fractions > 0.07 melt migration and segregation occur leading to pronounced weakening (Rosenberg and Handy 2005; Vigneresse et al. 1996). In our experiments isolation of the melts, even in the highest strain experiments, is suggested by the highly variable and inhomogeneous melt compositions found in the melt pockets.

In the deformed K-feldspar samples melt was distributed along fractures and in pockets oriented at ~50° to the axial shortening direction (σ_1). Our observations are in good agreement with observation of naturally deformed rocks (e.g., Brown and Solar 1998; Weinberg 1999; Weinberg 1996). However previous experimental works by Ave'Lallemant and Carter (1970), Dell'Angelo and Tullis (1988), and Rutter and Neumann (1995) indicate that melt was collected into pockets oriented dominantly parallel to the main shortening direction (σ_1). Our results suggest therefore a strong relationship between cracking and melt formation: cracks were initially formed at 30-60° to the compression direction and this was followed by enhanced local melting.

4.5.5 Dissolution-precipitation processes in K-feldspar

As discussed above, the deformation of K-feldspars at high pressures and temperatures in our experiments occurred mainly by brittle processes associated with partial melting. However, the presence of chemically homogenized zones surrounding fractures and the formation and growth of new crystals within and around melt pockets suggests the operation of dissolution-precipitation processes during deformation.

Chemically homogenized regions are clearly related to the cracking process, and are found around small fractures and melt pockets. Chemical homogenization is also evident in the fine-grained gouge fragments formed in shear fractures, and is extensive in the powder experiments where the entire material shows a homogeneous intermediate composition ($Ab_{22}An_1Or_{77}$). Due to the fact that compositional changes of the material are more pronounced in extensively fractured regions and gouges, where grain size reduction occurred and where melt is present, we suggest that homogenization occurs by dissolution-precipitation processes, where the presence of melt enhances the process by increasing the transport rate along grains (Cooper and Kohlstedt 1984; Hirth and Kohlstedt 2003; Kohlstedt and Zimmerman 1996; Pharr and Ashby 1983; Raj 1982; Tullis and Yund 1996). The activity of dissolution-precipitation processes in the deformed samples is consistent with the presence of overgrowths and grain bridges on the microscopic fragments of melt-bearing gouges (on the contrary melt free gouges show fragments with sharp and well defined boundaries), and the sealing of fractures by homogenized material.

Previous hydrostatic experiments at 1000 °C and 1.5 GPa conducted by Brady and Yund (1983) and Christoffersen et al. (1983) showed compositional changes in K-feldspar due to the interdiffusion of K and Na. They found that after 6 days an interdiffusion rate (D^-) of 10^{-13} cm^2/sec produced a homogenized rim of around 7 μm at the boundaries between the K-feldspar matrix and albite lamellae. However, in our experiments the homogenized zones can be much wider (up to 90 μm) and are not found at the albitic lamellae-K-feldspar contacts but always in relation to brittle fractures. In our experiments, even the very thin stringlet-type albite lamellae remained intact in the less deformed parts of the samples, without any signs of chemical homogenization along their boundaries. We suggest, therefore, that in deformed K-feldspar samples brittle cracking, which triggers the melting process, also favors dissolution-precipitation processes over interdiffusion.

The nucleation and growth of new euhedral crystals and the formation of growth rims around relict gouge particles adjacent to melt pockets are further examples of the activity of dissolution - precipitation processes in the samples. As described by Putnis (1992), the formation and growth of new grains by precipitation processes often produces crystals with a chemical composition different

to that of the parent, explaining the intermediate, chemically homogenized composition measured in all new grains.

The EBSD data lend further support to the interpretation of dissolution-precipitation creep being the dominant deformation mechanism in the fine-grained K-feldspar gouges and the zones of chemical homogenization. Numerical models have suggested that anisotropic dissolution and growth rates during diffusion creep can result in a crystallographic preferred orientation, in which the crystallographic direction of faster dissolution/growth ends up aligned with the instantaneous stretching axis during viscous flow (Bons and Den Brok 2000). In light of this, the alignment of the [010] planes of newly-grown crystals with the shear band boundaries, and of the (100) axes with the shear direction can be explained as a shape fabric achieved by oriented growth during diffusion creep. The (100) axis of K-feldspar has been interpreted as the direction of faster growth during anisotropic dissolution and precipitation in a number of studies (Menegon et al. 2013; Menegon et al. 2008). Likewise, anisotropic dissolution and precipitation has been invoked as a CPO-forming mechanism for other minerals (clinopyroxene: Godard and Van Roermund, 1995; quartz: Takeshita and Hara, 1998); albite: Heidelbach et al., 2000; amphibole: Pearce et al., 2011).

4.5.6 Melt-related weakening

Many experimental studies (e.g., Arzi 1978; Dell'Angelo and Tullis 1988; Holyoke and Rushmer 2002) have documented dramatic weakening when melt is formed in the system. In our experiments, weakening caused by the presence of melt along fractures is most evident in samples deformed at relatively low confining pressures (mn295, mn258 deformed at 0.75 GPa, 900 °C). Those samples show relatively high peak strength values (600-680 MPa) after 3-5 % strain, where microstructural observations show that almost no melt was formed. During deformation, fracturing occurred and melt was progressively formed, leading to weakening down to 55-70 % of peak strength (330 – 480 MPa). On the other hand, samples deformed at higher confining pressures (mn250, mn276, mn296 deformed at 1.5 GPa, 900 °C) and containing melt after small strains showed no well-defined peak stress. Instead, steady flow stresses of ~330 MPa were attained following yielding.

We speculate that the relative weakness of samples deformed at higher pressures is related, in addition to the different distribution and geometry of cracking and related melt formation, also to the lower viscosity of the melt formed along fractures. As postulated by Burnham and Jahns (1962), Day and Fenn (1982), Goranson (1936, 1938) and Kadik and Lebedev (1968) the amount of water that

can be dissolved in the melt phase is pressure dependent. At higher pressures water solubility strongly increases with increasing pressure (e.g., Holtz et al. 1995; McMillan 1994; McMillan and Holloway 1987; Paillat et al. 1992). For silicate melts (system Qz-Ab-Or-H_2O) Holtz et al. (1995) observed an increase of water content from 9.9 wt% at 0.5 GPa to 16 wt% at 1.0 GPa. Huang and Wyllie (1975) measured (for the same system) a water content of ca. 21 wt% at 2.0 GPa.

In a hydrostatic experiment performed at 1.0 GPa and 900 °C, however, we determined a water content of ~10 wt%, around 6 wt% lower than the value predicted by Holtz et al. (1995). This anomalously low water content may arise for several reasons, including the analytical difficulty of determining H_2O-contents in melts (see Behrens et al. 2001; Johannes and Holtz 1996), the difficulty of preserving H_2O loss during and before analyses (Behrens 1995; Holtz et al. 1995) and/or by the locally lower pressures surrounding the melt phase (due to dilatancy along fractures as discussed above). In accordance with the discussion in the previous paragraph we assume an increase in the dissolved water content of the melt in samples deformed at 1.5 GPa compared to the samples deformed at 0.75 GPa. As postulated by Dingwell et al. (1996), Goranson (1931) and Shaw (1972) the addition of few weight %H_2O to a melt can lead to a drastic (several orders of magnitude) decrease of the melt viscosity. We suggest therefore that the relative weakness of the perthitic K-feldspar samples deformed at higher confining pressure is related to the relatively low viscosity of the melt phase formed following brittle fracturing.

4.6 Conclusions

Deformation experiments conducted with a solid medium deformation apparatus on perthitic K-feldspar single crystals at high pressures (0.75 -1.5 GPa) and temperatures (700 °C and 900 °C) suggest that:

1. At 700 °C deformation of K-feldspar is accommodated entirely by brittle shear fracturing.
2. Samples heated hydrostatically at 900 °C do not show any evidence of partial melting or chemical homogenization even although the temperatures were far above the solidus.
3. Deformation experiments at 900 °C are dominated by the simultaneous formation of micro-fractures and melt. At high confining pressure brittle deformation initiates by pervasive microcracking. The resulting fracture dilatancy favors melt formation along fractures and in fault gouges produced during subsequent shearing. The relatively high flow stresses during

deformation suggest a low and poorly-interconnected melt fraction of less than 6 %, consistent with microstructural and chemical analyses that show isolated melt pockets of variable composition. Melt along fractures accommodates displacement by viscous processes, thus at 900 °C the fractures have to be considered as a partly viscous system. Chemical homogenization surrounding fractures and in fault gouges, and growth of new grains in the melt, are suggested to occur by dissolution precipitation processes. The role of dissolution-precipitation processes in the deformation of fine-grained feldspar gouges is explored further in Chapter 5.

CHAPTER 5

Deformation mechanisms and chemical compositional changes in melt bearing feldspar gouges: An experimental study

5.1 Abstract

Previous experiments conducted on K-feldspar single crystals (Chapter 4) showed localization of deformation into melt bearing, fine-grained gouges formed along new shear fractures. The intention of this work is to simulate and study the deformation processes occurring in the melt-bearing gouges by performing shear experiments on fine grained feldspar aggregates, both in the presence and absence of melt. The deformation experiments were conducted on feldspar aggregates of different chemical composition (K-feldspar, albite and labradorite) at temperatures ranging from 700 °C - 900 °C, confining pressure of 1.0 GPa, and shear strains up to $\gamma \sim 6$. Aggregates of K-feldspar (composed of 80% Orthoclase and 20% Albite) deformed at T> 800 °C contain melt, whereas pure albite and labradorite aggregates are melt-free up to 900 °C.

Microstructural observations supported by mechanical data suggest the activity of viscous deformation processes in all examined samples. The presence of (1) regions showing chemical compositional changes, (2) the nucleation and growth of new euhedral grains with different chemical composition, and (3) grains with lobate and indented grain boundaries indicate that in feldspar gouges at high pressure and temperature deformation is mostly accommodated by dissolution – precipitation enhanced diffusion creep. The presence of melt in the samples enhances the transport properties of the material and the dissolution and precipitation process but does not dramatically affect the material rheology: no systematic strength differences were observed between melt-free and melt-bearing samples. This indicates that at a relatively low melt fraction (<0.06; from image analysis of melt-bearing samples) the sample strength is controlled by the solid gouge material. The

orientation of melt-bearing regions, preferentially concentrated in bands oriented at ~30°-40° to the shear zone boundaries, suggests melt segregation during deformation, possibly accompanied by local enhancement of melt formation due to decreasing confining pressure (dilatancy) in the shear bands.

5.2 Introduction

The mineral feldspar accounts for approximately 60 wt% of igneous and metamorphic rocks, and is therefore one of the major mineral constituents of the crust. The understanding of its deformation behavior is crucial for determining the rheology of the continental crust and, more generally, in understanding the evolution and dynamics of the Earth. However, because of the complex crystallographic structure of feldspar, its refractory nature and large compositional variation, its deformation behavior is still not fully understood.

Previous experimental deformation studies of feldspar aggregates have documented a regime of brittle faulting at low pressure and /or temperature (Tullis and Yund 1992, 1987). At temperatures of 300 °C - 600 °C and confining pressures (Pc) of 1.0 -1.5 GPa Tullis and Yund (1987) describe a regime of cataclastic flow. In this regime, coarse-grained (~500 μm starting grain size) anorthosite deforms by distributed cracking and no dislocation motions were observed (Tullis and Yund 1992). The existence of a broad regime of cataclastic flow in feldspar is caused by the relative ease of cracking along well-developed cleavage planes, and the difficulty of dislocation glide and climb (Tullis and Yund 1985).

At higher temperatures (600 °C – 900 °C; 1.0-1.5 GPa) microstructural observations indicate a transition from dominant microcracking to recrystallization-accommodated dislocation creep (Borg and Hear 1970; Hadizadeh and Tullis 1992; Kronenberg and Shelton 1980; Marshall and Mclaren 1977; Tullis and Yund 1987, 1985, 1980, 1977). Tullis et al. (1990) observed in polycrystalline albite samples deformed at 900 °C (1.5 GPa; 10^{-6} s^{-1}) the formation of strain free and weakly recrystallized grains. They attributed the formation of new grains to grain boundary migration. Rybacki and Dresen (2000) reported the activity of dislocation glide, grain boundary migration and recrystallization in synthetic anorthite aggregates deformed at ~1000 °C and strain rates of 10^{-4} s^{-1}-10^{-5} s^{-1}. Stünitz and Tullis (2001) observed the activity of dislocation creep in dry plagioclase aggregates (An_{54} and An_{60}) deformed at 900 °C and 1.0 GPa.

However, in the experimental study presented in Chapter 4 on the deformation behavior of perthitic K-feldspar single crystals (700- 900 °C; 0.75-1.5 GPa) we did not observe any evidence for

dislocation creep. Instead, deformation was accommodated along brittle shear fractures, accompanied by the formation of fine-grained fault gouges and melt. Preliminary microstructural and chemical analyses of the gouges indicated the activity of diffusion creep by dissolution-precipitation, probably enhanced by the presence of melt in the system. The activity of diffusion creep in deformed feldspar has previously been reported by Barreiro et al. (2007), Dimanov et al. (2000), Dimanov et al. (1998), Ji and Mainprice (1986), Manning et al. (2008), Stünitz and Tullis (2001) and Tullis and Yund (1996, 1991). In these studies, the switch from dislocation creep to diffusion creep was caused by the presence of a small amount of water (0.1-0.4 wt%; Stünitz and Tullis 2001) or by the formation of melt in the system (Dimanov et al. 2000; Ji and Mainprice 1986). Tullis and Yund (1996) found that in Albite and Orthoclase aggregates deformed at 1.4 GPa and 900 °C (strain rate of 10 -5 s-1) a switch from dislocation creep to diffusion creep was accompanied by a significant decrease in strength.

The aim of this work is to further explore the deformation mechanisms and influence of melt within gouges formed during experimental deformation of K-feldspar at high pressure and temperature. Instead of using K-feldspar single crystals as in Chapter 4, this chapter presents experimental work performed on layers of fine-grained synthetic feldspar aggregates deformed in shear, therefore simulating deformation processes occurring in the fault gouges. Three different starting materials (perthitic K-feldspar, pure albite, pure labradorite) were chosen in order to compare the strength and deformation behavior in both melt-free and melt-bearing gouges.

5.3 Methods

5.3.1 Starting materials

Ten experiments were performed on synthetic fault gouges derived from three different species of feldspar (Table 1): (1) perthitic K-feldspar (six experiments), (2) albite (two experiments), (3) labradorite (two experiments).

(1) The K-feldspar gouge material was obtained from the same single crystal used in previous experiments (Chapter 4). The pegmatitic crystal consists of 84% Or-rich matrix ($Ab_6An_0Or_{94}$) and 15% albite exsolution lamellae ($Ab_{98}An_{1.5}Or_{0.5}$) (Table 5.1). Small quartz grains (0.2 %) are randomly distributed within the exsolution lamellae. White mica (0.5 %) is present as thin needles oriented parallel to the {110} cleavage planes of the feldspar. The water content (in the form of fluid inclusions, structurally bound H_2O and some absorbed H_2O) was determined

as ~0.1 -0.2 wt% by the loss of ignition method on a sample heated to 1000 °C for 2 h. Polysynthetic twinning is pervasively and homogeneously distributed throughout the whole K-feldspar matrix.

(2) The Albite gouge was obtained from a metasomatic igneous rock of Vannøya, Northern Norway. The mafic to intermediate igneous protolith was strongly affected by a CO_2 rich fluid, which led to the breakdown of the Fe–Mg–bearing silicates and Fe–Ti oxides and the transformation of all primary plagioclase into albite (Priyatkina et al. 2011). The rock consists of 98 % albite with a chemical composition of $Ab_{98-99}An_0Or_{1-2}$ (Table 5.1), <1 % hematite and 1-2 % residual plagioclase with a composition of $Ab_{63}An_{36}Or_1$. The water content of the intact rock was determined as 0.1 wt%. For further information on the albite starting material we refer to Priyatkina et al. (2011).

(3) The gem quality labradorite powder was extracted from a volcanic olivine basalt of Sonora, Mexico (Gutmann and Martin 1976). The colorless single crystals, which can be several cm long, contain no impurities and are completely transparent. The composition was determined by Stünitz and Tullis (2001) as $Ab_{38}An_{60}Or_2$ (Table 5.1). Loss of ignition suggests that the single crystals contain no intracrystalline water.

Phase	K-feldspar		Albite	Labradorite
(wt%)	Matrix	Lamellae		
SiO_2	64.74	67.65	67.40	53.01
Al_2O_3	18.71	19.77	19.40	29.83
FeO	0.00	0.00	0.13	0.36
CaO	0.00	0.36	0.25	12.49
Na_2O	0.68	11.73	12.00	4.30
MgO	0.00	0.00	0.04	0.00
K_2O	15.70	0.08	0.06	0.30
MnO	0.06	0.00	0.01	0.00
TiO_2	0.00	0.00	0.48	0.00
Total	99.90	99.59	99.77	100.29
Ab%	6	98	98	38
An%	0	1.5	1.5	60
Or%	94	0.5	0.5	2

Table 5.1 Chemical compositions of the three starting materials. Measurements are given in wt.%. Labradorite composition from Stünitz and Tullis (2001)

The feldspar powders contain intracrystalline H_2O as well as absorbed water. The intracrystalline water determined by loss of ignition is reported above, whereas the absorbed water in a fine grained (10-20 μm grain size, see below) powder is expected to be ~ 0.1 wt% (Stünitz and Tullis 2001; Tullis and Yund 1991). Therefore, the water contents in our deformed feldspar powders are approcimately 0.1 wt% H_20 in the labradorite, 0.2 wt% H_20 in the albite, and 0.3 wt% H_20 in the perthitic K-feldspar.

5.3.2 Sample preparation and experimental procedures

All experiments were conducted with a modified Griggs type solid medium deformation apparatus (Tullis and Tullis 1986) on powdered (gouge) material. Sample powders were prepared by grounding the intact crystals in an alumina mortar. The separation of different grain size fractions was performed by sieving the ground rock through a series of filter papers. After the separation process the powder was air-dried in an oven at 110 °C for at least 24 hours.

For the sample preparation, 0.1 g of dried powder was sandwiched between two alumina forcing blocks pre-cut at 45°. Almost all of the experiments reported here were performed on powder with a grain size of 11-20 μm. One experiment (mn344) was performed on a mixture of 70 % 11-20 μm grain size fraction and 30 % 80-100 μm grain size fraction. The powder samples and forcing blocks were wrapped in a 0.025 mm thick Nickel foil and inserted into a can-shaped Pt-jacked. The Pt-jacket was welded using a Lampert welding apparatus. The sample was then placed between two alumina pistons in the center of a graphite furnace. NaCl was used as confining medium for all the experiments. The experimental temperature was monitored with Pt-Pt10%Rh S-type-thermocouples placed in the center of the samples at the contact with the Pt-jacket. A schematic representation of the sample assembly is given in Fig. 5.1.

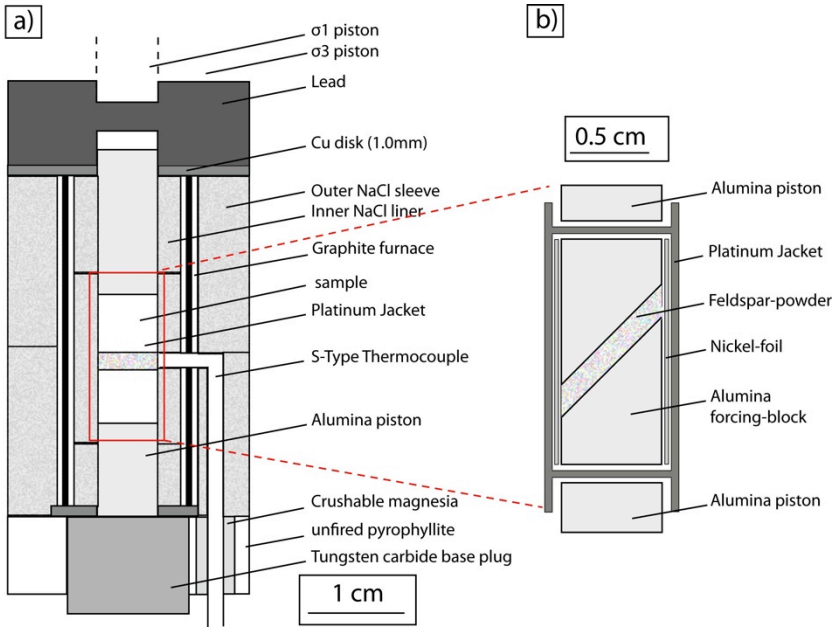

Fig. 5.1 Schematic representation of the **(a)** assembly inside the pressure vessel and **(b)** sample geometry used in this study. Modified after (Tarantola et al. 2010).

The samples were taken to desired P,T-conditions in approximately 6 h by sequentially increasing the pressure and temperature (T increase =25 °C/min). Prior to deformation all the samples except two (mn269 and mn270) were hydrostatically hot-pressed for 41-50 h in order to decrease the porosity of the starting gouge material. Samples mn269 and mn270 were hot pressed at 1000 °C and 1.5 GPa for 50 h and 36 h, respectively, and afterwards pressure and temperature were decreased slowly until the desired deformation conditions were reached.

After hot-pressing the samples were deformed by advancing the σ_1 piston at a constant strain rate of ~10^{-6} s^{-1}. At the end of the deformation process the motor was stopped and the temperature was immediately decreased (quenched) to 200 °C in <2 min. Subsequently, confining pressure and axial load were simultaneously and slowly reduced to atmospheric conditions in order to minimize the formation of unloading fractures.

Experimental data (confining pressure, force, displacement, temperature) were digitally recorded in 1.0 sec intervals and evaluated using the MATLAB program "RIG" (http://sites.google.com/site/rigprogram/). The recorded data were corrected for apparatus compliance, internal friction of the instrument, and changes in thickness and diameter of the samples. For the strain calculations an initial shear zone thickness of 0.7 mm was used. This thickness was determined from microstructural images of a hydrostatically hot pressed but unsheared sample. For further information regarding processing of the mechanical data see Pec et al. (2011). Table 5.2 lists the details of the experiments described in this study.

Sample name	Experiment type	Starting material	Grain size [μm]	Pc [GPa]	T [°C]	Mean Shear rate [x$10^{-5}s^{-1}$]	Hot – pressing [h]	Deformation [h]	Total time [h] at p,T	Strain [%]
mn267	Hydrost.	K-Fsp	11-20	1.00	900	0.0	34	0	34	0.0
mn269	Shear	K-Fsp	11-20	1.00	900	3.3	76	18	126	3.5
mn270	Shear	Albite	11-20	1.00	900	6.3	41	17	65	4.0
mn272	Shear	K-Fsp	11-20	1.00	900	6.9	44	19	74	4.3
mn341	Shear	K-Fsp	11-20	1.00	800	3.2	44	25	92	3.0
mn342	Shear	K-Fsp	11-20	1.00	700	2.5	44	30	92	2.6
mn343	Shear	Albite	11-20	1.00	900	2.3	50	30	113	2.6
mn344	Hydrost.	K-Fsp	11-100	1.00	900	0.0	48	0	48	0.0
mn345	Shear	Labradorit	11-20	1.00	800	2.3	48	34	120	2.8
mn346	Shear	Labradorit	11-20	1.00	900	1.9	48	24	113	0.9

Table 5.2 Summary of deformation conditions of all performed experiments (Pc= Confining pressure, T= Temperature).

5.3.3 Analytical methods

Standard petrographic polished thin-sections were prepared by cutting the samples parallel to the compression direction and normal to the shear displacement in the gouge layers. Carbon coated samples were studied in backscatter mode using a field emission Zeiss Sigma FE-SEM at the University of Tromsø. The images were taken at a beam current of 15 nA and an acceleration voltage of 15 kV. In all images presented in this chapter the shear zone boundaries are horizontally oriented and the shear sense is dextral. Angles measured counterclockwise from the horizontal will be called "antithetic", whereas angles measured clockwise will be called "synthetic". The compression direction (σ_1) in all images is oriented antithetically at 45° to the shear zone boundaries.

Quantitative element analyses were performed with a JEOL Superprobe 8200x (University of Copenhagen) at 15 kV and 20 nA using a spot size of 5 μm. For the determination of the melt composition a low beam current of 10-12 nA, a spot-size of 10-12 μm, and counting time <10 sec was used, in order to avoid significant Na-loss. The melt fraction and distribution were estimated from SEM images processed with ImageSXM (www.liv.ac.uk/~sdb/ImageSXM/) as well as a number of macros developed by Renee Heilbronner (http://pages.unibas.ch/earth/micro/index.html).

5.4 Results

5.4.1 Melting in feldspar systems

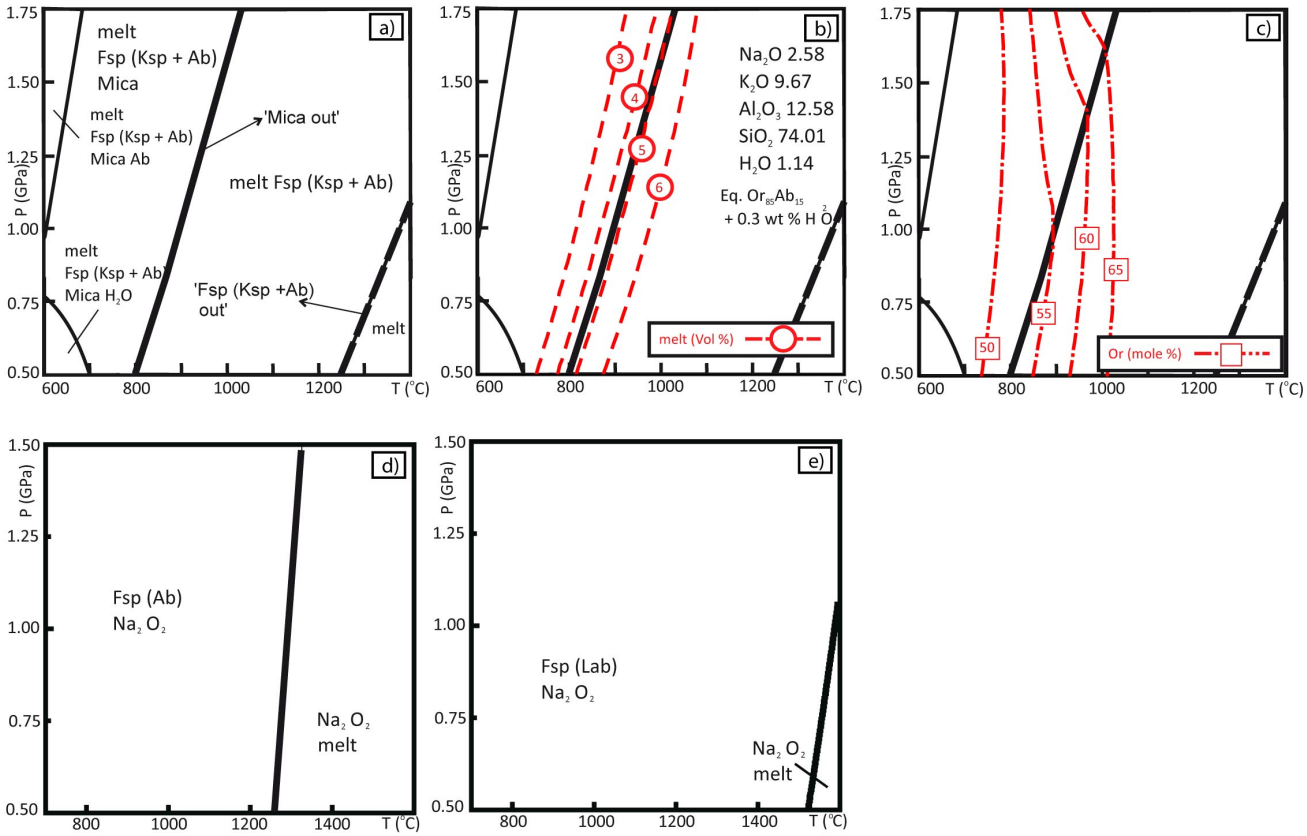

Fig.5.2 P-T Pseudosections for the investigated feldspar systems. Mineral abbreviations: Fsp= Feldspar, Ksp= K-feldspar, Ab= Albite, Lab= Labradorite (a-c) Calculations for the K-feldspar system. Molar ratios of element oxides are given in the right side of part (b). **(a)** Assemblage stability fields showing melt formation at temperatures >600 °C. **(b)** Isopleths showing the increase of melt fraction (Vol%) with increasing temperature. **(c)** Contours of moles of Orthoclase (Or) in the melt indicate that orthoclase is consumed with increasing temperature. Contours numbers are in mole fraction. **(d)** Assemblage stability fields for albite. Melt formation occurs at T > 1230 °C. **(e)** Assemblage stability fields for labradorite showing melt formation at T > 1540 °C.

Thermodynamic models (Fig 5.2) for the 3 starting materials used in this work were calculated by using the program package PerpleX_07 (Connolly 2009). The following solution models were used for the pseudosection calculations (refer to the solution_model.dat file for details): mica (Coggon and Holland 2002), melt (Holland and Powell 1998), sanidine (Waldbaum and Thompson 1969) ternary feldspar (Fuhrman and Lindsley 1988). The CORK model (Holland and Powell 1998) was used as fluid equation of state for H_2O.

For the K-feldspar powders, where 0.3 wt% H_2O is present, melting is expected to commence at temperatures <600 °C (Fig 5.2a). With increasing temperature (Confining Pressure, Pc, constant) the melt content increases and at 900 °C and 1.0 GPa the expected melt content is ~5 vol% (Fig. 5.2b). The melt composition at 900 °C and 1.0 GPa is expected to be ~Or_{55} (Fig. 5.2c). During the melt-forming reaction, the single-phase feldspar solid changes to a composition of $Ab_{20}Or_{80}$.

In the modeled system, which contains 0.5% white mica, the melt reactions are more complex than in simple alkali feldspars systems, because of the stability range of the mica. At 1.0 GPa confining pressure the white mica breaks down just below 900 °C, shifting the solidus temperatures of the system towards lower temperatures due to the release of water during the mica breakdown reaction.

Thermodynamic models for albite containing 0.2 wt% H_2O (Fig. 5.2d) and for pure labradorite containing 0.1 wt % absorbed water (Fig. 5.2e) predict at a confining pressure of 1.0 GPa melting will commence at 1270 °C and 1580 °C, respectively. Therefore at the deformation conditions investigated here no partial melting is expected in either the albite or labradorite samples.

5.4.2 Hydrostatically heated K-feldspar sample

The K-feldspar powder (grain fraction 11-20 μm; mn267) held at hydrostatic conditions at P = 1.0 GPa and T = 900 °C for 34 hours contains ~5.6 vol% melt (Fig. 5.3). Most of the melt, which has a chemical composition of $Ab_{34}An_5Or_{61}$, is collected in a large melt pool ~ 1.5 mm long and up to 80 μm wide at the upper border of the sample, and in numerous smaller (up to 100 μm) melt pools randomly distributed in the gouge material (Fig. 5.3a, b). Minor amounts of melt are confined at grain triple junctions (interstitially) and locally form thin melt films around the feldspar gouge fragments (Fig. 5.3b,c). The melt pools commonly contain small spherical bubbles with a diameter of 2-4 μm, which form by the exsolution of a fluid phase from the melt fraction during the quenching process (Behrens et al. 2001) (Fig. 5.3c). EMPA analyses indicate ~10 wt% fluid (probably in the form of H_2O) in the melt. The solid gouge material consists mainly of euhedral grains (Fig. 5.3b,c) with sizes between 5 - 30 μm. As some grains are larger than the maximum dimension of the starting material we assume that grain growth occurred during the experimental process. Chemical analyses reveal a relatively homogenous composition for the feldspar grains of ~$Ab_{20}An_0Or_{80}$ (Fig. 5.3c). None of the grains show the original composition measured in the starting material ($Ab_6An_0Or_{94}$ for the K-feldspar fragments and $Ab_{98}An_{1.5}Or_{0.5}$ for the albite fragments). A compositional change from

the original composition to a more intermediate composition (~ $Ab_{20}An_0Or_{80}$) is referred to in this study as "chemical homogenization".

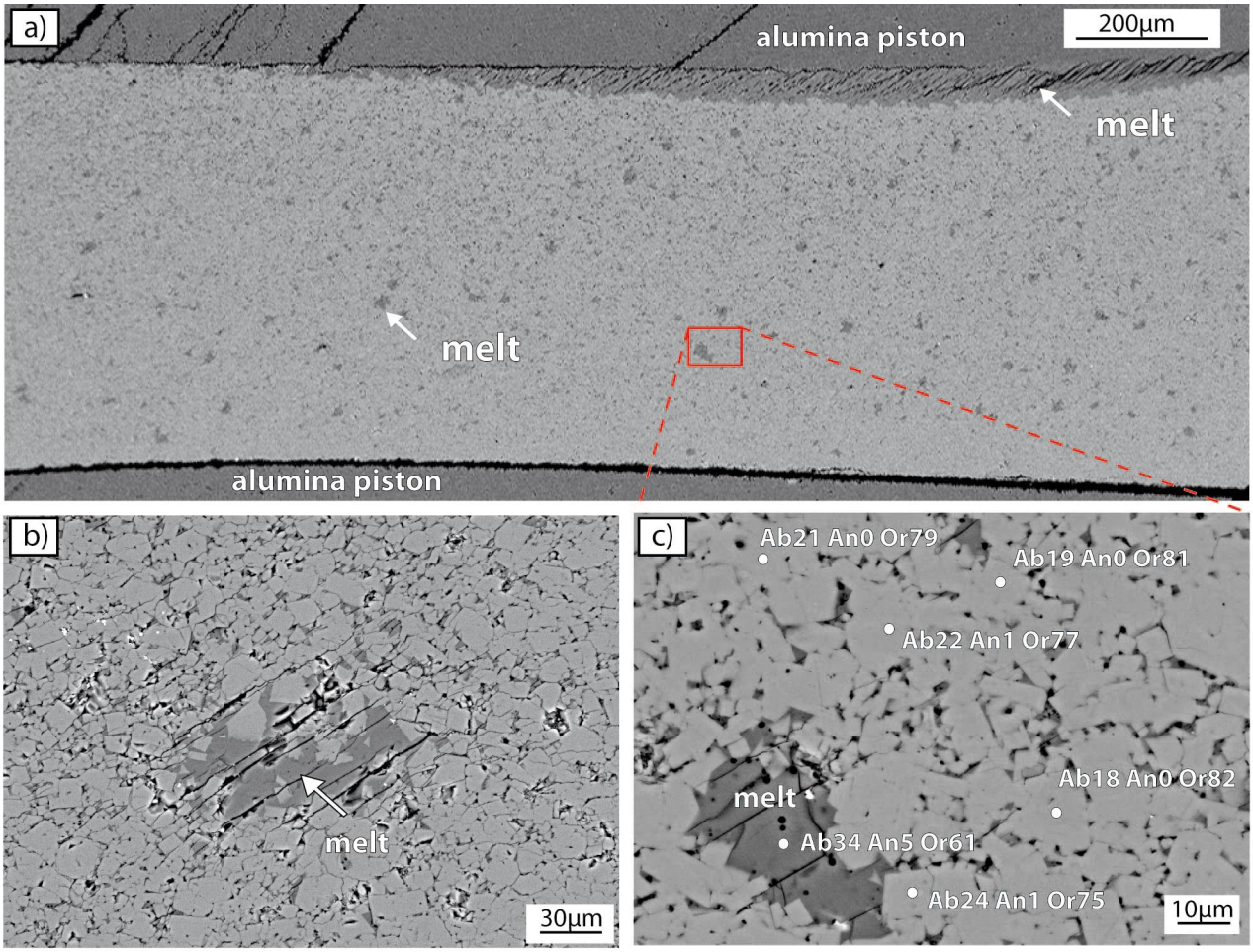

Fig.5.3 Microstructures of the hydrostatically heated (900 °C, 1.0 GPa) K-feldspar powder (mn267). **(a)** SEM-Backscatter image showing the melt distribution in the gouge layer. Melt is recognizable by the darker contrast, and is mainly collected in an elongate melt lens at the gouge-piston contact. **(b)** Microstructures around a melt pool. Melt is collected in large melt pools and locally is present along grain boundaries. The melt pool contains a high density of unloading cracks formed during depressurization of the sample after deformation. **(c)** Melt pool containing small spherical bubbles formed by the exsolution of a fluid phase from the melt fraction during the quenching process (Behrens et al. 2001). The solid material has a chemically homogenized composition of ~$Ab_{18\text{-}22}An_{0\text{-}1}Or_{75\text{-}81}$.

In a hydrostatic experiment (mn344; Fig. 5.4) performed on K-feldspar powder composed of mixed grain sizes (70 wt% with sizes of 11-20 μm, 30 wt% with sizes of 80-100 μm) the internal parts of the large grains do not show any chemical homogenization and maintain their original composition (Fig. 5.4a). In some grains the perthitic structure (albite lamellae alternating with Or-

matrix) is still preserved (Fig. 5.4b). On the other hand, the finer-grained fraction shows complete homogenization and overgrowths along grain boundaries. Melt in this experiment is present in randomly distributed pools (Fig. 5.4a) and as thin melt films surrounding the small homogenized grains. Locally, at the edges of large melt pools, grains with euhedral shapes, straight grain boundaries and chemically homogenized compositions are observed (Fig. 5.4a).

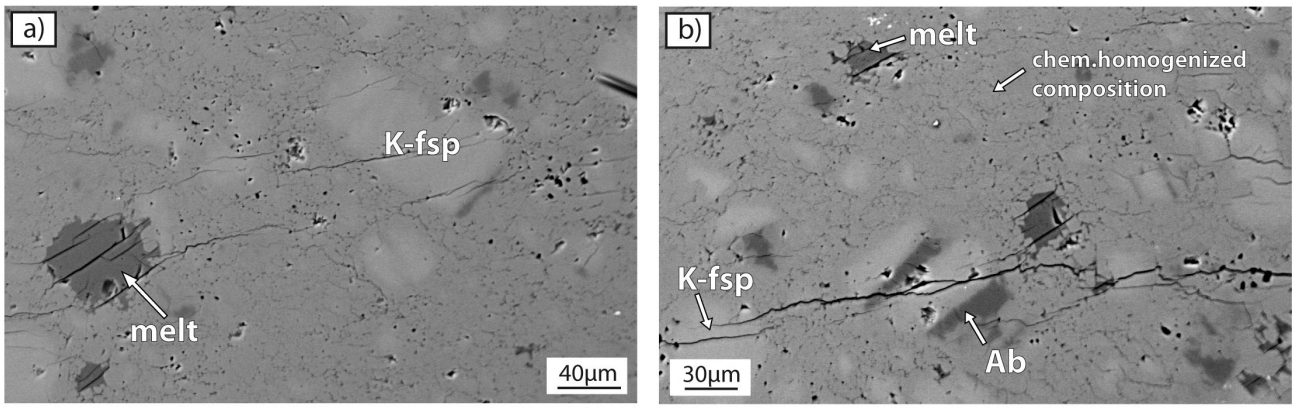

Fig.5.4 Microstructures of hydrostatically heated (900 °C, 1.0 GPa) K-feldspar powder containing different grain size fractions (mn344). **(a)** SEM- Backscatter image showing no chemical compositional changes in the cores of the larger K-feldspar grains (light grey colour). On the other hand the fine-grained fraction is completely homogenized and overgrowth structures are common around grain boundaries. **(b)** Larger K-feldspar grains retain unchanged perthitic structures in their cores. Melt pools are randomly distributed within the fine grained and chemically homogenized matrix.

5.4.3 Deformed K-feldspar samples

K-feldspar powder was deformed at 700, 800 and 900 °C (confining pressure 1.0 GPa).

The mechanical data (Fig. 5.5) show a general decrease of flow stress with increasing temperature. The sample deformed at 700 °C (mn342) shows a well-defined peak stress of ~ 350 MPa followed by pronounced weakening to reach 180 MPa after a shear strain of $\gamma \sim 3$. The sample deformed at 800 °C (mn341) shows a peak strength of 180 MPa followed by the onset of steady state flow at 160 MPa after a $\gamma \sim 2$. At 900 °C, samples reach steady state flow stresses of 100-150 MPa after $\gamma \sim 2$, followed by some strain hardening.

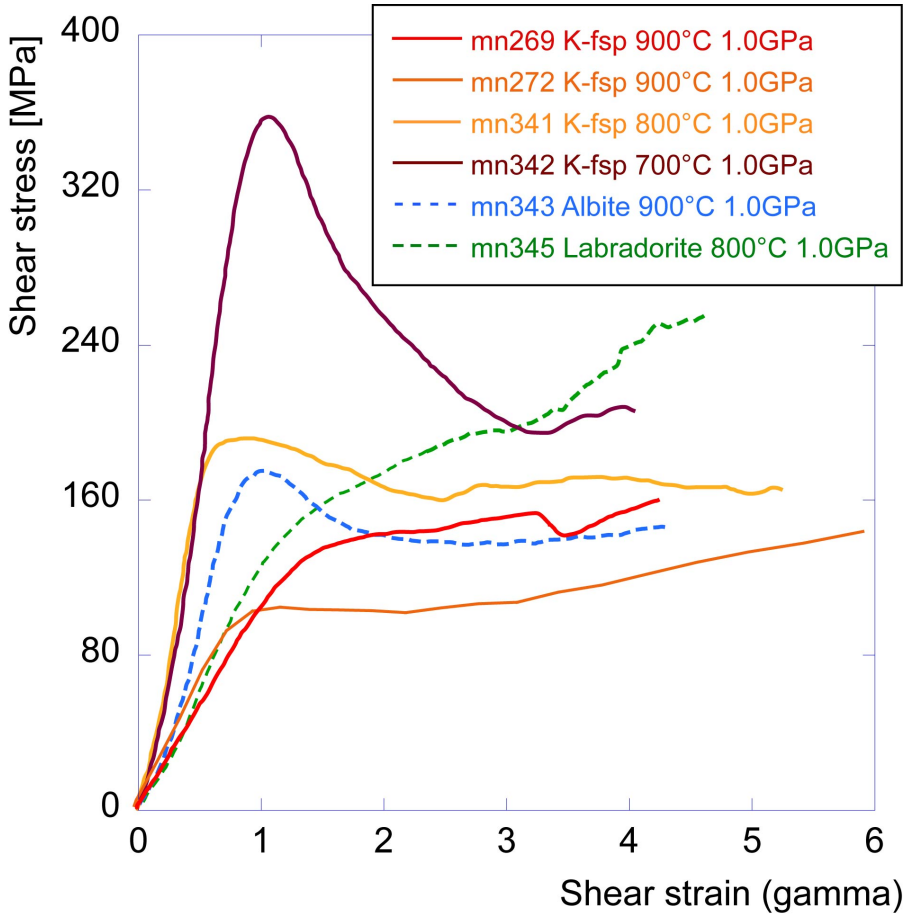

Fig.5.5 Shear strain vs. shear stress curves for the deformed feldspar samples. K-feldspar sample are represented in orange-red-brown color, albite sample is represented in blue and labradorite sample is represented in green.

Microstructural observations reveal no melt in the K-feldspar sample deformed at 700 °C (mn342) (Fig. 5.6). The sample shows the development of domains in which the gouge material is extensively crushed down to a grain size of a few μm, forming a chemically homogenized, very fine-grained matrix (Fig. 5.6a,b). A few larger grains (with original chemical composition, both K-feldspar and albite) with well preserved albite lamellae are present in the finely crushed matrix (Fig. 5.6b). The orientation of the fine grained domains defines, at the edges of the sample, a weak foliation oriented sub-parallel to the shear zone boundary (c-planes, Fig. 5.6c), whereas in the central part of the sample the anastomosing fine grained domains are generally oriented at ~15 ° (antithetically) to the shear plane (S-planes, Fig. 5.6d). Locally, fine grained bands form at 160° (antithetically) to the shear zone boundary (Fig. 6) leading to the development of a S-C-C' fabric geometry (following the nomenclature of Berthé et al. 1979). The large surviving grains of orthoclase in the fine grained matrix are sometimes associated with tails of fine-grained material and form delta-type clasts (Passchier and Trouw 1996). Albite fragments occasionally develop sigma-type clasts (Fig 6c; Passchier and Trouw 1996). In less deformed regions the gouge fragments, which are surrounded by a chemically homogenized matrix, show no shape-preferred orientation (Fig. 5.6b).

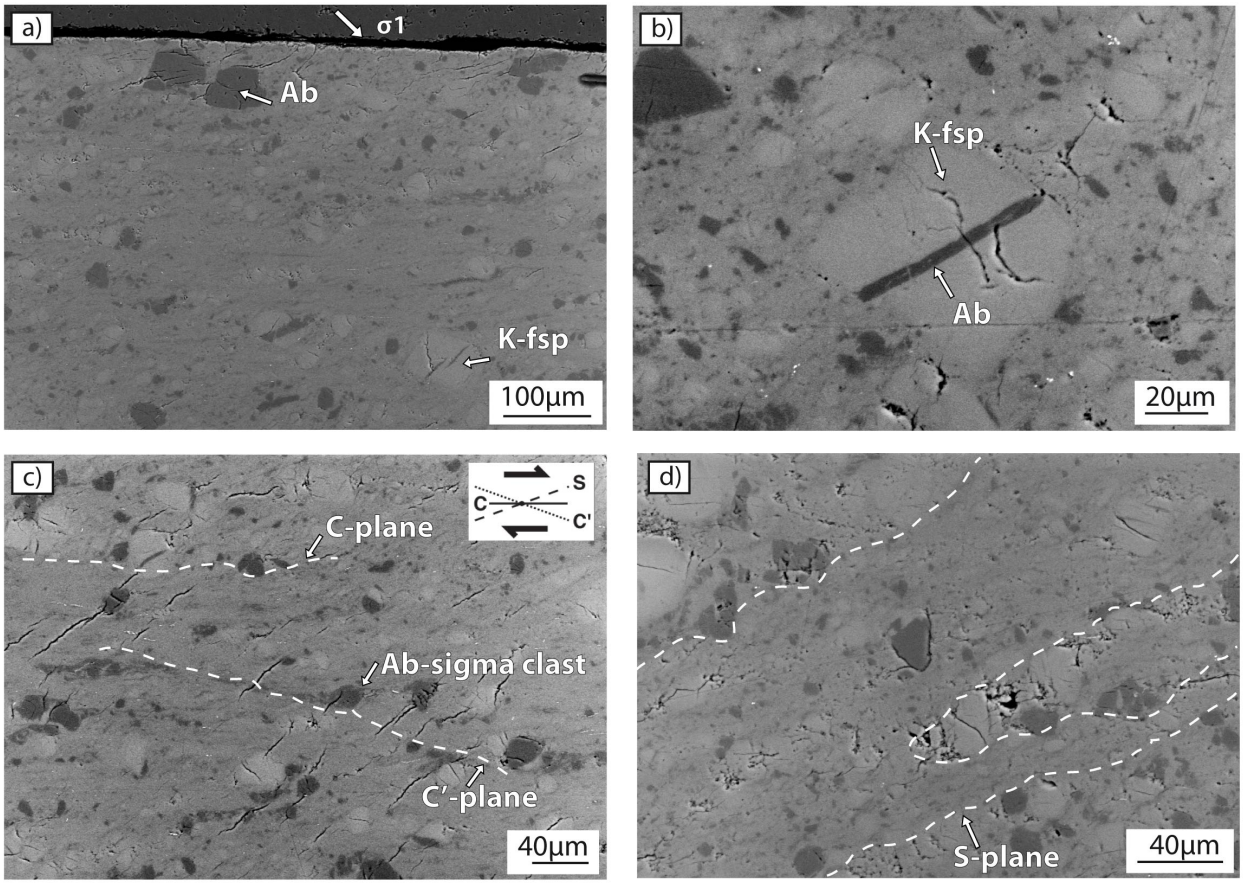

Fig.5.6 SEM-backscatter images of deformed sample mn342 (K-feldspar powder, 700 °C, 1.0 GPa). All images have a dextral sense of shear and the shear zone boundary is horizontal in all images. Compression direction (σ_1) is oriented at 135° to the shear zone boundary as indicated in part (a). Kfs= K-feldspar, Ab= Albite. **(a)** Development of fine-grained domains throughout the central part of the sample. **(b)** Larger grains, which show no preferential orientation and maintain their original composition, including perthitic structures with undisturbed boundaries. **(c)** Development of a weak foliation (C-type) oriented sub-parallel to the shear zone boundary and poorly-defined shear bands oriented at low angles to the shear zone boundary (C' type) in the peripheral part of the sample. Inset shows the geometry of shear zones after Berthé et al. (1979). **(d)** Formation of anastomosing fine grained domains oriented at ~ 15 ° (antithetically) to the shear zone boundary in the central part of the sample**.**

The K-feldspar sample (mn341, Fig. 5.7) deformed at 800 °C contains melt that is present as: 1) thin films wetting grain boundaries oriented predominantly subparallel to the compression direction (Fig 5.7a-c), and 2) locally as melt-laden bands 5-10 μm wide oriented at ~30 ° (synthetically) to the shear zone boundaries (Fig. 5.7a,b). Small melt pools, containing 5-20 μm sized euhedral feldspar grains with straight grain boundaries and chemically homogenized compositions are present along the melt bands (Fig. 5.7b,c). Melt-rich regions of the sample show relatively high

porosity (Fig. 5.7a) and a relatively high density of unloading cracks formed during depressurization of the quenched sample after deformation (Fig. 5.7c). Chemical homogenization is pervasive in the whole sample, however larger grains preserving the original composition are still present (Fig. 5.7a). These larger grains show diffusely homogenized grain boundaries, and local overgrowth structures between the single grains are observed. Backscatter SEM images show more pronounced chemical homogenization around melt-bearing bands compared to the regions between (Fig. 5.7a).

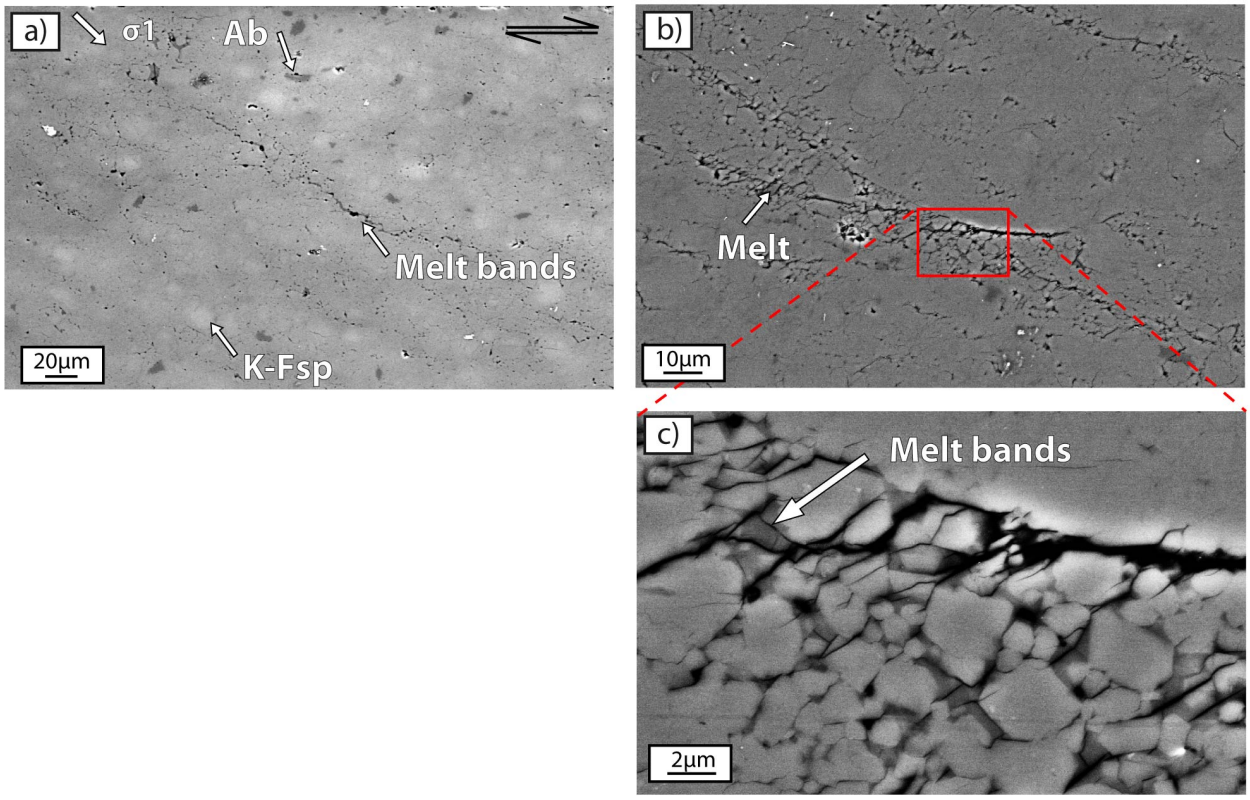

Fig.5.7 SEM-backscatter images of deformed sample mn341 (K-feldspar powder, 800 °C, 1.0 GPa). All images have a dextral sense of shear and the shear zone boundary is horizontal in all images. Compression direction (σ_1) is oriented at 135° to the shear zone boundary. Kfs= K-feldspar, Ab= Albite. **(a)** Chemical homogenization is pervasive throughout the sample. However, a few grains (with lighter grey color) showing the original chemical composition are still present. Melt is collected in thin melt-rich shear bands oriented subparallel to the compression direction. **(b)** Melt bands oriented at 30° (syntheticically) to the shear zone boundary. The surrounding solid material shows compositional changes, and overgrowth structures between individual grains are common. **(c)** Detail of (b) showing the formation of euhedral feldspar grains of different grain sizes around and within the melt pools.

At 900 °C the perthitic K-feldspar powders (mn269, mn272, Fig. 5.8) are completely homogenized. The entire material has a chemical composition of $Ab_{24\text{-}28}An_1Or_{71\text{-}75}$ and no grains with

the original composition were preserved (Fig. 5.8a). From a microstructural point of view, two different domains can be distinguished:

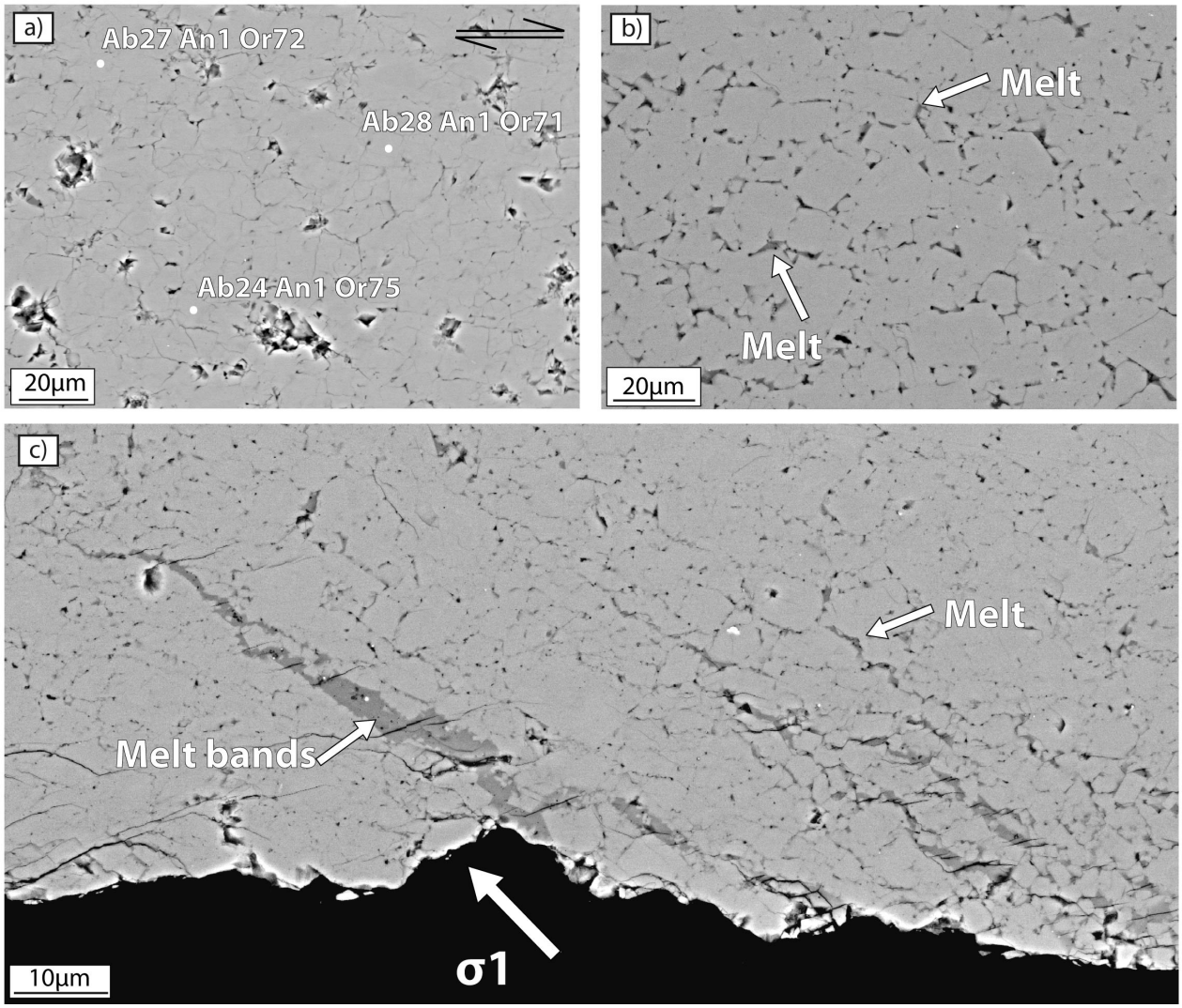

Fig.5.8 SEM-backscatter images of deformed samples mn269 and mn272 (K-feldspar powder, 900 °C, 1.0 GPa). All images have a dextral sense of shear and the shear zone boundary is horizontal in all images. Compression direction (σ_1) is oriented at 135° to the shear zone boundary. Kfs= K-feldspar, Ab= Albite. **(a)** Microstructures in the central part of the deformed gouge layer. The feldspar grains, which show a completely homogenized chemical composition of $Ab_{24\text{-}28}$ $An_1Or_{71\text{-}75}$, have indented grain boundaries and an interlocked microstructure. **(b)** Microstructure in the peripheral part of the sample. Melt is present at grain triple junctions and locally as a film wetting the grain boundaries. **(c)** Synthetic melt rich band in the central part of the sample. The melt bands reach lengths of 100 μm and are up to 10 μm wide.

1) The peripheral parts of the samples towards the ends of the gouge layers (Fig. 5.8b). These areas of the samples contain a local melt fraction of ~6-7 vol%. The melt is confined to grain triple junctions and locally is present as a film wetting the grain

boundaries (Fig. 5.8b). The solid grains in these regions consist of crystals with grain-sizes between 5 – 20 μm, straight grain boundaries and euhedral grain shapes.

2) The internal parts of the samples towards the middle of the gouge layers (Fig. 5.8c). In these areas, the melt is primarily collected along melt-rich bands oriented sub-parallel to the compression direction (at 35-40° synthetically to the shear plane). The melt bands reach lengths of 100 μm and are up to 10 μm wide. As visible in figure 5.8c, along some melt rich bands the solid grains, which show euhedral shapes and chemically homogenized compositions, loose interconnectivity (grain to grain contacts). Between the melt rich bands, melt free areas are also recognized (Fig. 5.8a). In these domains the solid grains consists of chemically homogenized feldspar crystals with tightly-interlocking and indented grain boundaries; no melt is visible in SEM images in between the single grains.

5.4.4 Deformed Albite samples

Albite samples deformed at 900 °C (mn270, mn343, Fig. 5.5) show peak strengths of 170 MPa followed by some weakening. After a shear strain of $\gamma \sim 1$ the samples deform by steady state flow at shear stresses of ~ 125 MPa.

In the deformed samples, neither chemical compositional changes nor melt are observed (Fig. 5.9a), and all of the grains maintain their original chemical composition. This includes a few plagioclase grains present in the starting material with a composition of $Ab_{63}An_{36}Or_1$ (Fig. 5.9a). The albite grains, which show an inhomogeneous grain size varying from 5 to 25 μm, are interlocked and their boundaries show indentation structures (Fig. 5.9b). This is most prominent along the grain boundaries oriented subparallel to the compression direction (Fig. 5.9b,c), along which porosity is also well developed leading to the formation of open grain boundaries (Fig. 5.9c). Locally the open grain boundaries coalesce to form short (~100 μm) fractures oriented at 40-50° (synthetically) to the shear zone boundaries. In the central parts of the deformed samples these short fractures act as connecting “bridges” for more continuous fractures that crosscut the gouge layer at an angle of 20-30° (synthetically; Fig. 5.9d).

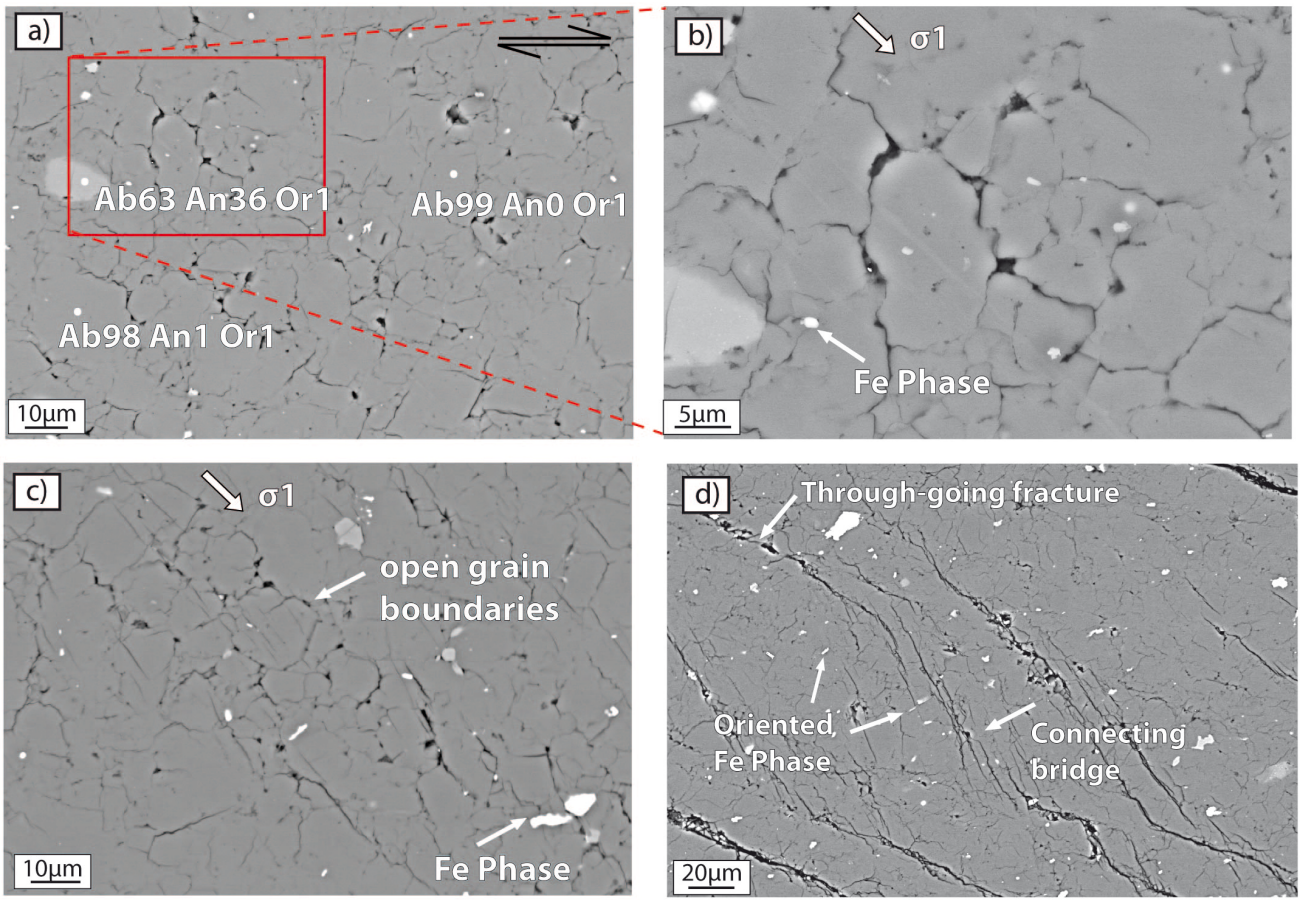

Fig.5.9 SEM-backscatter images of deformed sample mn343 (Albite powder, 900 °C, 1.0 GPa). All images have a dextral sense of shear and the shear zone boundary is horizontal in all images. Compression direction (σ_1) is oriented at 135° to the shear zone boundary. **(a)** EMPA chemical analyses of the deformed material. A few plagioclase grains with a composition of $Ab_{63}An_{36}Or_1$ are still present. All of the albite maintains its original chemical composition of $Ab_{99}An_0Or_1$. **(b)** Detailed picture of (a) showing the typical microstructure of the deformed sample. The albite grains are significantly interlocked and their boundaries show indentation structures. **(c)** Development of porosity and open grain boundaries oriented subparallel to the compression direction. **(d)** Formation of synthetic shear bands oriented at 40-50° to the shear zone boundary caused by the coalescence of the open grain boundaries. In some areas the shear bands act as connecting bridges between more continuous fractures oriented at 20-30° (synthetically) to the shear zone boundaries.

5.4.5 Deformed Labradorite sample

The pure Labradorite sample (mn345) deformed at 800 °C shows strain hardening during the entire experiment (Fig. 5.5). After a γ of around 1 the rate of hardening is relatively constant, and shear stress increases from 150 MPa after γ of 1 to 255 MPa after γ of 4.8.

Deformation is homogeneously distributed within the sample (Fig. 5.10) and no shear-bands or melt were observed. The deformed sample is composed primarily of a ground-mass of inter-grown labradorite grains (Fig. 5.10a). The larger grains (20 μm) shown in backscatter electron images are zoned (Fig. 5.10b): the labradoritic cores, which have well rounded edges, are surrounded by more albitic rims. The fact that newly formed rims have a different composition from the starting material suggests that crystallization involved nucleation and growth of plagioclase with a different (more albitic) composition.

Newly formed prismatic grains with lengths up to 20 μm are pervasively distributed throughout the deformed sample (Fig. 5.10b). The grains are oriented sub-parallel to the shear zone boundaries. Although microprobe analyses were not performed on these newly formed grains in this work, previous analyses by Stünitz and Tullis (2001), who worked with the same Sonoran labradorite starting material and similar deformation conditions, indicate that the new grains are zoisite.

Locally in the more albitic matrix, which formed between the starting labradorite grains, very small elongated grains of a newly-formed mineral are found (Fig. 5.10b). Due to their elongated shape and the small size (long axis <2 μm) no chemical analyses were possible. Stünitz and Tullis (2001) identified these grains as white mica and kyanite by SEM and TEM analyses.

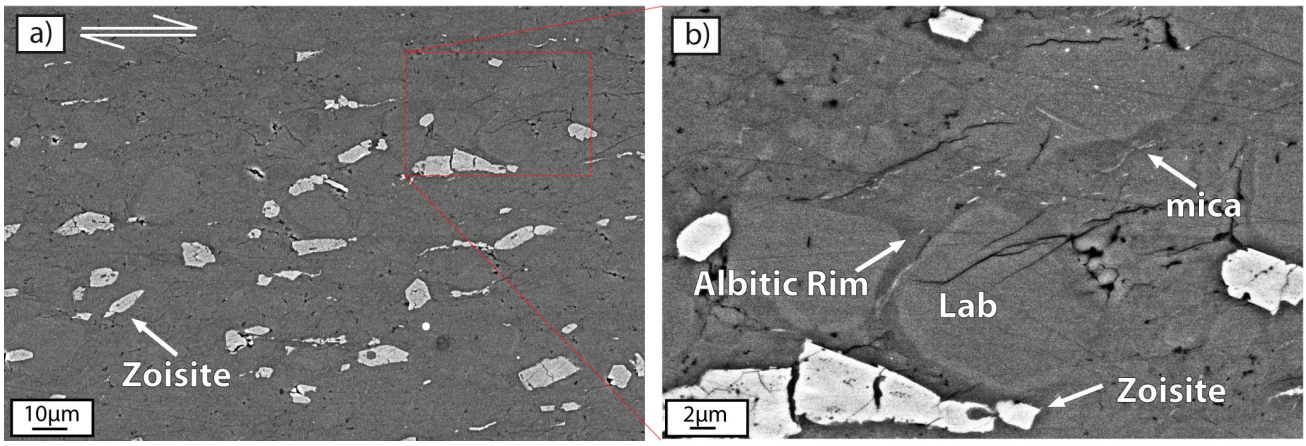

Fig.5.10 SEM-backscatter images of deformed sample mn345 (Sonora labradorite powder, 800 °C, 1.0 GPa). All images have a dextral sense of shear and the shear zone boundary is horizontal in all images. Compression direction (σ_1) is oriented at 135° to the shear zone boundary. **(a)** Deformation is homogeneously distributed within the gouge layer, with no evidence for the formation of melt or shear bands. **(b)** Detail of (a) showing a ground-mass of rounded labradorite grains surrounded by rims that are more albitic in composition. Newly formed prismatic zoisites up to 20 μm long are found throughout the entire gouge layer. Locally in the more albitic matrix very small grains of mica and kyanite are found.

5.5 Discussion

5.5.1 Melt formation in the system Ab-Or-An-H_2O

The onset of melting in the feldspar system Ab-Or-An-H_2O is dependent on the mineral chemical composition, on the water content of the material, and on pressure and temperature. For K-feldspar with a composition of 84 % $Ab_6An_0Or_{94}$, 15 % $Ab_{98}An_{1.5}Or_{0.5}$ ± Quartz and Mica, and a water content of 0.3 wt%, thermodynamic models predict melting to initiate at temperatures below 600 °C. Johannes and Holtz (1996) and Luth et al. (1964) postulated that melting would initiates at 675 °C for the system Ab-Or- H_2O at 1 GPa confining pressure. The lower solidus temperature obtained by the pseudosection calculation is attributed to the break down reaction of the mica. The mica break-down, which occurs at temperatures below 600 °C, releases water into the system and lowers the melting temperature. The fact that microstructural observations on our deformed samples indicates melt formation at T > 700°C (and therefore in better accordance with the experiments of Johannes and Holtz 1996 and Luth et al. 1964) suggest that the presence of the mica in the system does not affect the melting behavior of the k-feldspar samples. This is probably the case as mica breakdown can be kinetically inhibited in experiments and does not affect the melting behavior of the bulk system. The melt content (5-6 vol%), the melt composition ($Ab_{34}An_5Or_{61}$) and the composition of the solid material ($Ab_{22}An_1Or_{77}$) formed in the hydrostatic K-feldspar experiment are in good agreement with the predicted values of the thermodynamic models. Also, the increase of melt content with increasing temperature is in good agreement with the calculations.

Thermodynamic models for albite ($Ab_{98}An_0Or_2$; 0.2 wt% H_2O) and labradorite ($Ab_{38}An_{60}Or_2$; 0.1 wt% H_2O) predict melting to occur at temperatures far above the conditions investigated here. The thermodynamic calculations are confirmed by microstructural observations on the deformed samples, which reveal the absence of melt in both labradorite and albite samples.

5.5.2 Melt distribution

Microstructural observations reveal a significant difference in the distribution of melt in the deformed K-feldspar samples with respect to the hydrostatically heated samples, indicating that deformation significantly influences the melt distribution. In hydrostatic experiments melt is present mainly at grain triple junctions and locally collected into randomly distributed melt pools. Melt

confined to grain junctions in hydrostatically heated rocks is interpreted to result from the small (<50°) melt-solid dihedral angle of the feldspar material (e.g., Holness 2006, Kohlstedt 1992,Von Bargen and Waff 1986; Waff and Bulau 1982; Waff and Bulau 1979). In K-feldspar samples deformed at 800 °C melt is preferentially collected along grain boundaries oriented at a low angle to the compression direction. In experiments at 900 °C, which contain a higher melt fraction, the melt is segregated into synthetic melt-rich shear bands oriented at ~30° to the shear plane. Melt rearrangement during experimental deformation leading to the formation of melt rich bands has been extensively reported in a range of fine grained materials including mantle material (spinel lherzolite, olivine basalt; Bussod and Christie 1991; Daines and Kohlstedt 1997; Holtzman et al. 2003; Kohlstedt and Zimmerman 1996; Zimmerman et al. 1999;), crustal rocks (quartzite, anorthite; Dell'Angelo and Tullis 1988; Kanagawa et al. 2000; Rybacki et al. 2008) and synthetic materials (Norcamphor + benzamide melt; Rosenberg and Handy 2001).

Several models have been proposed for the rearrangement of melt in response to deviatoric stresses. Maaløe and Scheie (1982), McKenzie (1984), Richter and McKenzie (1984), Scott and Stevenson (1986) and Turcotte and Ahern (1978) proposed that melt segregation is driven by a solid-liquid density contrast, where the driving forces for the segregation are the spatial variations of shear stress and related gradients of mean pressure caused by the localized presence of melt. Cooper (1990) on the other hand observed melt migration driven by the gradient in applied stress. Melt segregation caused by gradients in mean stress associated with regional variations in viscosity have been described by Hall and Parmentier (2000), Holtzman et al. (2003a), Holtzman et al. (2003b), Kelemen and Dick (1995), Richardson et al. (1996), Stevenson (1989), Daines and Kohlstedt (1993), Riley and Kohlstedt (1991), Riley and Kohlstedt (1990 a,b) and Watson (1982). Further models proposed that melt migration was triggered by solubility gradients caused by dissolution reactions of minerals (Kelemen et al. 1995; Chadam et al. 1986).

In our experiments we suggest that melt segregation is driven by local stress gradients due to strain partitioning and formation of shear bands. The K-feldspar sample deformed at 700 °C (without melt formation) shows incipient strain localization and the development of fine-grained shear bands oriented at around 15° (both synthetically and antithetically) to the shear zone boundaries. In the albite samples (without melt formation) the development of shear bands is documented by the alignment of porosity and open grain boundaries. Similar microstructures have been reported by Rybacki et al. (2008) and Schmocker et al. (2003). The mechanism responsible for the initiation of the shear bands is not fully understood. However, it is generally accepted that shear bands are associated with local dilatancy and small shear displacements (e.g., Bésuelle 2001; Kohlstedt and

Holtzman 2009; Rudnicky and Rice 1975). A local drop in confining pressure (pressure gradient) is expected in such zones of dilatancy. Once melting initiates, the presence of pressure gradients in the sample promotes melt migration from "higher pressure" zones (e.g., in the matrix surrounding the shear bands) into "lower-pressure" zones (e.g., within the shear bands), leading to the formation of melt rich bands alternating with melt-free regions. Formation of dilatant bands where the fluid phase collects, and compaction bands in which the porosity is reduced and no fluid is present, has been modeled by Bésuelle (2001) and observed in experiments and natural outcrops by Antonellini and Aydin (1994) and Du Bernard et al. (2002).

In previous experiments on K-feldspar single crystals presented in Chapter 4, melt was found only along brittle cracks and in fault gouges. Microstructural observations suggested that melting was promoted by dilatancy effects. In the experiments on gouges reported here, the same K-feldspar starting material and the same deformation conditions were used as in Chapter 4, and it is therefore assumed that the same kinetic evolution is applicable (i.e melting favored by dilatancy). Following this, it can be expected that melt formation in the K-feldspar gouges will be favored along the shear bands where the volume increase occurring during the melting process can be accommodated. We thus suggest that in addition to melt segregation, where melt migrates from the surrounding layers into the shear bands, melt formation is directly enhanced along the shear bands due to dilatancy effects.

5.5.3 Viscous deformation in granular feldspar aggregates

The mechanical data show a general decrease in strength with increasing temperature. Combined with microstructural observations, this indicates the activity of viscous deformation mechanisms in all of the analyzed samples.

The deformed K-feldspar samples show chemical homogenization at all investigated temperatures. In samples deformed at 700 °C and 800 °C (Figs. 5.6, 5.7) pervasive chemical homogenization occurs in the finer grained gouge material associated with through-going (and melt-bearing at 800 °C) shear bands, whereas the cores of larger clasts maintain their original chemical composition. At 900 °C K-feldspar grains are completely homogenized (Fig. 5.8). The chemically homogenized compositions measured with EPMA ($Ab_{22}An_1Or_{77}$) correspond to the calculated equilibrium composition of the solid material ($Ab_{20}Or_{80}$).

Pervasive chemical homogenization in the K-feldspar samples is consistent with the activity of dissolution precipitation processes (e.g., Tullis and Yund 1991; Pec et al 2011). The activity of dissolution precipitation processes is supported by the nucleation and growth of new grains with compositions different to that of the starting material (Putnis 1992). The growth of new and chemically homogenous grains in the sample occurs mainly in melt-rich regions, and results in a microstructure characterized by original grains of 11-20 μm in size alternating with smaller, newly-grown euhedral grains. We interpret these new grains to have nucleated and grown during deformation. Grain growth by dissolution and precipitation, leading to a change in the sample grain size distribution, was reported by Cox and Paterson (1991) in fine quartz aggregates deformed at high temperature. They interpreted the change in sample grain size to occur both by the dissolution of the finest grains and precipitation of the dissolved material as overgrowths on the coarser grains. In our experiments, dissolution is documented by lobate and tightly interlocking (indented) grain boundaries of the feldspar grains present in melt free regions, where dissolution often occurs at grain-to-grain contacts. Precipitation of the dissolved material in melt-bearing regions is suggested by the straight grain boundaries and the euhedral shapes of the newly-grown and chemically distinct grains.

As the grain size of the starting K-feldspar gouge material was quite homogeneous (11-20 μm) we suggest that sites of dissolution and precipitation in the gouge layers were mainly controlled by strain partitioning and local variations in stress within the sample during deformation. For example, in melt-rich regions the nominal stresses are lower and this could promote local nucleation of new grains and precipitation of the feldspatic material which was previously dissolved in higher strain regions of the sample (e.g., Paterson 1978). Because chemical homogenization is observed at 700 °C in the K-feldspar gouges, where no melt was detected, we assume that the small amount of water in the starting material (up to ~0.3 wt%) was sufficient to promote dissolution-precipitation processes. This suggests that dissolution-precipitation processes were active at the beginning of our deformation experiments and are not directly initiated by the formation of melt in the system, although they were likely further promoted by the onset of melting. As postulated by Watson and Brenan (1987) the wetting angle in feldspar for aqueous fluids is <60°. Thus the addition of only a very small amount of aqueous fluid to the system would provide an interconnected network of high diffusivity channels and enhance grain boundary diffusion creep. The activity of diffusion creep promoted by only a small amount of fluid or melt has been reported for albite (Ji and Mainprice 1986), granite (Dell' Angelo et al. 1987) and olivine (Karato et al. 1986).

In the deformed albite samples open grain boundaries are oriented sub-parallel to the compression direction. Tullis and Yund (1991) and Heidelbach et al. (2000) observed similar microstructures in albite aggregates deformed at high pressure and temperature in the presence of fluid, and attributed the formation of such porosity to dissolution precipitation processes. Additional indications for the activity of dissolution and precipitation in the albite samples deformed here are the indented and lobate grain boundaries achieved by dissolution at grain-to-grain contacts (Cox and Paterson 1991; Knipe 1989; Tenthorey and Cox 2006) and the high fraction of tightly interlocking grains (e.g., Kanagawa et al. 2000). Microstructural observations also suggest the activity of dissolution precipitation processes in the labradorite sample deformed at 800 °C and 1.0 GPa. This is indicated by the formation of grain overgrowths with a chemical composition different to the starting material, as well as the growth of new large grains of zoisite. Stünitz and Tullis (2001) attributed the development of similar microstructures in Sonora labradorite aggregates deformed at 750 °C and 1.5 GPa to diffusion-accommodated grain boundary sliding.

We conclude that in all of our high temperature and pressure experiments on feldspar gouges deformation was mainly accommodated by dissolution precipitation processes. This process is favored by the small grain size of the aggregates, the high deformation temperatures and the presence of fluids (water and melt) in the system. Because samples deformed in the presence of melt show similar microstructures to melt –free samples, we infer that the activation of diffusion creep (more specifically solution precipitation) in this case is not reliant upon the formation of melt but can also occur due to the small amount of water in the starting material. The formation of melt in the system accelerates the process, as demonstrated by the pervasive compositional changes in melt bearing samples with respect to the minor and more localized compositional changes in the samples deformed without melt. Enhancement of the diffusion process in the presence of melt has been described, among others, by Cooper and Kohlstedt (1984), Dell'Angelo et al. (1987), Ji and Mainprice (1986), Pharr and Ashby (1983) and Raj (1982). Cooper and Kohlstedt (1984) observed that the addition of few wt% melt into a dry, fine-grained olivine aggregate increases dramatically (by a factor of 2-5) the creep rate of the material as the melt present along interconnected pores and channels provides rapid diffusion pathways and enables grain boundary diffusion to accommodate the deformation.

5.5.4 Mechanical Data

K-feldspar aggregates deformed at 700 °C show peak strength (shear stress) of 350 MPa followed by pronounced weakening, whereas samples deformed at 800 °C and 900 °C show steady state flow at shear stresses of 100-160 MPa. This observation, together with microstructural observations, indicates a different mechanical evolution in the sample deformed at 700 °C compared to those deformed at higher temperatures. The sample deformed at 700 °C shows incipient strain localization, no melt formation and limited chemical homogenization. On the other hand, samples deformed at higher temperatures show formation of melt rich grain boundaries and melt rich bands, as well as extensive chemical homogenization. Melt bearing samples (K-feldspar deformed at 800 °C and 900 °C) show similar deformation trends, strength values and microstructures suggesting that above the solidus (>700 °C) the deformation mechanism is not temperature independent. We assume that the weakening that occurred in the K-feldspar sample deformed at 700 °C is related to localization of deformation into shear bands with increasing strain. Weakening resulting from localization of deformation in to bands oriented at low angles to the shear plane has been reported by Kohlstedt and Holtzman (2009). Conversely, Kanagawa et al. (2000) reported a continuous strength increase in samples where deformation was homogeneously distributed across the entire gouge layer. This latter case is applicable to the deformed labradorite sample (mn345), which shows continuous strain hardening and homogeneously distributed deformation without the formation of shear bands.

The albite sample deformed at 900 °C shows a similar flow stress to the K-feldspar sample deformed at the same temperature. Microstructural observations indicate no melt formation in the albite sample, in accordance with thermodynamic calculations. This suggests that the formation of a few percent melt (5-6 vol%) in the K-feldspar gouge samples does not significantly influence the mechanical behavior. This is in agreement with the arguments of Rosenberg and Handy (2005) who suggested that at a melt fraction <7% the bulk stress of granular samples is supported by the solid framework, because at these low melt contents the melt is poorly interconnected.

In addition, our experiments do not show a pronounced decrease in rock strength that could be attributed to a melt-enhanced switch from dislocation- to diffusion-creep, as observed by Dell'Angelo and Tullis (1988), Dell'Angelo et al. (1987), Molen and Paterson (1979), Paquet et al. (1981), Rushmer (1995), Rutter and Neumann (1995) and Rosenberg and Handy (2005). This may be the case because the feldspar gouges deformed in this work contain enough water to promote dissolution and precipitation processes from the very earliest stages of the experiments (see above),

and thus the formation of melt during deformation only enhances the dissolution precipitation processes without leading to a switch in deformation mechanism.

5.6 Conclusions

Shear experiments on fine grained feldspar gouges at a confining pressure of 1.0 GPa and temperatures between 700° – 900 °C show that K-feldspar, albite and labradorite gouges containing a small amount of water (0.1-0.3 wt% H_2O) deform mainly by dissolution precipitation creep. Evidence for dissolution precipitation processes in the deformed samples includes pervasive chemical homogenization of the gouge materials, the nucleation and growth of new euhedral grains with compositions distinct from the starting materials, overgrowth structures, lobate and indented grain boundaries, a high fraction of interlocking grains and the development of preferentially oriented porosity including open grain boundaries. The presence of melt in samples deformed at ≥800 °C accelerates dissolution and precipitation processes, but melt does not have a major influence on the mechanical properties of the material due to the low overall melt fraction (5-6 vol%). In melt-bearing samples, microstructural observations indicate that melt is preferentially collected in shear bands due to a combination of stress-driven melt segregation and preferential melt formation associated with shear band dilatancy.

BIBLIOGRAPHY

Adachi T, Hokada T, Osanai Y, Toyoshima T, Baba S, Nakano N (2010) Titanium behavior in quartz during retrograde hydration: Occurrence of rutile exsolution and implications for metamorphic processes in the Sør Rondane Mountains, East Antarctica. Polar Science 3:222–234. doi: 10.1016/j.polar.2009.08.005

Adams BL, Wright SI, Kunze K (1993) Orientation Imaging : The Emergence of a New Microscopy. Metallurgical Transactions A 24:819–831.

Afonso JC, Ranalli G (2004) Crustal and mantle strengths in continental lithosphere: is the jelly sandwich model obsolete? Tectonophysics 394:221–232. doi: 10.1016/j.tecto.2004.08.006

Alling H. (1938) Plutonic perthites. Journal of Geology 46:142–165.

Allmendinger RW, Hauge TA, C HE, Potter CJ, Oliver J (1987) Tectonic heredity and the layered lower crust in the Basin and Range province, western United States. Continental extensional tectonics

Antonellini M, Aydin A (1994) Effect of faulting on fluid flow in porous sandstones: petrophysical properties. AAPG Bulletin 78:355–377.

Arzi AA (1978) Critical phenomena in the rheology of partially melted rocks. Tectonophysics 44:173–184.

Austerheim H (1987) Eclogitization of lower crustal granulites by fluid migration through shear zones. Earth and Planetary Science Letters 81:221–232.

Ave'Lallemant HG, Carter NL (1970) Syntectonic recrystallization of olivine and modes of flow in the upper mantle. Geological Society of America Bulletin 81:2203–2220.

Baeta RD, Ashbee K (1969a) Slip systems in quartz : I. Experiments. American Mineralogist 54:1551–1573.

Baeta RD, Ashbee K (1969b) Slip systemy in Quartz: II. Interpretation. American Mineralogist 54:1574–1582.

Von Bargen N, Waff HS (1986) Permeabilities, interfacial areas and curvatures of partially molten systems: Results of numerical computations of equilibrium microstructures. Journal of Geophysical Research 91:9261. doi: 10.1029/JB091iB09p09261

Barker AK, Coogan LA, Gillis KM, Hayman NW, Weis D (2010) Direct observation of a fossil high-temperature, fault-hosted, hydrothermal upflow zone in crust formed at the East Pacific Rise. Geology 38:379–382. doi: 10.1130/G30542.1

Barreiro JG, Lonardelli I, Wenk HR, Dresen G, Rybacki E, Ren Y, Tomé CN (2007) Preferred orientation of anorthite deformed experimentally in Newtonian creep. Earth and Planetary Science Letters 264:188–207. doi: 10.1016/j.epsl.2007.09.018

Bastin GF, Van Loo FJJ, Vosters PJC, Vrolijk JWGA (1984) An iterative procedure for the correction of secondary fluorescence effects in electron-probe microanalysis near phase boundaries. Spectrochimica Acta Part B: Atomic Spectroscopy 39:1517–1522. doi: 10.1016/0584-8547(84)80174-3

Beaumont C, Jamieson RA, Nguyen MH, Lee B (2001) Himalayan tectonics explained by extrusion of a low-viscosity crustal channel coupled to focused surface denudation. Nature 414:738–42. doi: 10.1038/414738a

Behrens H (1995) Determination of water solubilities in high-viscosity melts: An experimental study on NaAlSi3O8 and KAlSi3O8 melts. Eur J Mineral 7:905–920.

Behrens H, Meyer M, Holtz F, Benne D, Nowak M (2001) The effect of alkali ionic radius, temperature, and pressure on the solubility of water in MAlSi3O8 melts (M=Li, Na, K, Rb). Chemical Geology 174:275–289.

Du Bernard X, Eichhubl P, Aydin A (2002) Dilation bands: A new form of localized failure in granular media. Geophysical Research Letters. doi: doi:10.1029/2002GL015966

Berthé D, Choukroune P, Jegouzo P (1979) Orthogneiss, mylonite and non coaxial deformation of granites: the example of the South Armorican Shear Zone. Journal of Structural Geology 1:31–42. doi: 10.1016/0191-8141(79)90019-1

Bésuelle P (2001) Theoretical and experimental conditions. Journal of Geophysical Research 106:435–442.

Blacic JD, Christie JM (1984) Plasticity and hydrolytic weakening of quartz single crystals. Journal of Geophysical Research 89:4223–4239.

Bohlen SR, Mezger K (1989) Origin of granulite terranes and the formation of the lowermost continental crust. Science 244:326–329.

Bons PD, Den Brok B (2000) Crystallographic preferred orientation development by dissolution - precipitation creep. Journal of Structural Geology 22:1713–1722.

Borg IY, Hear HC (1970) Experimental deformation of Cataclastic flow in anorthosite plagioclase. Experimental and Natural Rock Deformation. Berlin, pp 375–403

Boyd F, England J (1960) Apparatus for phase-equilibrium measurements at pressures up to 50kb and temperatures up to 1750°C. Journal of Geophysical Research 65:741–748.

Brady JB, Yund RA (1983) Interdiffusion of K and Na in alkali feldspar: homogenization experiments. American Mineralogist 68:106–111.

Brodie KH, Rutter EH (1985) On the relationship between deformation and metamorphism with special reference to the behavior of basic rocks. In: Thompson AB, Rubie D (eds) Kinematics, Textures, and Deformation: Advances in Physical Geochemistry. Springer Verlag, Berlin, pp 138–179

Brown D, Carbonell R, Kukkonen I, Ayala C, Golovanova I (2003) Composition of the Uralide crust from seismic velocity (Vp, Vs), heat flow, gravity, and magnetic data. Earth and Planetary Science Letters 6621:1–17.

Brown M (2007) Crustal melting and melt extraction , ascent and emplacement in orogens : mechanisms and consequences. Journal of the Geological Society 164:709–730.

Brown M (1994) The generation, segregation, ascent and emplacement of granite magma: the migmatite-to-crustally-derived granite connection in thickened orogens. Earth-Science Reviews 36:83–130. doi: 10.1016/0012-8252(94)90009-4

Brown M (2010) The spatial and temporal patterning of the deep crust and implications for the process of melt extraction. Philosophical transactions Series A, Mathematical, physical, and engineering sciences 368:11–51. doi: 10.1098/rsta.2009.0200

Brown M, Solar GS (1998) Shear-zone systems and melts : feedback relations and self-organization in erogenic belts. Journal of Structural Geology 20:211–277.

Bruhn D, Groebner NJ, Kohlstedt DL (2000) An interconnected network of core-forming melts produces by shear deformation. Nature 883–886.

Bürgmann R, Dresen G (2008) Rheology of the Lower Crust and Upper Mantle : Evidence from Rock Mechanics , Geodesy , and Field Observations. Annual Review of Earth and Planetary Sciences 36:531–67. doi: 10.1146/annurev.earth.36.031207.124326

Burnham CW, Jahnes RH (1962) A method for determining the solubility of water in silicate melts. American Journal of Science 260:721–745.

Burov EB, Diament M (1995) The effective elastic thickness (Te) of continental lithosphere: What does it really mean? Journal of Geophysical Research 100:3905–3928. doi: 10.1029/94Jb02770

Burov EB, Watts AB (2006) The long-term strength of continental lithosphere: " jelly sandwich " or " crème brûlée "? GSA Today. doi: 10.1130/1052-5173(2006)016<4

Bussod GY, Christie JM (1991) Textural development and melt topology in spinel lherzolite experimentally deformed at hypersolidus conditions. Journal of Petrology 17–39.

Campbell ME, Hanson JB, Minarik WG, Stix J (2009) Thermal History of the Bandelier Magmatic System: Evidence for Magmatic Injection and Recharge at 1.61 Ma as Revealed by Cathodoluminescence and Titanium Geothermometry. The Journal of Geology 117:469–485. doi: 10.1086/604744

Chadam J, Hoff D, Merino E, Ortoleva P, Sen A (1986) Reactive nfiltration instability. IMA Journal of Applied Mathematics 36:207–221.

Chen WP, Molnar P (1983) Focal depths of intracontinental and intraplate earthquakes and their implications for the thermal and mechanical properties of the lithosphere. Journal of Geophysical Research 88:4183–4214.

Cherniak DJ, Watson BE, Wark DA (2007) Ti diffusion in quartz. Chemical Geology 236:65 – 74. doi: 10.1016/j.chemgeo.2006.09.001

Christensen NI, Mooney WD (1995) Seismic velocity structure and composition of the continental crust: a global view. Journal of Geophysical Research 100:9761–9788.

Christoffersen R, Yund RA, Tullis J (1983) Inter-difrusion of K and Na in alkali feldspars : diffusion couple experiments. american Mineralogist 68:1126–1133.

Clark MK, Royden LH (2000) Topographic ooze : Building the eastern margin of Tibet by lower crustal flow. Geology 28:703–706. doi: 10.1130/0091-7613(2000)28<703

Cloetingh S, Burov EB (1996) Thermomechanical structure of European continental lithosphere: constraints from rheological profiles and EET estimate. Geophysical Journal International 124:695–723.

Coggon R, Holland TJB (2002) Mixing properties of phengitic micas and revised garnet–phengite thermobarometers. Journal of Metamorphic Geology 20:683–696.

Collins WJ, Sawyer EW (1996) Pervasive granitoid magma transfer through the lower – middle crust during non-coaxial compressional deformation. Journal of Metamorphic Geology 14:565–579.

Condie K. (1999) Mafic crustal xenoliths and the origin of the lower continental crust. Lithos 46:95–101.

Connolly JAD (2009) The geodynamic equation of state: what and how. Geochemistry Geophysics Geosystems 10:

Cooper RF (1990) Differential stress-induced melt migration: An experimental approach. Journal of Geophysical Research 95:6979. doi: 10.1029/JB095iB05p06979

Cooper RF, Kohlstedt DL (1984) Solution-precipitation enhanced diffusional creep of partially molten olivine-basalt aggregates during hot-pressing. Tectonics 107:207–233.

Cooper RF, Kohlstedt DL, Chyung K (1989) Solution-precipitation enhanced creep in solid-liquid aggregates which display a non-zero dihedral angle. Acta Metallurgica 37:1759–1771. doi: 10.1016/0001-6160(89)90061-8

Cox SF, Paterson MS (1991) Experimental dissolution-precipitation creep in quartz aggregates at high-temperatures. Geophysical Research Letters 18:1401–1404.

Daines MJ, Kohlstedt DL (1997) Influence of deformation on melt topology in peridotites. Journal of Geophysical Research 107:10257–10271.

Daines MJ, Kohlstedt DL (1993) A laboratory study of melt migration. Philosophical transactions of the Royal Society of London Series A 3:43–52.

Davidson C, Schmid SM, Hollister LS (1994) Role of melt during deformation in the deep crust. Terra Nova 6:133–142.

Dawson JB, Carswell DA, Hall J, Wedepohl KH (1986) The Nature of the Lower Continental Crust. 394.

Day HW, Fenn PM (1982) No TitleEstimating the P-T-XH2O conditions during crystallization of low calcium granites. Journal of Geology 90:485–507.

Dell'Angelo LN, Tullis J (1988) Experimental deformation of partially melted granitic aggregates. Journal of Metamorphic Geology 6:495–515. doi: 10.1111/j.1525-1314.1988.tb00436.x

Dell'Angelo LN, Tullis J, Yund RA (1987) Transition from dislocation creep to melt-enhanced diffusion creep in fine-grained granitic aggregates. Tectonophysics 139:325–332.

Derby B (1991) The dependence of grain size on stress during dynamic recrystallization. Acta Metallurgica 39:955–962.

Dimanov A, Dresen G, Wirth R (1998) High-temperature creep of partially molten plagioclase aggregates. Journal of Geophysical Research 103:9651–9664. doi: 10.1029/97JB03742

Dimanov A, Wirth R, Dresen G (2000) The effect of melt distribution on the rheology of plagioclase rocks. Tectonophysics 328:307–327.

Dingwell DB, Romano C, Hess K-U (1996) The effect of water in the viscosity of a haplogranitic melt under P–T–X conditions relevant to silicic volcanism. Contributions to Mineralogy and Petrology 124:19–28.

Donovan JJ, Lowers HA, Rusk BG (2011) Improved electron probe microanalysis of trace elements in quartz. American Mineralogist 96:274–282. doi: 10.2138/am.2011.3631

Drury MR, Urai JL (1990) Deformation-related recrystallization processes. Tectonophysics 172:235–253.

Ebadi A, Johannes W (1991) Beginning of melting and composition of first melts in the system Qz - Ab - Or - H20 - CO2. Contributions to Mineralogy and Petrology 106:286–295.

Evans B, Hay RS, Shimizu N (1986) Diffusion-induced grain-boundary migration in calcite. Geology 14:60–63. doi: 10.1130/0091-7613(1986)14<60

Fitz Gerald JD, McLaren AC (1982) The Microstructures of Microcline from Some Granitic Rocks and Pegmatites. Contributions to Mineralogy and Petrology fitz:219–229.

Flem B, Larsen RB, Grimstvedt A, Mansfeld J (2002) In situ analysis of trace elements in quartz by using laser ablation inductively coupled plasma mass spectrometry. Chemical Geology 182:237–247. doi: 10.1016/S0009-2541(01)00292-3

Flynn GW, Powell WJA (1979) The Cutting and Polishing of Electro-optical Materials. Adam Hilger, Bristol

Fountain DM, Percival J, Salisbury MH (1990) Exposed cross sections of the continental crust-synopsis. In: Salisbury MH, Fountain DM (eds) Exposed Cross-sections of the Continental Crust-, Kluwer. Amsterdam, pp 653–662

Fountain DM, Salisbury MH (1981) Fountain D. M. and Salisbury M. H. (1981) Exposed crosssections through the continental crust: implications for crustal structure, petrology, and evolution. Earth and Planetary Science Letters 56:263–277.

Fournelle J (2007) Problems in trace elements EMPA: modeling secondary fluorescence with PENEPMA. EOS Transactions American Geophysical Union m:

Frondel C (1962) Dana's system of Mineralogy. Wiley, New York

Fuhrman ML, Lindsley DH (1988) Ternary-feldspar modelling and thermometry. American Mineralogist 73:201–215.

Gao S, Zhang BR, Jin Z-M, Kern H, Luo TC, Zhao ZD (1998) How mafic is the lower crust? Earth and Planetary Science Letters 161:101–117.

Girard G, Stix J (2010) Rapid extraction of discrete magma batches from a large differentiating magma chamber: the Central Plateau Member rhyolites, Yellowstone Caldera, Wyoming. Contributions to Mineralogy and Petrology 160:441–465. doi: 10.1007/s00410-009-0487-1

Gleason GC, Tullis J, Heidelbach F (1993) The role of dynamic recrystallization in the development of lattice preferred orientations in experimentally deformed quartz aggregates. Journal of Structural Geology 15:1145–1168. doi: 10.1016/0191-8141(93)90161-3

Godard G, Van Roermund HLM (1995) Deformation-induced clinopyroxene fabrics from eclogites. Journal of Structural Geology 17:1425–1443.

Goranson RW (1938) Silicate-water systems: Phase equilibria in the NaAlSi3O8-H2O and KAlSi3O8 -H2O systems at high temperatures and pressures. American Journal of Science 35A:71–92.

Goranson RW (1936) Silicate-water system: The solubility of water in albite-melt. Tran Am Geophys Union 17:257–259.

Goranson RW (1931) The solubility of water in granitic magmas. American Journal of Science 22:481–502.

Gottstein G, Mecking H (1985) Recrystallization. In: Wenk HR (ed) Preferred Orientation in Deformed Metals and Rocks: An Introduction to Modern Texture Analysis. Academic Press, Orlando, FL, pp 183–218

Green HW, Griggs DT, Christie JM (1970) Syntectonic and annealing recrystallization of fine-grained quartz aggregates. In: Paulitsch P (ed) Experimetnal and natural rock deformation: International Symposium. Darmstadt, Germany, pp 272–335

Greenwood JP, Hess PC (1998) Congruent melting kinetics of albite ' Theory and experiment. journal of geophysical research 103:29815–29828.

Griggs DT (1967) Hydrolitic weakening of quartz and other silicates. Geophysical Journal International 14:19–31.

Grujic D, Stipp M, Wooden JL (2011) Thermometry of quartz mylonites: Importance of dynamic recrystallization on Ti-in-quartz reequilibration. Geochemistry geophysics geosystems 12:1–19. doi: 10.1029/2010GC003368

Guillope M, Poirier JP (1979) Dynamic recrystallization during creep of singlecrystalline halite: An experimental study. Journal of Geophysical Research 84:5557–5567.

Gutmann JT, Martin RF (1976) Crystal chemistry , unit cell dimensions , and structural state of labradorite megacrysts from Sonora, Mexico. Schweizerische mineralogische und petrographische Mitteilungen 56:55–64.

Hadizadeh J, Tullis J (1992) Cataclastic flow and semi-brittle deformation of anorthosite. Journal of Structural Geology 14:57–63.

Hall CE, Parmentier EM (2000) Spontaneous melt localization in a deforming solid with viscosity variations due to water weakening. Geophysical Research Letters 27:9–12.

Handy M., Brun J-P (2004) Seismicity, structure and strength of the continental lithosphere. Earth and Planetary Science Letters 223:427–441. doi: 10.1016/j.epsl.2004.04.021

Handy MR, Mulch A, Rosenau M, Rosenberg CL (2001) The role of fault zones and melts as agents of weakening, hardening and differentiation of the continental crust: a synthesis. The Nature and Tectonic Significance of Fault Zone Weakening

Hart RJ, Andreoli MAG, Tredoux M, Dewit MJ (1990) Geochemistry across an exposed section of Archean crust at Vredefort, South Africa with implications for midcrustal discontinuities. Chemical Geology 82:21–50.

Härtel M, Herweg M (2013) Linking titanium-in-quartz thermometry and quartz microstructures : strong evidence of continued vein formation during strain localization.

Hay RS, Evans B (1987a) Chemically induced grain boundary migration in calcite: temperature dependence, phenomenology, and possible applications to geologic systems. Contributions to Mineralogy and Petrology 97:127–141.

Hay RS, Evans B (1987b) Chemically induced migration in low and high angle calcite grain boundaries. Acta Metallurgica 35:2049–2062.

Hayden LA, Watson BE (2007) Rutile saturation in hydrous siliceous melts and its bearing on Ti-thermometry of quartz and zircon. Earth and Planetary Science Letters 258:561–568. doi: 10.1016/j.epsl.2007.04.020

Heacock JH (1971) The Structure and Physical Properties of the Earth's Crust. 348.

Heidelbach F, Post A, Tullis J (2000) Crystallographic preferred orientation in albite samples deformed experimentally by dislocation and solution precipitation creep. Journal of Structural Geology 22:1649–1661. doi: 10.1016/S0191-8141(00)00072-9

Hermann J, O'Neill HSC, Berry AJ (2005) Titanium solubility in olivine in the system TiO2–MgO–SiO2: no evidence for an ultra-deep origin of Ti-bearing olivine. Contributions to Mineralogy and Petrology 148:746–760. doi: 10.1007/s00410-004-0637-4

Hirth G, Kohlstedt DL (2003) Rheology of the upper mantle and the mantle wedge: a view from the experimentalists. Geophysical Monograph 138:83–105.

Hirth G, Kohlstedt DL (1995a) Experimental constraints on the dynamics of the partially molten upper mantle : Deformation in the diffusion creep regime. Journal of Geophysical Research 100:1981–2001.

Hirth G, Kohlstedt DL (1995b) Experimental constraints on the dynamics of the partially molten upper mantle, 2, Deformation in the dislocation creep regime. Journal of Geophysical Research 100:15441–15449.

Hirth G, Teyssier C, Dunlap J (2001) An evaluation of quartzite flow laws based on comparisons between experimentally and naturally deformed rocks. International Journal of Earth Sciences 90:77–87. doi: 10.1007/s005310000152

Hirth G, Tullis J (1992) Dislocation creep regimes in quartz aggregates. Journal of Structural Geology 14:145–159. doi: 10.1016/0191-8141(92)90053-Y

Holbrook WS, Mooney WD, Christensen NI (1992) The seismic velocity structure of the deep continental crust. In: Fountain DM, Arculus R, Kay RW (eds) Continental Lower Crust, Elsevier. Amsterdam, pp 1–44

Holland TJB, Powell R (1998) An internally-consistent thermodynamic dataset for phases of petrological interest. Journal of Metamorphic Geology 16:309–344.

Holland TJB, Powell R (2001) Calculation of Phase Relations Involving Haplogranitic Melts Using an Internally Consistent Thermodynamic Dataset. Journal of Petrology 42:673–683.

Holness MB (2006) Melt – Solid Dihedral Angles of Common Minerals in Natural Rocks. Journal of Petrology 47:791–800. doi: 10.1093/petrology/egi094

Holtz F, Behrens H, Dingwell DB, Johannes W (1995) Water solubility in haplogranitic melts. Compositional, pressure and temperature dependence. American Mineralogist 80:94–108.

Holtzman BK, Groebner NJ, Zimmerman ME, Ginsberg SB, Kohlstedt DL (2003a) Stress-driven melt segregation in partially molten rocks. Geochemistry Geophysics Geosystems 4:8607. doi: doi:10.1029/2001GC000258

Holtzman BK, Kohlstedt DL (2007) Stress-driven Melt Segregation and Strain Partitioning in Partially Molten Rocks: Effects of Stress and Strain. Journal of Petrology 48:2379–2406. doi: 10.1093/petrology/egm065

Holtzman BK, Kohlstedt DL, Zimmerman ME, Heidelbach F, Hiraga T, Hustoft JW (2003b) Melt segregation and strain partitioning: implications for seismic anisotropy and mantle flow. Science 301:1227–30. doi: 10.1126/science.1087132

Holtzman BK, Kohlstedt DL, Zimmerman ME, Heidelbach F, Hiraga T, Hustoft JW (2003c) Supplemental Online Material to Melt Segregation and Strain Partitioning: Implications for Seismic Anisotropy and Mantle Flow. Science 1–9.

Holyoke CW, Kronenberg AK (2010) Accurate differential stress measurement using the molten salt cell and solid salt assemblies in the Griggs apparatus with applications to strength, piezometers and rheology. Tectonophysics 494:17–31. doi: 10.1016/j.tecto.2010.08.001

Holyoke CW, Rushmer T (2002) An experimental study of grain scale melt segregation mechanisms in two common crustal rock types. Journal of Metamorphic Geology 20:493–512. doi: 10.1046/j.1525-1314.2002.00381.x

Huang R, Audétat A (2012) The titanium-in-quartz (TitaniQ) thermobarometer: A critical examination and re-calibration. Geochimica et Cosmochimica Acta 84:75–89. doi: 10.1016/j.gca.2012.01.009

Huang WL, Wyllie PJ (1975) Melting reactions in the system NaAlSi3O8-kaAlSi3O8-SiO2 to 35 kilobars, dry and with excess water. Journal of Geology 83:737–748.

Jacamon F, Larsen RB (2009) Trace element evolution of quartz in the charnockitic Kleivan granite, SW-Norway: The Ge/Ti ratio of quartz as an index of igneous differentiation. Lithos 107:281–291. doi: 10.1016/j.lithos.2008.10.016

Jackson J (2002) Strength of the continental lithosphere: Time to abandon the jelly sandwich ? GSA Today

Jackson JA, Austrheim H, McKenzie D, Priestley K (2004) Metastability, mechanical strength, and the support of mountain belts. Geology 32:625–628.

Jessell MW (1987) Grain-boundary migration microstructures in a naturally deformed quartzite. Journal of Structural Geology 9:1007.

Ji S, Mainprice D (1986) Transition from power law to newtonian creep in experimentally deformed dry albite rock. EOS Transactions American Geophysical Union 67:1235.

Jin Z-M, Green HW, Zhou Y (1994) Melt topology in partially molten mantle peridotite during ductile deformation. letters to nature 372:164–166.

Johannes W, Holtz F (1996) Petrogenesis and Experimental Petrology of Granitc Rocks. Springer

Kadik AA, Lebedev YB (1968) Temperature dependenceof the solubility of water in an albite melt at high pressures. Geochemistry International 12:1172–1181.

Kanagawa K, Cox SF, Zhang S (2000) Effects of dissolution-precipitation processes on the strength and mechanical behavior of quartz gouge at high-temperature hydrothermal conditions velocity. Journal of Geophysical Research 105:11,115–11,126.

Kawasaki T, Osanai Y (2008) Empirical thermometer of TiO2 in quartz for ultrahigh-temperature granulites of East Antarctica. Geological Society, London, Special Publications 308:419–430. doi: 10.1144/SP308.21

Kay RW, Kay SM (1981) The nature of the lower continental crust: inferences from geophysics, surface geology, and crustal xenoliths. Reviews of Geophysics 19:271–297.

Kelemen PB, Dick HJB (1995) Focused melt flow and localized deformation in the upper mantle: Juxtaposition of replacive dunite and ductile shear zones in the Josephine Peridotite, SW Oregon. Journal of Geophysical Research 100:423–438.

Kelemen PB, Shimizu N, Salters VJM (1995) Extraction of mid-ocean-ridge basalt from the upwelling mantle by focused flow of melt in dunite channels.pdf. Nature 375:747–753.

Kennett BLN, Van der Hilst RD (1998) Seismic structure of the mantle: from subduction zone to craton. In: Jackson I (ed) The Earth's Mantle-Composition, Structure, and evolution, Univ. Pres. Cambridge, pp 381–404

Kern H, Gaob S, Jin Z, Popp T, Jin S (1999) Petrophysical studies on rocks from the Dabie ultrahigh-pressure (UHP) metamorphic belt, Central China: implications for the composition and delamination of the lower crust. Tectonics 301:191–215.

Ketcham RA (1996) Distribution of heat-producing elements in the upper and middle crust of southern and west central Arizona: evidence from core complexes. Journal of Geophysical Research 101:13611–13632.

King DSH, Zimmerman ME, Kohlstedt DL (2010a) Stress-driven Melt Segregation in Partially Molten Olivine-rich Rocks Deformed in Torsion. Journal of Petrology 51:612–626. doi: 10.1093/petrology/egp062

King J, Harris N, Argles T, Parrish R, Zhang H (2010b) Contribution of crustal anatexis to the tectonic evolution of Indian crust beneath southern Tibet. Geological Society of America Bulletin 123:218–239. doi: 10.1130/B30085.1

Knipe RJ (1989) Deformation mechanisms-recognition from natural tectonites. Journal of Structural Geology 11:127–146.

Kohlstedt DL (1992) Structure, rheology and permeability of partially molten rocks at low melt fractions. In: Philipps-Morgan J, Blackman D., Sinton J. (eds) Mantle Flow and Melt Generation at Mid-Ocean Ridges, Geophysica. American Geophysical Union, Washington, pp 103–121

Kohlstedt DL, Evans B, Mackwell SJ (1995) Strength of the lithoshpere: Constraints imposed by laboratory experiments. Journal of Geophysical Research 100:17587–17602.

Kohlstedt DL, Holtzman BK (2009) Shearing Melt Out of the Earth: An Experimentalist's Perspective on the Influence of Deformation on Melt Extraction. Annual Review of Earth and Planetary Sciences 37:561–593. doi: 10.1146/annurev.earth.031208.100104

Kohlstedt DL, Zimmerman ME (1996) Rheology of partially molten mantle rocks. Annual Review of Earth and Planetary Sciences 24:41–62.

Kohlstedt DL, Zimmerman ME, Mackwell SJ (2009) Stress-driven Melt Segregation in Partially Molten Feldspathic Rocks. Journal of Petrology 51:9–19. doi: 10.1093/petrology/egp043

Kohn MJ, Northrup CJ (2009) Taking mylonites' temperatures. Geology 37:47–50. doi: 10.1130/G25081A.1

Kronenberg AK, Shelton G (1980) Deformation microstructures in experimentally deformed Maryland Diabase. Journal of Structural Geology 2:341–352.

Kruse R, Stünitz H, Kunze K (2001) Dynamic recrystallization processes in plagioclase porphyroclasts. Journal of Structural Geology 23:1781–102.

Lambert IB, Heier KS (1968) Geochemical investigations of deep-seated rocks in the Australian Shield. Lithos 1:30–53.

Larsen RB, Henderson I, Ihlen PM, Jacamon F (2004) Distribution and petrogenetic behaviour of trace elements in granitic pegmatite quartz from South Norway. Contributions to Mineralogy and Petrology 147:615–628. doi: 10.1007/s00410-004-0580-4

Lexa O, Schulmann K, Janoušek V, Štípská P, Guy A, Racek M (2011) Heat sources and trigger mechanisms of exhumation of HP granulites in Variscan orogenic root. Journal of Metamorphic Geology 29:79–102. doi: 10.1111/j.1525-1314.2010.00906.x

Luan FC, Paterson MS (1990) Preparation and deformation of synthetic aggregates of quartz. Journal of Geophysical Research 97:

Lund MG, Austerheim H, Erambert M (2004) Earthquakes in the deep continental crust- Insights from studies on exhumed high-pressure rocks. Geophysical Journal International 158:569–576. doi: 10.1111/j.1365- 246X.2004.02368.x

Luth WC, Jahnes RH, Tuttle OF (1964) The granite System at pressure of 4 to 10 kilobars. Journal of Geophysical Research 69:759–773.

Maaløe S, Scheie A (1982) The permeability controlled accumulation of primary magma. Contributions to Mineralogy and Petrology 81:350–357.

Mackwell SJ, Zimmerman ME, Kohlstedt DL (1998) High- temperature deformation of dry diabase with application to tectonics on Venus. Journal of Geophysical Research 103:957–984.

Maggi A, Jackson JA, McKenzie D, Priestley K (2000) Earthquake focal depth, effective elastic thickness, and the strength of the continental lithosphere. Geology 28:495–498.

Mancktelow N, Pennacchioni G (2004) The influence of grain boundary fluids on the microstructure of quartz-feldspar mylonites. Journal of Structural Geology 26:47–69. doi: 10.1016/S0191-8141(03)00081-6

Manning CE, Wilke M, Schmidt C, Cauzid J (2008) Rutile solubility in albite-H2O and Na2Si3O7-H2O at high temperatures and pressures by in-situ synchrotron radiation micro-XRF. Earth and Planetary Science Letters 272:730–737. doi: 10.1016/j.epsl.2008.06.004

Marchildon N, Brown M (2002) Grain-scale melt distribution in two contact aureole rocks: implications for controls on melt localization and deformation. Journal of Metamorphic Geology 20:381–396. doi: 10.1046/j.1525-1314.2002.00376.x

Marshall DB, Mclaren AC (1977) Deformation Mechanisms in Experimentally Deformed Plagioclase Feldspars. Physics and Chemistry of Minerals 1:351–370.

Martin JJ, Armington AF (1983) Effect of growth rate on quartz defects. Journal of Crystal Growth 62:203–206.

Matthews DH, Cheadle MJ (1986) Deep reflections from the Cale- donides and Variscides west of Britain and comparison with the Himalayas. Reflection seismology: A global perspective

McKenzie D (1984) The Generation and Compaction of Partially Molten. Journal of Petrology 25:713–765.

McMillan P (1994) Water solubility and speciation models. Reviews in Mineralogy and Geochemistry 30:131–156.

McMillan P, Holloway J (1987) Water solubility in aluminosilicate melts. Contributions to Mineralogy and Petrology 97:320–332.

Mecklenburgh J, Rutter EH (2003) On the rheology of partially molten synthetic granite. Journal of Structural Geology 25:1575–1585. doi: 10.1016/S0191-8141(03)00014-2

Menegon L, Nasipuri P, Stünitz H, Behrens H, Ravna EJK (2011) Dry and strong quartz during deformation of the lower crust in the presence of melt. Journal of Geophysical Research 116:1–23. doi: 10.1029/2011JB008371

Menegon L, Pennacchioni G, Heilbronner R, Pittarello L (2008) Evolution of quartz microstructure and c-axis crystallographic preferred orientation within ductilely deformed granitoids (Arolla unit, Western Alps). Journal of Structural Geology 30:1332–1347. doi: 10.1016/j.jsg.2008.07.007

Menegon L, Stünitz H, Nasipuri P, Heilbronner R, Svahnberg H (2013) Transition from fracturing to viscous flow in granulite facies perthitic feldspar (Lofoten, Norway). Journal of Geology 48:95–112.

Miller JD, Christensen NI (1994) Seismic signature and geochemistry of an island arc: a multidisciplinary study of the Kohistan accreted terrane, northern Pakistan. Journal of Geophysical Research 99:11623–11642.

Misra S, Burlini L, Burg J-P (2009) Strain localization and melt segregation in deforming metapelites. Physics of the Earth and Planetary Interiors 177:173–179. doi: 10.1016/j.pepi.2009.08.011

Molen I Van Der, Paterson MS (1979) Experimental Deformation of Partially-Melted Granite. Contributions to Mineralogy and Petrology 70:299–318.

O'Reilly SY, Griffin WL (1996) 4-D lithosphere mapping: methodology and examples. Tectonophysics 262:3–18.

Ostapenko GT, Tarashchan AN, Mitsyuk BM (2007) Rutile-quartz geothermobarometer. Geochemistry International 45:506–508. doi: 10.1134/S0016702907050084

Paillat O, Elphick SC, Brown WL (1992) The solubility of water in NaAlSi3O8 melts: A re-examination of Ab-H2O phase relationships and critical behaviour at high pressures. Contributions to Mineralogy and Petrology 112:490–500.

Paquet J, Francois P, Nedelec A (1981) Effect of partial melting on rock deformation: Experimental and natural evidences on rocks of granitic compositions. Tectonophysics 78:545–565. doi: 10.1016/0040-1951(81)90028-7

Parsons R, Hustoft JW, Holtzman DL, Kohlstedt DL, Phipps Morgan J (2004) Stress-driven melt segregation and organization in partially molten rocks; III, Annealing experiments and surface tension-driven redistribution of melt; AGU 2004 fall meeting. EOS Transactions American Geophysical Union 85:@Abstract V21A–0599.

Passchier CW, Trouw RAJ (1996) Microtectonics. Springer Verlag, Berlin

Paterson MS (1978) Experimental Rock Deformation – The Brittle Field, Springer V. Berlin

Paterson MS, Luan FC (1990) Quartzite rheology under geological conditions. In: Knipe RJ, Rutter EH (eds) Deformation Mechanisms, Rheology and Tectonics, Geol. Soc. pp 299–307

Pearce MA, Wheeler J, Prior DJ (2011) Relative strength of mafic and felsic rocks during amphibolite facies metamorphism and deformation. Journal of Structural Geology 33:662–675.

Pec M (2012) Experimental Investigation on the Rheology of Fault Rocks. Universität Basel

Pec M, Stünitz H, Heilbronner R (2011) Semi-brittle deformation of granitoid gouges in shear experiments at elevated pressures and temperatures. Journal of Structural Geology 1–22. doi: 10.1016/j.jsg.2011.09.001

Pennacchioni G, Menegon L, Leiss B, Nestola F, Bromiley G (2010) Development of crystallographic preferred orientation and microstructure during plastic deformation of natural coarse-grained quartz veins. Journal of Geophysical Research. doi: 10.1029/2010JB007674

Pharr GM, Ashby MF (1983) ON CREEP ENHANCED BY A LIQUID PHASE. Acta Metallurgica 31:129–138.

Priestley K, Jackson J, McKenzie D (2008) Lithospheric structure and deep earthquakes beneath India, the Himalaya and southern Tibet. Geophysical Journal International 172:345–362. doi: 10.1111/j.1365-246X.2007.03636.x

Prior DJ, Boyle AP, Brenker F, Cheadle MC, Austin D, Lopez G, Peruzzo L, Potts GJ, Reddy S, Spiess R, Timms NE, Trimby PW, Wheeler J, Zetterström L (1999) The application of electron backscatter diffraction and orientation contrast imaging in the SEM to textural problems in rocks. American Mineralogist 84:1741–1759.

Priyatkina NS, Kullerud K, Bergh SG, Armitage PEB, Ravna EJK (2011) CO2 sequestration during interactions between fluid and mafic to intermediate intrusive rocks on Vannøya Island, West Troms Basement Complex, North Norway. ICAM, 10th International Congress for Applied Mineralogy, Trondheim. pp 549–558

Putnis A (1992) Introduction to Mineral Sciences. Cambridge University Press, Cambridge

Raj R (1982) Creep in polycrystalline aggregates by matter transport through a liquid phase. Journal of Geophysical Research 87:4731–4739.

Ranalli G (1995) Rheology of the Earth, 2nd ed. Chapman and Hall, London

Ranalli G, Murphy DC (1987) Rheological stratification of the lithosphere. Tectonophysics 132:281–296.

Rankama K, Sahama TG (1950) Geochemistry. University of Chicago Press, Chicago, IL

Richardson CN, Lister JR, McKenzie D (1996) Melt conduits in a viscous porous matrix. Journal of Geophysical Research 101:20,423–20,432.

Richter FM, McKenzie D (1984) Dynamical models for melt segregation from a deformable matrix. Journal of Geology 92:729–740.

Riley GN, Kohlstedt DL (1991) Kinetics of melt migration in upper mantle-type rocks. Earth and Planetary Science Letters 105:500–521.

Riley GN, Kohlstedt DL (1990a) An experimental study of melt migration in an olivine-melt system. In: Ryan MP (ed) Magma Transport and Storage. Wiley, Chichster/Sussex, England, pp 77–86

Riley GN, Kohlstedt DL (1990b) Melt migration in a silicate liquid-olivine system: An experimental test of compaction theory. Geophysical Research Letters 17:2101–2104.

Rosenberg CL, Berger A (2001) Syntectonic Melt Pathways in Granitic Gneisses , and Melt-Induced Transitions in Deformation Mechanisms. Phys Chem Earth 26:287–293.

Rosenberg CL, Handy MR (2005) Experimental deformation of partially melted granite revisited: implications for the continental crust. Journal of Metamorphic Geology 23:19–28. doi: 10.1111/j.1525-1314.2005.00555.x

Rosenberg CL, Handy MR (2001) Mechanisms and orientation of melt segregation paths during pure shearing of a partially molten rock analog (norcamphor ± benzamide). Journal of Structural Geology 23:1917–1932.

Rossi M, Rolland Y, Vidal O, Cox SF (2005) Geochemical variations and element transfer during shear-zone development and related episyenites at middle crust depths: insights from the Mont Blanc granite (French -- Italian Alps). Geological Society, London, Special Publications 245:373–396. doi: 10.1144/GSL.SP.2005.245.01.18

Royden LH, Burchfiel BC, Van der Hilst RD (2008) The geological evolution of the Tibetan Plateau. Science (New York, NY) 321:1054–8. doi: 10.1126/science.1155371

Rudnick RL (1992) Xenoliths—samples of the lower continental crust. In: Fountain DM, Arculus R, Kay RW (eds) Continental Lower Crust, Elsevier. Amsterdam, pp 269–316

Rudnick RL, Fountain DM (1995) NATURE AND COMPOSITION OF THE CONTINENTAL CRUST : A LOWER CRUSTAL PERSPECTIVE. Reviews of Geophysics 33:267–309.

Rudnicky JW, Rice JR (1975) Conditions for the localization of deformation in pressure sensitive dilatant materials. J Mech Phys Solids 23:371–394.

Rushmer T (1995) An experimental deformation study of partially molten amphibolite : Application to low-melt fraction segregation. Journal of Geophysical Research 100:15681–15695.

Rusk BG (2006) Intensity of quartz cathodoluminescence and trace-element content in quartz from the porphyry copper deposit at Butte, Montana. American Mineralogist 91:1300–1312. doi: 10.2138/am.2006.1984

Rusk BG, Lowers HA, Reed MH (2008) Trace elements in hydrothermal quartz: Relationships to cathodoluminescent textures and insights into vein formation. Geology 36:547. doi: 10.1130/G24580A.1

Rutter EH, Neumann DHK (1995) Experimental deformation of partially molten Westerly granite under fluid-absent conditions , with implications for the extraction of granitic magmas. journal of geophysical research 100:15697–15715.

Rybacki E, Dresen G (2000) Dislocation and diffusion creep of synthetic anorthite aggregates. Journal of Geophysical Research 105:17–26.

Rybacki E, Dresen G (2004) Deformation mechanism maps for feldspar rocks. Tectonophysics 382:173–187. doi: 10.1016/j.tecto.2004.01.006

Rybacki E, Wirth R, Dresen G (2008) High-strain creep of feldspar rocks : Implications for cavitation and ductile failure in the lower crust. Geophysical Research Letters. doi: 10.1029/2007GL032478

Sato K, Santosh M (2007) Titanium in quartz as a record of ultrahigh-temperature metamorphism: the granulites of Karur, southern India. Mineralogical Magazine 71:143–154. doi: 10.1180/minmag.2007.071.2.143

Sawyer EW (2001) Melt segregation in the continental crust: distribution and movement of melt in anatectic rocks. Journal of Metamorphic Geology 19:291–309. doi: 10.1046/j.0263-4929.2000.00312.x

Schmitz MD, Bowring SA (2003) Constraints on the thermal evolution of continental lithosphere from U–Pb accessory mineral thermochronometry of lower crustal xenoliths, Southern Africa. Contributions to Mineralogy and Petrology 144:592–618.

Schmocker M, Bystricky M, Kunze K, Burlini L, Stünitz H, Burg J-P (2003) Granular flow and Riedel band formation in water-rich quartz aggregates experimentally deformed in torsion. Journal of Geophysical Research 108:1–16. doi: 10.1029/2002JB001958

Schulmann K, Lexa O, Štípská P, Racek M, Tajčmanová L, Konopásek J, Edel J-B, Peschler A, Lehmann J (2008) Vertical extrusion and horizontal channel flow of orogenic lower crust: key

exhumation mechanisms in large hot orogens? Journal of Metamorphic Geology 26:273–297. doi: 10.1111/j.1525-1314.2007.00755.x

Scott DR, Stevenson DJ (1986) Magma Ascent by Porous Flow. Journal of Geophysical Research 91:9283–9296.

Scott T, Kohlstedt DL (2006) The effect of large melt fraction on the deformation behavior of peridotite. Earth and Planetary Science Letters 246:177 – 187. doi: 10.1016/j.epsl.2006.04.027

Shankland TJ, Ander MC (1983) Electrical conductivity, temperatures and fluids in the lower crust. Journal of Geophysical Research 88:9475–9484.

Shaw HR (1972) Viscosities of magmatic silicate liquids: An empirical method of prediction. American Journal of Science 272:870–893.

Sinha AK, Hewitt DA, Rimstidt JD (1986) Fluid interaction and element mobility in the development of ultramylonites. Geology 14:883–886. doi: 10.1130/0091-7613(1986)14<883

Slagstad T (2005) Formation, Crystallization, and Migration of Melt in the Mid-orogenic Crust: Muskoka Domain Migmatites, Grenville Province, Ontario. Journal of Petrology 46:893–919. doi: 10.1093/petrology/egi004

Smith J V, Brown WL (1988) Feldspar minerals, Vol.1 ed. 1–20541.

Smith V, Shane P, Nairn I (2010) Insights into silicic melt generation using plagioclase, quartz and melt inclusions from the caldera-forming Rotoiti eruption, Taupo volcanic zone, New Zealand. Contributions to Mineralogy and Petrology 160:951–971. doi: 10.1007/s00410-010-0516-0

Smithson SB (1978) Modeling continental crust-structural and chemical constraints. Geophysical Research Letters 5:749–752.

Spear FS, Wark DA (2009) Cathodoluminescence imaging and titanium thermometry in metamorphic quartz. Journal of Metamorphic Geology 27:187–205. doi: 10.1111/j.1525-1314.2009.00813.x

Stevenson J (1989) Spontaneous small-scale melt segregation in partial melts undergoing deformation. Geophysical Research Letters 16:1067–1070.

Stipp M, Stünitz H, Heilbronner R, Schmid SM (2002) The eastern Tonale fault zone : a “natural laboratory” for crystal plastic deformation of quartz over a temperature range from 250 to 700 8C. Journal of Structural Geology 24:1861–1884.

Stipp M, Tullis J (2003) The recrystallized grain size piezometer for quartz. Geophysical Research Letters 30:1–5. doi: 10.1029/2003GL018444

Stipp M, Tullis J, Behrens H (2006) Effect of water on the dislocation creep microstructure and flow stress of quartz and implications for the recrystallized grain size piezometer. Journal of Geophysical Research 111:B04201. doi: 10.1029/2005JB003852

Stipp M, Tullis J, Scherwath M, Behrmann JH (2010) A new perspective on paleopiezometry: Dynamically recrystallized grain size distributions indicate mechanism changes. Geology 38:759–762. doi: 10.1130/G31162.1

Stöckhert B, Renner J (1998) Rheology of crustal rocks at ultrahigh pressure. In: Hacker BR, Liou JG (eds) When Continents Collide: Geodynamics and Geochemistry of Ultrahigh- Pressure Rocks. Kluwer Academic Publishers, pp 57–95

Storm LC, Spear FS (2009) Application of the titanium-in-quartz thermometer to pelitic migmatites from the Adirondack Highlands, New York. Journal of Metamorphic Geology 27:479–494. doi: 10.1111/j.1525-1314.2009.00829.x

Stünitz H, Fitz Gerald JD, Tullis J (2003) Dislocation generation, slip systems, and dynamic recrystallization in experimentally deformed plagioclase single crystals. Tectonophysics 372:215–233. doi: 10.1016/S0040-1951(03)00241-5

Stünitz H, Tullis J (2001) Weakening and strain localization produced by syn-deformational reaction of plagioclase. International Journal of Earth Sciences 90:136–148. doi: 10.1007/s005310000148

Takeshita T, Hara I (1998) C-Axis fabrics and microstructures in a recrystallized quartz vein deformed under fluid-rich greenschist conditions. Journal of Structural Geology 20:417–431.

Tarantola A, Diamond LW, Stünitz H (2010) Modification of fluid inclusions in quartz by deviatoric stress I: experimentally induced changes in inclusion shapes and microstructures. Contributions to Mineralogy and Petrology 160:825–843. doi: 10.1007/s00410-010-0509-z

Tarantola A, Diamond LW, Stünitz H, Thust A, Pec M (2012) Modification of fluid inclusions in quartz by deviatoric stress. III: Influence of principal stresses on inclusion density and orientation. Contributions to Mineralogy and Petrology. doi: 10.1007/s00410-012-0749-1

Taylor SR, McLennan MS (1985) The Continental Crust: Its Composition and Evolution, Blackwell. Oxford

Tenthorey E, Cox SF (2006) Cohesive strengthening of fault zones during the interseismic period: an experimental study. Journal of Geophysical Research. doi: doi:10.1029/2005JB004122

Thomas JB, Watson BE (2012) Application of the Ti-in-quartz thermobarometer to rutile-free systems. Reply to: a comment on: "TitaniQ under pressure: the effect of pressure and temperature on the solubility of Ti in quartz" by Thomas et al. Contributions to Mineralogy and Petrology. doi: 10.1007/s00410-012-0761-5

Thomas JB, Watson BE, Spear FS, Shemella PT, Nayak SK, Lanzirotti A (2010) TitaniQ under pressure: the effect of pressure and temperature on the solubility of Ti in quartz. Contributions to Mineralogy and Petrology 160:743–759. doi: 10.1007/s00410-010-0505-3

Thompson JBJ, Waldbaum DR (1969) Mixing properties of sanidine crystalline solutions: III. Calculations based on two-phase data. American Mineralogist 54:811–838.

Thust A (2012) Experimentelle Verformung von natürlichen Quarzeinkristallen. Universität Basel

Thust A, Tarantola A, Stünitz H, Heilbronner R, Behrens H, Fitz Gerald JD (2012) Water redistribution in experimentally deformed natural quartz single crystals. 1–45.

Tullis J, Dell'Angelo LN, Yund RA (1990) Ductile shear zones from brittle precursors in feldspathic rocks: the role of dynamic recrystallization. American Geophysical Union Monograph 56:67–81.

Tullis J, Yund RA (1987) Transition from cataclastic flow to dislocation creep of feldspar : Mechanisms and microstructures. geology 15:606–609. doi: 10.1130/0091-7613(1987)15<606

Tullis J, Yund RA (1985) Geology Dynamic recrystallization of feldspar : A mechanism for ductile shear zone formation. geology 13:238–241. doi: 10.1130/0091-7613(1985)13<238

Tullis J, Yund RA (1980) Hydrolytic weakening of experimentally deformed Westerly granite and Hale albite rock. Journal of Structural Geology 2:439–451. doi: 10.1016/0191-8141(80)90005-X

Tullis J, Yund RA (1977) Experimental deformation of dry Westerly granite. Journal of Geophysical Research 82:5705–5718.

Tullis J, Yund RA (1992) The brittle -Ductile Transition in Feldspar Aggregates: An Experimental Study. Fault mechanics and transport properties of rock

Tullis J, Yund RA (1991) Diffusion creep in feldspar aggregates: experimental evidence. Journal of Structural Geology 13:987–1000.

Tullis J, Yund RA (1996) Deformation-enhanced fluid- distribution in feldspar aggregates and implications for ductile shear zones. Geology 24:63–66.

Tullis TE, Tullis J (1986) Experimental rock deformation techniques. Mineral and Rock Deformation: Laboratory Studies, vol. Geophysical Monograph

Tumarkina E, Misra S, Burlini L, Connolly JAD (2011) An experimental study of the role of shear deformation on partial melting of a synthetic metapelite. Tectonophysics 503:92–99. doi: 10.1016/j.tecto.2010.12.004

Turcotte DL, Ahern JL (1978) A Porous Flow Model for Magma Migration in the Asthenosphere. Journal of Geophysical Research 83:767–772.

Urai JL, Means WD, Lister GS (1986) Dynamic recrystallization of minerals. In: Hobbs B, Herald H. (eds) Mineral and Rock Deformation: Laboratory Studies, Paterson vol. Geophysical Monograph. American Geophysical Union, pp 161–199

Vazquez JA, Kyriazis SF, Reid MR, Sehler RC, Ramos FC (2009) Thermochemical evolution of young rhyolites at Yellowstone: Evidence for a cooling but periodically replenished postcaldera magma reservoir. Journal of Volcanology and Geothermal Research 188:186–196. doi: 10.1016/j.jvolgeores.2008.11.030

Vernooij MGC, Den Brok B, Kunze K (2006a) Development of crystallographic preferred orientations by nucleation and growth of new grains in experimentally deformed quartz single crystals. Tectonophysics 427:35–53. doi: 10.1016/j.tecto.2006.06.008

Vernooij MGC, Kunze K, Den Brok B (2006b) "Brittle" shear zones in experimentally deformed quartz single crystals. Journal of Structural Geology 28:1292–1306. doi: 10.1016/j.jsg.2006.03.018

Vigneresse JL (1995a) Control of granite emplacement by regional deformation. Tectonophysics 249:173–186. doi: 10.1016/0040-1951(95)00004-7

Vigneresse JL (1995b) Crustal regime of deformation and ascent of granitic magma. Tectonophysics 249:187–202. doi: 10.1016/0040-1951(95)00005-8

Vigneresse JL, Barbey P, Cuney M (1996) Rheological Transitions During Partial Melting and Crystallization with Application to Felsic Magma Segregation and Transfer. Journal of Petrology 37:1579–1600.

Vissers RLM, Drury MR, Newman J, Fliervoet TF (1997) Mylonitic deformation in upper mantle peridotites of the North Pyrenean Zone (France): implications for strength and strain localization in the lithosphere. Tectonophysics 279:303–325.

Waff HS, Bulau JR (1982) Experimental studies of near-equilibrium textures n partially molte silicates at high pressure. Earth and Planetary Science Letters 12:229–236.

Waff HS, Bulau JR (1979) Equilibrium fluid distribution in an ultramafic partial melt under hydrostatic stress conditions. Journal of Geophysical Research 84:

Waldbaum DR, Thompson JBJ (1969) Mixing properties of sanidine crystalline solution: IV. Phase diagrams from equations of state. American Mineralogist 54:1274–1298.

Wark DA, Hildreth W, Spear FS, Cherniak DJ, Watson BE (2007) Pre-eruption recharge of the Bishop magma system. Geology 35:235. doi: 10.1130/G23316A.1

Wark DA, Watson BE (2006) TitaniQ : a titanium-in-quartz geothermometer. Contributions to Mineralogy and Petrology 152:743–754. doi: 10.1007/s00410-006-0132-1

Watson BE (2004) A conceptual model for near-surface kinetic controls on the trace-element and stable isotope composition of abiogenic calcite crystals. Geochimica et Cosmochimica Acta 68:1473–1488. doi: 10.1016/j.gca.2003.10.003

Watson BE (1982) Melt infiltration and magma evolution. Geology 10:236–240.

Watson BE, Brenan JM (1987) Fluids in the lithosphere, 1. Experimentally-determined wetting characteristics of CO2-H2O fluids and their implications for fluid transport, host-rock physical properties, and fluid inclusion formation. Earth and Planetary Science Letters 85:497–515.

Watson BE, Liang Y (1995) A simple model for sector zoning in slowly grown crystals : Implications for growth rate and lattice diffusion , with emphasis on accessory minerals in crustal rocks. american Mineralogist 80:1179–1187.

Watts AB, Burov EB (2003) Lithosperic strength and ist relationship tot he elastic and seismologic layer thickness. Earth and Planetary Science Letters 213:113–131.

Weaver BL, Tarney J (1984) Empirical approach to estimating the composition of the continental crus. Nature 310:575–577.

Weaver BL, Tarney J (1981) Lewisian gneiss geochemistry and Archaean crustal development models. Earth and Planetary Science Letters 55:171–180.

Weaver BL, Tarney J (1980) Continental crust composition and nature of the lower crust: constraints from mantle Nd–Sr isotope correlation. Nature 286:342–346.

Weinberg RF (1999) Mesoscale pervasive felsic magma migration: alternatives to dyking. Lithos 46:393–410. doi: 10.1016/S0024-4937(98)00075-9

Weinberg RF (1996) Ascent mechanism of felsic magmas: news and views. Transactions of the Royal Society of Edinburgh, Earth Sciences 87:95–103.

Wheeler J, Prior DJ, Jiang Z, Spiess R, Trimby PW (2001) The petrological significance of misorientations between grains. Contributions to Mineralogy and Petrology 141:109–124. doi: 10.1007/s004100000225

White SH (1967) Geological significance of recovery and recrystallization processes in Quartz.

Wickham SM (1987) The segregation and emplacement of granitic magmas. Journal of the Geological Society 144:281–297. doi: 10.1144/gsjgs.144.2.0281

Willaime C, Christie JM, Mainprice D (1979) Experimental deformation of K-feldspar single crystals. Bull MIneral 102:168–177.

Wilson CJN, Seward TM, Allan ASR, Charlier BLA, Bello L (2012) A comment on: "TitaniQ under pressure: the effect of pressure and temperature on the solubility of Ti in quartz", by Jay B. Thomas, E. Bruce Watson, Frank S. Spear, Philip T. Shemella, Saroj K. Nayak and Antonio Lanzirotti. Contributions to Mineralogy and Petrology. doi: 10.1007/s00410-012-0757-1

Xia Q-K, Yang X-Z, Deloule E, Sheng Y-M, Hao Y-T (2006) Water in the lower crustal granulite xenoliths from Nushan, eastern China. Journal of Geophysical Research 111:B11202. doi: 10.1029/2006JB004296

Yu JH, Xu X, O'Reilly SY, Griffin WL, Zhang M (2003) Granulite xenoliths from Cenozoic Basalts in SE China provide geochemical fingerprints to distinguish lower crust terranes from the North and South China tectonic blocks. Lithos 67:77–102.

Zhai MG, Guo JH, Liu WJ (2001) An exposed cross-section of early Precambrian continental lower crust in North China Craton. Physics and Chemistry of the Earth Part A Solid Earth and Geodesy 26:781–792.

Zhang M, Zhou XH, Zhang JB (1998) Nature of the lithospheric mantle beneath NE China: evidence from potassic volcanic rocks and mantle xenoliths. In: Flower MFJ (ed) Mantle Dynamics and Plate Interactions in East Asia, AGU, Geody. pp 197–219

Zimmerman ME, Kohlstedt DL (2004) Rheological properties of partially molten lherzolite. Journal of Structural Geology 45:275–298.

Zimmerman ME, Zhang S, Kohlstedt DL, Karato S (1999) Melt distribution in mantle rocks deformed in shear. Geophysical Research Letters 26:1505. doi: 10.1029/1999GL900259

ISBN xxx-xx-xxxx-xxx-x